

# AD-A267 980



## DOCUMENTATION PAGE

Form Approved  
GSA GEN. REG. NO. 27

1

This report is the property of the Department of Defense and is loaned to your organization. It and its contents are not to be distributed outside your organization. If you are not an authorized recipient, please return this report to the Office of Management and Administration, Department of Defense, 4120 Randolph Avenue, Washington, DC 20341-1501.

1. REPORT DATE		3. REPORT TYPE AND DATES COVERED THESIS/DISSERTATION	
4. TITLE AND SUBTITLE A Comparative Study of Analog and Digital Control Laws for the UMCSL Truss		5. FUNDING NUMBERS	
6. AUTHOR(S) 2nd Lt Anthony M. Mitchell			
7. PERFORMING ORGANIZATION NAME(S) AND ADDRESS(ES) AFIT Student Attending: University of Washington		8. PERFORMING ORGANIZATION REPORT NUMBER AFIT/CI/CIA- 93-008	
9. SPONSORING/MONITORING AGENCY NAME(S) AND ADDRESS(ES) AFIT/CI Wright-Patterson AFB OH 45433-6583		10. SPONSORING/MONITORING AGENCY REPORT NUMBER	
11. SUPPLEMENTARY NOTES			
12a. DISTRIBUTION/AVAILABILITY STATEMENT Approved for Public Release IAW 190-1 Distribution Unlimited MICHAEL M. BRICKER, SMSgt, USAF Chief Administration		12b. DISTRIBUTION CODE	
13. ABSTRACT (Maximum 200 words)			
14. SUBJECT TERMS		15. NUMBER OF PAGES 145	
		16. PRICE CODE	
17. SECURITY CLASSIFICATION OF REPORT	18. SECURITY CLASSIFICATION OF THIS PAGE	19. SECURITY CLASSIFICATION OF ABSTRACT	20. LIMITATION OF ABSTRACT

# A Comparative Study of Analog and Digital Control Laws for the UWCSL Truss

by

Anthony Michael Mitchell

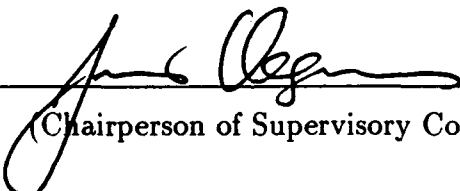
A thesis submitted in partial fulfillment  
of the requirements for the degree of

Master of Science in Aeronautics and Astronautics

University of Washington

1992

Approved by \_\_\_\_\_

  
(Chairperson of Supervisory Committee)

Program Authorized  
to Offer Degree \_\_\_\_\_

Date \_\_\_\_\_

DTIC QUALITY INSPECTED 3

Accession For	
NTIS CRA&I	<input checked="" type="checkbox"/>
DTIC TAB	<input type="checkbox"/>
Unannounced	<input type="checkbox"/>
Justification	
By	
Distribution/	
Availability Codes	
Dist	
A-1	

In presenting this thesis in partial fulfillment of the requirements for the Master's degree at the University of Washington, I agree that the Library shall make its copies freely available for inspection. I further agree that extensive copying of this thesis is allowable only for scholarly purposes, consistent with "fair use" as prescribed in the U. S. Copyright Law. Any other reproduction for any purposes or by any means shall not be allowed without my written permission.

Signature\_\_\_\_\_

Date\_\_\_\_\_

# TABLE OF CONTENTS

<b>List of Figures</b>	<b>iii</b>
<b>List of Tables</b>	<b>iv</b>
<b>Chapter 1 Introduction</b>	<b>1</b>
1.1 Background . . . . .	1
1.2 Problem Definition . . . . .	3
1.3 System Configuration . . . . .	3
1.3.1 Truss . . . . .	3
1.3.2 Air Jet Thrusters . . . . .	5
1.3.3 Reaction Mass Actuators . . . . .	6
1.3.4 Accelerometers . . . . .	6
1.3.5 Force Gage . . . . .	6
1.3.6 Electro-Mike Position Sensor . . . . .	7
1.3.7 Analog Computers . . . . .	7
1.3.8 National Instruments LABVIEW and DSP Boards . . . . .	7
1.3.9 Dynamic Signal Analyzer . . . . .	8
1.3.10 MATLAB and SIMULINK Software . . . . .	8
1.4 Thesis Outline . . . . .	8
<b>Chapter 2 System Modeling and Verification</b>	<b>9</b>
2.1 Overview . . . . .	9
2.2 Air Jet Thruster Modeling . . . . .	10
2.3 Reaction Mass Actuator Modeling . . . . .	13
2.4 Truss Modeling . . . . .	20
2.4.1 Finite Element Model of the UWCSL Truss . . . . .	20
2.4.2 Model Reduction . . . . .	25
2.4.3 Modeling of Truss Damping . . . . .	27
2.4.4 Eighth Order State Space Model . . . . .	28

2.4.5	Twelfth Order State Space Model . . . . .	29
2.5	Truss Model Validation . . . . .	30
2.5.1	Experimental Configuration without RMAs . . . . .	31
2.5.2	Experimental Configuration with RMAs . . . . .	38
<b>Chapter 3</b>	<b>Classical Analog Control Law Synthesis and Validation</b>	<b>44</b>
3.1	Overview . . . . .	44
3.2	Approximate Integrator for Velocity Feedback . . . . .	44
3.3	Classical Analog Control Using AJT Actuation . . . . .	47
3.3.1	Non-Linear Simulation . . . . .	48
3.3.2	Experimental Results . . . . .	49
3.4	Classical Analog Control Using RMA Actuation . . . . .	53
3.4.1	Non-Linear Simulation . . . . .	55
3.4.2	Experimental Results . . . . .	56
3.5	Classical Analog Control Using Hybrid Actuation . . . . .	60
3.5.1	Non-Linear Simulation . . . . .	61
3.5.2	Experimental Results . . . . .	62
<b>Chapter 4</b>	<b>Digital Control: Discretization and Digitization of Classical Analog Control Law</b>	<b>66</b>
4.1	Overview . . . . .	66
4.2	Digital Control . . . . .	66
4.3	Emulation by Tustin's Method . . . . .	69
4.4	LABVIEW: Digital Data Acquisition and Control . . . . .	71
4.5	Digital AJT Controller . . . . .	74
4.5.1	Non-Linear Simulation . . . . .	74
4.5.2	Experimental Results . . . . .	76
4.6	Digital RMA Controller . . . . .	80
4.6.1	Non-Linear Simulation . . . . .	81
4.6.2	Experimental Results . . . . .	82
4.7	Digital Hybrid Controller . . . . .	86
4.7.1	Non-Linear Simulation . . . . .	87

<b>Chapter 5</b>	<b>Linear Quadratic Regulator Design</b>	<b>90</b>
5.1	Overview . . . . .	90
5.2	Full-State Feedback Design Problem . . . . .	90
5.3	Non-Linear Simulation of Full-State Feedback to the RMAs . . . . .	96
5.4	Non-Linear Simulation of a Hybrid (Classical AJT and Full-State RMA) Controller . . . . .	97
<b>Chapter 6</b>	<b>Conclusion and Recommendations</b>	<b>103</b>
6.1	Overview . . . . .	103
6.2	Conclusions . . . . .	103
6.3	Recommendations for Future Research . . . . .	104
<b>Bibliography</b>		<b>107</b>
<b>Appendix A</b>	<b>AJT Control Circuitry</b>	<b>110</b>
<b>Appendix B</b>	<b>State space matrices</b>	<b>116</b>
<b>Appendix C</b>	<b>Euler-Bernoulli Beam Theory</b>	<b>119</b>
<b>Appendix D</b>	<b>Operating Instructions and Experiments for the UWCSL Truss</b>	<b>123</b>
D.1	Operating Instructions . . . . .	123
D.2	Experiments . . . . .	124
D.2.1	Open Loop: Swept Sine Resonant Frequency Determination . . . . .	124
D.2.2	Open Loop: Determination of Damping Coefficients . . . . .	126
D.2.3	Open Loop: Determination of Mode Shapes . . . . .	129
<b>Appendix E</b>	<b>SIMULINK Block Diagrams for Simulation</b>	<b>134</b>
<b>Appendix F</b>	<b>Digital Controller State Space Matrices and LABVIEW Diagrams</b>	<b>141</b>

## LIST OF FIGURES

1.1	Experimental Configuration . . . . .	4
2.1	AJT signals . . . . .	11
2.2	Non-Linear Block Diagram for AJT Model . . . . .	13
2.3	Reaction Mass Actuator (RMA) schematic . . . . .	15
2.4	RMA Attached to a Truss Node . . . . .	17
2.5	Block Diagram of RMA . . . . .	19
2.6	MAPMODES Coordinate Systems and Transformations . . . . .	22
2.7	Frequency Response: Experimental(Dashed), FEM(Solid) . . . . .	33
2.8	Tip Free Decay: Simulation without RMAs . . . . .	34
2.9	Tip Free Decay: Experimental Results without RMAs . . . . .	35
2.10	Second Order Free Vibration . . . . .	36
2.11	UWCSL Truss: Normalized Mode Shapes . . . . .	39
2.12	Frequency Response: Experimental(Dashed), FEM(Solid) . . . . .	40
2.13	Tip Free Decay: Simulation with RMAs . . . . .	42
2.14	Tip Free Decay: Experimental Results with RMAs . . . . .	43
3.1	Frequency Response: Ideal Integrator (Solid), Approximate Integrator (Dashed) . . . . .	46
3.2	Approximate Integrator for Analog Computer Implementation . . . . .	47
3.3	Simulation of AJT Controller . . . . .	50
3.4	Experimental AJT Controller . . . . .	51
3.5	Experimental AJT Controller . . . . .	52
3.6	Simulation of RMA Controller . . . . .	57
3.7	Experimental RMA Controller . . . . .	58
3.8	Experimental RMA Controller . . . . .	59
3.9	Simulation of Hybrid AJT and RMA Controller . . . . .	63
3.10	Experimental Hybrid AJT and RMA Controller . . . . .	64
3.11	Experimental Hybrid AJT and RMA Controller . . . . .	65

4.1	Block Diagram of a Continuous and Digital Control System . . . . .	68
4.2	Simulation of Digital AJT Controller . . . . .	77
4.3	Experimental Digital AJT Controller . . . . .	78
4.4	Experimental Digital AJT Controller . . . . .	79
4.5	Simulation of Digital RMA Controller . . . . .	83
4.6	Experimental Digital RMA Controller . . . . .	84
4.7	Experimental Digital RMA Controller . . . . .	85
4.8	Simulation of Digital Hybrid Controller . . . . .	89
5.1	Simulation of Full-State Feedback to the RMAs . . . . .	98
5.2	Simulation of Full-State Feedback to the RMAs . . . . .	99
5.3	Simulation of Hybrid Controller (Classical AJT and Full-State RMA)	101
5.4	Simulation of Hybrid Controller (Classical AJT and Full-State RMA)	102
A.1	Lead Network Circuit Diagram . . . . .	111
A.2	Accelerometer Circuit . . . . .	114
A.3	AJT Switching Circuit . . . . .	115
C.1	Cantilever Beam Schematic . . . . .	119
D.1	Experiment 1 Configuration . . . . .	132
D.2	Experiment 2 Configuration . . . . .	133
E.1	SIMULINK Block Diagram: AJT Controller . . . . .	135
E.2	SIMULINK Block Diagram: Hybrid AJT and RMA Controller . . . . .	136
E.3	SIMULINK Block Diagram: Digital AJT Controller . . . . .	137
E.4	SIMULINK Block Diagram: Digital Hybrid Controller . . . . .	138
E.5	SIMULINK Block Diagram: Full-State Feedback for RMA . . . . .	139
E.6	SIMULINK Block Diagram: Hybrid (Full-State RMA, Classical AJT)	140
F.1	LABVIEW: Block Diagram Hierarchy and Front Panel . . . . .	143
F.2	LABVIEW: Digital AJT Controller Block Diagram . . . . .	144
F.3	LABVIEW: Digital RMA Controller Block Diagram . . . . .	145

## LIST OF TABLES

2.1	Experimentally Determined Values for RMA Models . . . . .	19
2.2	Average Mass and Stiffness Properties of Truss Members . . . . .	21
2.3	UWCSL Truss without RMAs: Resonant Natural Frequencies . . . . .	32
2.4	UWCSL Truss without RMAs: Experimentally Determined Damping Ratios $\zeta_{AJT}$ . . . . .	38
2.5	UWCSL Truss with RMAs: Resonant Natural Frequencies . . . . .	41
2.6	UWCSL Truss with RMAs: Experimentally Determined Damping Ratios ( $\zeta_{RMA}$ ) . . . . .	43
3.1	AJT Controller: Approximate Simulation Settling Times in Seconds .	49
3.2	AJT Controller: Experimentally Determined Damping Ratios ( $\zeta_{clAJT}$ )	53
3.3	RMA Feedback Gains on Truss Velocities . . . . .	55
3.4	RMA Controller: Approximate Simulation Settling Times in Seconds	56
3.5	RMA Controller: Experimentally Determined Damping Ratios ( $\zeta_{clRMA}$ )	60
3.6	Hybrid Controller: Approximate Simulation Settling Times in Seconds	62
3.7	Hybrid Controller: Experimentally Determined Damping Ratios ( $\zeta_{clHYB}$ )	65
4.1	Tustin Method: Discrete State Space Matrices . . . . .	71
4.2	Digital AJT Controller: Approximate Simulation Settling Times in Seconds . . . . .	76
4.3	Digital AJT Controller: Experimentally Determined Damping Ratios	80
4.4	Digital RMA Controller: Approximate Simulation Settling Times in Seconds . . . . .	82
4.5	Digital RMA Controller: Experimentally Determined Damping Ratios ( $\zeta_{clDRMA}$ ) . . . . .	86
4.6	Digital Hybrid Controller: Approximate Simulation Settling Times in Seconds . . . . .	89

5.1 Full-State Feedback RMA Controller: Approximate Simulation Settling Times in Seconds . . . . .	97
5.2 Hybrid LQR Controller: Approximate Simulation Settling Times in Seconds . . . . .	100

## ACKNOWLEDGMENTS

It says on the cover "this thesis is submitted in partial fulfillment of the requirements for the degree of MSAA," but "partial" seems insufficient for defining the time and energy involved in the research and documentation of this work. I don't know who learned more about the other, the truss or me.

Of course, I could not have completed this thesis on my own and gladly accepted the assistance and advice of others. It would be an impossible task to individually thank all of the people who have assisted me through the academics, the research, and my life. To those of you, who I forget to mention - no offense, better luck next time.

First and foremost, I would like to thank Jesus Christ for blessing me with the talent and tools to accomplish all that I have been able to do. I would like to thank the members of the Oates family for their support of the fellowship in memory of Dr. Gordon Oates, which enabled me to pursue this degree and chase my dreams. Sincere thanks to Professor Juris Vagners, who brought me to the University of Washington, steered me through the maze of research toward the completion of this thesis, and taught me, by example, that you can always play, and play to win. Thanks to Marcus Schulthess and Mike Shepherd who established the UWCSL truss and bestowed upon me their advice regarding academic pursuits, the truss, and of course, the Seattle scene. Thanks also goes to Hamid Montazeri and all of the Zoomies who have helped me out along the way.

Thank you Mom, Dad and Bob for your encouragement and support. You knew that I would make it all along, didn't you? Finally, thank you Siri, for exploring Seattle with me and constantly reminding me that there is more to life than a Master's Degree. Latte!

*To Siri, you said "yes" and changed my life forever*



## Chapter 1

# INTRODUCTION

### *1.1 Background*

Large flexible structures are used in a variety of space applications including astronomy, communications, directed energy, SDI (Strategic Defense Initiative), and other areas or research. Many of these applications require stable platforms from which high precision optical systems or delicate sensors must be employed. Space structures serve as platforms for space based payloads such as precise sensors (scientific data gathering devices), sensitive optical elements (cameras, gyros, lasers, telescopes, etc.) and human beings (on space stations). These platforms are light weight, flexible structures capable of supporting large loads in low gravity environments, but are susceptible to bending and vibrating due to their low inherent damping qualities. The problems associated with the vibration of large space structures are becoming increasingly more important as larger and more sophisticated equipment is placed in orbit around the Earth. Disturbances can be caused both internally, by vibrating or rotating mechanical parts or structural maneuvering, and externally by collisions with space debris, solar winds or asymmetric heating, or other forces [9].

The challenge engineers face with flexible space structures is two-fold. The first is to design a structure that will support the desired payload, meet the mission requirements, and be capable of launch and deployment into space. The second is to control the structure's orientation and effectively suppress vibrations to allow the payload to remain in orbit and successfully complete its mission. Control engineers are primarily concerned with the second challenge; vibration suppression and control of the structure's orientation once it is deployed in the space environment. The vacuum of space imposes constraints on the control of spaced based systems. No reacting medium is available to absorb energy or provide viscous damping in space and therefore, all of the energy created by the system must be dealt with by onboard systems. Onboard structural control systems are known as Space Realizable Actuation (SRA) and in-

volve two types of energy dissipation. The first, a non-renewable method, relies on thrusters and/or rockets to translate or rotate the structure. The second, an electrically powered method, relies on momentum exchangers, such as proof mass actuators to dissipate motion [20]. Another method to side step the problem of low structural damping is active control of beam steering mirrors and optical lenses onboard the platforms [1, 2, 19]. However, low frequency structural resonance effects may be uncontrollable by the high frequency, high precision mirror and optics controllers.

Features of flexible space structures can be captured in some simple, Earth-based laboratory experiments such as the planar truss testbed at the University of Washington Control Systems Laboratory (UWCSL). The UWCSL 20-Bay planar truss is modeled after a truss at the United States Air Force Academy (USAFA) in Colorado Springs, CO. Applying control laws to the air jet thrusters (AJTs) and reaction mass actuators (RMAs) to suppress the vibrations of the experimental truss, control engineers can better understand and learn how to control space-based systems. Previous research at USAFA [7] and at the University of Washington [20] points toward a unique solution which incorporates the control laws for the two actuator types in conjunction with one another. The AJTs are effective for high amplitude disturbances at low frequencies while the RMAs have a higher bandwidth and are more effective at higher frequencies and lower amplitude disturbances. "Hybrid actuation is the terminology coined by the USAFA team to describe the simultaneous functioning of two or more types of structure-borne actuators in active vibration control, each type having a frequency band of greatest effectiveness that is different from the bands of the other types." [7]

The research presented in this thesis includes verification and modification of previous work on the UWCSL truss which includes both system modeling and the classical AJT, RMA, and hybrid analog control laws. Discretization and digitization of the classical analog control laws was accomplished, the control laws were simulated and subsequently implemented on the truss. A comparative study of the analog and digital control laws was accomplished. The development of a Linear Quadratic (LQ) optimal, full-state feedback control law for the RMAs was also examined in this thesis. Simulation of hybrid actuation utilizing the optimal RMA control law and the classical AJT control law is reported and compared to the pure classical control law design.

## 1.2 Problem Definition

The objectives of the research conducted for this thesis were to verify previous controller designs and to design and implement new control laws for vibration suppression of a lightly damped flexible structure in a cantilever beam configuration. Two methods of actuation are currently used to excite and control the structure: air jet thrusters (AJTs) and structurally-borne reaction mass actuators (RMAs). The actuators are located at the midpoint and the tip (free end) of the truss for convenience and are configured to excite and control lateral motion. Accelerometers are used to sense the motion of the flexible structure as it vibrates. The accelerometers are mounted at the midpoint and tip of the truss, to provide colocated sensor-actuator pairs. The objective of the classical and modern control laws is to improve the stability of the structure using active control to increase its modal damping. The performance of the controller is evaluated based on the amount of time required to reduce the excited states of the truss to within  $\pm 1\%$  of the equilibrium value. This is commonly referred to as the settling time. The damping ratios of the truss, in different controller configurations, are also compared as an alternative criterion for control law performance.

## 1.3 System Configuration

Each component of the hardware of the UWCSL truss and analysis equipment is described in this section. System modeling and verification of the truss and actuators models will be discussed in Chapter 2. A schematic diagram of the experimental configuration of the flexible truss in the UW Control Systems Laboratory which depicts the major hardware components, is shown in Figure 1.1.

### 1.3.1 Truss

The UWCSL truss is a 23.2 feet long, aluminum and steel, flexible structure weighing 239 lbs. One end of the truss is bolted to a rigid steel table which is anchored to the concrete floor of the lab. The cantilever structure is composed of 20 square

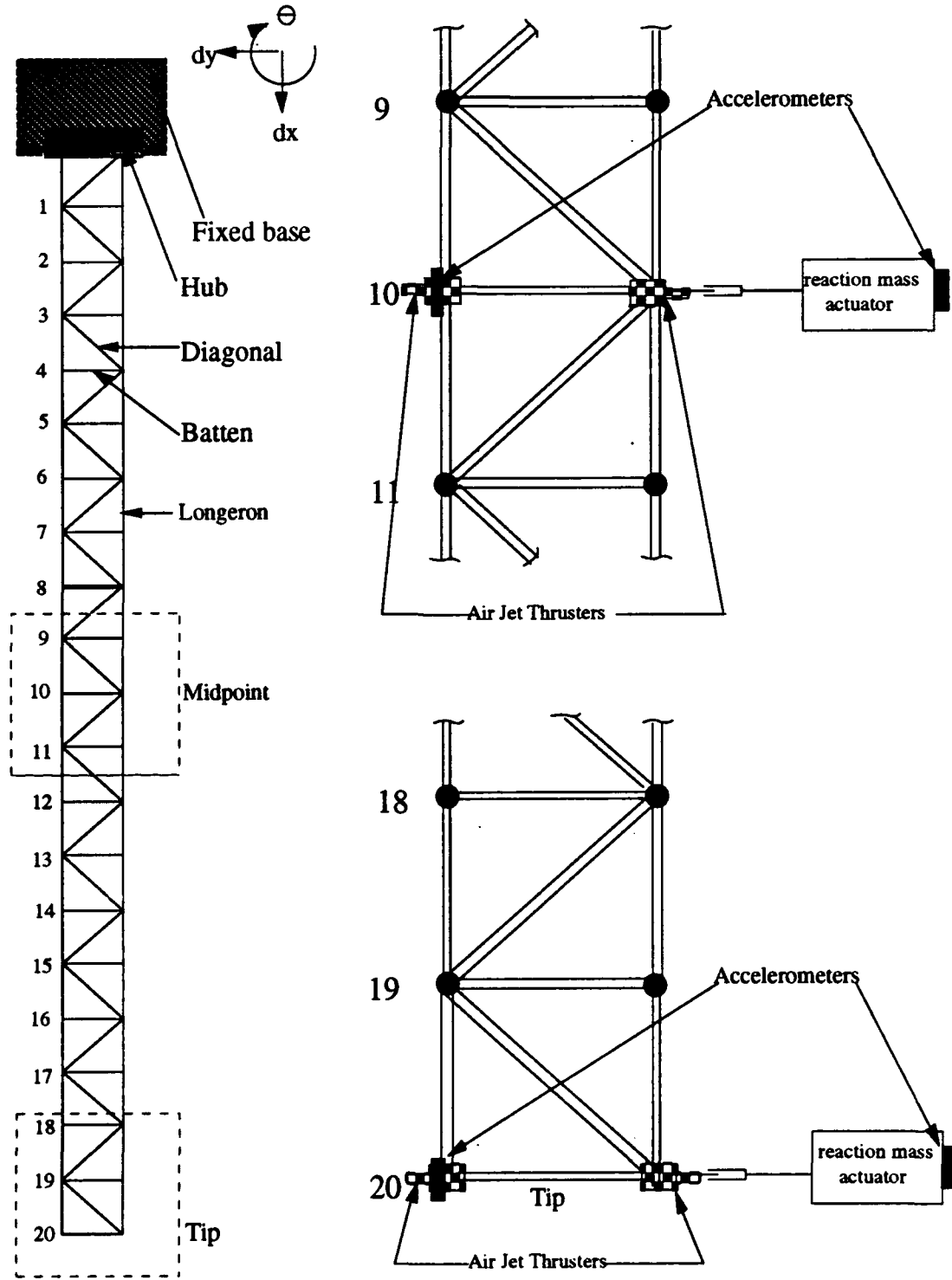


Figure 1.1: Experimental Configuration

bays with sides 1.161 feet in length. The square bays are fitted with alternating diagonal members to increase stiffness, each 1.640 feet in length. The entire structure rests on steel ball bearings, 0.748 in diameter, to minimize the friction with the supporting table and to allow planar motion. Rigid steel battens are fixed to the lateral members of the truss to increase the mass of the structure, to reduce the amplitude of the disturbances and to lower the natural frequencies of the lateral bending modes [20]. The first four bending modes of the open loop truss without the reaction mass actuators attached are experimentally determined to occur at 1.485, 9.14, 24.545, and 42.678 Hz. The first four bending modes of the open loop truss with the reaction mass actuators attached are experimentally determined to occur at 1.485, 9.508, 24.545, and 42.678 Hz. The experimental methods and results of truss modeling and verification are presented in Section 2.5.

The following locations on the truss, which will be frequently referenced, are the 1/4 point (station 5), midpoint (station 10), 3/4 point (station 15), and tip (station 20). Station 0 is the end of the truss bolted to the box beam on the steel table. Station 20 is the free end of the truss (See Figure 1.1).

### *1.3.2 Air Jet Thrusters*

Four identical air jet thrusters (AJTs), one pair at the tip and the other pair at the midpoint of the truss, are used to excite and control the lateral bending modes of the truss. The AJTs are "bang-bang" actuators driven by on-off triggered circuits which function as a pair, each AJT firing transversely in opposite directions. A positive control signal voltage fires one of the air jet thrusters while a negative signal fires the opposing AJT. Ideal on-off forces cannot be realized by the AJTs due to the dynamics of high speed air flow and the dynamics of the solenoid valves. There are non-linear time delays between the control signal and the realization of full-on or full-off thrust [7]. The principal component of the AJT is a solenoid valve manufactured by MAC Valves, Inc. The source of pressurized air used to drive the AJTs is pressurized air regulated to 65 psi, providing a steady state output thrust of 0.6 lbf.

### 1.3.3 Reaction Mass Actuators

Two reaction mass actuators (RMA) are attached to the tip and midpoint of the truss. The RMAs are Ling Dynamics V102 Shakers mounted on aluminum bases which ride on similar ball bearings to those of the truss. The DC motor of the shaker is attached to the truss steel joint with a stinger which allows for small misalignments. This configuration simulates structurally-borne actuation without permanently fixing the RMAs to the truss. The connection of the RMAs to the truss via the stingers alters the structure's modal frequencies by increasing the mass of the structure and acting as passive dampers. Ling Dynamics variable gain amplifiers provide the power supplies for the RMAs.

### 1.3.4 Accelerometers

The lateral excitation of the truss is sensed by four high-precision accelerometers from Sundstrand Data Control. Two of the accelerometers are mounted on the truss, colocated with the actuators at the tip and midpoint. An accelerometer is also mounted to the aluminum base of each of the RMAs to sense lateral motion and provides for measurement of RMA lateral acceleration relative to the truss relative acceleration at the corresponding connection node. The difference in these relative accelerations is used in the control law for the RMAs. A 30 K $\Omega$  resistor increases the sensitivity of the accelerometers to an output of 38.8 volts/g which corresponds to an output of  $9.709 \frac{\text{in}/\text{sec}^2}{\text{volt}}$  [19].

### 1.3.5 Force Gage

A Transducer Techniques force gage/load cell, model MDB-10, was used to characterize the AJTs and the RMAs. The force gage has a linear range of -10 to 10 lbs, and is calibrated in compression only. A TM-2 strain gage transducer amplifier module is used to power the force gage and measure the output forces. The amplifier is equipped with a 10  $\mu\text{f}$  filter capacitor for noise suppression, which results in an appreciable phase lag above the cutoff frequency.

### *1.3.6 Electro-Mike Position Sensor*

An Electro Corporation displacement transducer was used to measure the mode shapes of the truss. The transducer has a linear range of 0.050 to 0.500 inches, but the sensitivity and linearity of the sensor is dramatically affected by the type of metal to be monitored. A low level radio frequency field is generated in front of the sensor which causes eddy currents to form around any metal object the field intercepts. These induced eddy currents remove energy from the electric field reducing the Quality Factor ( $Q$ ) of the sensor coil [19]. This change in the Quality Factor is translated into an output signal proportional to the distance from the target to the sensor. Magnetic steel provides data with the best linearity and an error on the order of 0.9 percent of full scale.

### *1.3.7 Analog Computers*

The Electronic Associates, Inc. EAI TR-20 computers were used to implement the classical control laws in this experiment. Banana plug leads and adjustable pots were used to construct circuits on the available operation amplifiers and potentiometers. The linear operating range for the computers is  $\pm 10$  volts. The EAI TR-20 analog computers were constructed in 1966 and although they function adequately, their reliability is questionable.

### *1.3.8 National Instruments LABVIEW and DSP Boards*

LABVIEW 2 is a National Instruments Corporation software package designed to simplify scientific computation, process control, and test and measurement applications. LABVIEW is an acronym for Laboratory Virtual Instrument Engineering Workbench. LABVIEW is a programming language which replaces code with intuitive graphic objects in a user friendly environment. For the application reported in this thesis, the LABVIEW code was implemented on a Macintosh Quadra 900 equipped with digital signal processing (DSP) boards. The primary DSP board in use in the UW Control Systems Laboratory is the National Instruments NB-MIO-16, a high-performance multifunction analog, digital, and timing input/output board.

### *1.3.9 Dynamic Signal Analyzer*

Data acquisition and signal analysis was performed on the Hewlett Packard (HP) 35665A Dynamic Signal Analyzer. It is a two channel fast-fourier-transform (FFT) spectrum/network analyzer with a frequency range from DC to 100 kHz. The HP 35665A is an all-purpose tool for measurement and evaluation of electronic and mechanical devices. It is primarily a frequency domain analyzer, but is also used for time domain measurements. The analyzer is equipped to perform both random noise and swept sine device characterization.

### *1.3.10 MATLAB and SIMULINK Software*

Computer analysis and simulation were performed using MATLAB/SIMULINK software by Mathworks, Inc. [14] operated on DEC workstations equipped with X-windows. Both MATLAB and SIMULINK are linear/non-linear analysis and dynamic simulation packages. SIMULINK is a program for simulating dynamic systems using block diagrams to establish the system models. SIMULINK provides time response simulations with the capability to include non-linear and/or discrete time blocks.

## *1.4 Thesis Outline*

Theoretical development and experimental verification of the AJT, the RMA, and the UWCSL truss models are reported in Chapter 2. Classical control law theory and experimental verification of AJT, RMA, and hybrid classical analog control techniques are presented in Chapter 3. Chapter 4 includes the discretization (emulation) of the classical analog controllers and digital implementation on the truss. Simulation and experimental results of the classical control law, analog and digital, are also presented in Chapter 3 and Chapter 4 respectively. An optimal, full-state feedback controller for the RMAs is presented in Chapter 5 along with simulation results of the hybrid LQ RMA controller and the classical AJT controller. Conclusions and recommendations for future study are stated in Chapter 6. Appendices are included to explain experimental techniques, to present schematic diagrams of circuits and their explanations, to provide exact numerical models, and to present an inventory of equipment used to accomplish the research in this thesis.

## Chapter 2

# SYSTEM MODELING AND VERIFICATION

### 2.1 Overview

In control systems engineering, system modeling and verification often takes a secondary role to the development of control laws to stabilize the system. Design of the control laws is based on the premise that a precise or exact model of the system exists. Assuming a model of the system is available, the control law is designed to be robust, in order to allow for uncertainties in the model. A large amount of time is consumed in designing robust and efficient controllers for implementation in the system. Implementation of the control law on the actual hardware often reveals shortcomings in the controller if not complete failure of the design. Considerable effort is then spent modifying the control laws or the model to obtain the desired performance.

By accurately modeling the system and experimentally verifying the model with hardware prior to controller design, the control system engineer can more effectively and efficiently design and implement realizable control laws. Through an understanding of the system dynamics and modeling constraints, the designer can more readily identify design flaws and correct implementation failures.

Previous research has been accomplished in the development of a low order model of the flexible truss in the cantilever configuration using finite element methods and is used as the starting point for this research [7, 2, 19, 20]. Previous development of the air jet thruster (AJT) and reaction mass actuator (RMA) models has also been accomplished. This chapter examines the theoretical development of the model for the UWCSL truss, verification of the model through dynamic characterization of the hardware, and modification of the model to reflect the damping of the actual hardware. The final result of this process is an accurate model of the system which can be used for control law synthesis.

## 2.2 Air Jet Thruster Modeling

Theoretical modeling and experimental verification of the air jet thrusters (AJTs) has been accomplished by Hallauer at USAFA and Barker, Schulthess, and Shepherd at UWCSL [7, 2, 19, 20]. A summary of their research is presented for a more complete analysis of the system model. Four identical AJTs, one pair at the tip and the other pair at the midpoint of the truss, are used to excite and control the lateral bending modes of the truss. The AJT operates through the actuation of a solenoid valve which has two positions, full-on or full-off, which characterizes them as "bang-bang" actuators. The AJTs are driven by on/off triggered circuits. The switching is implemented through transistors which open and close each respective valve whenever the control signal passes through a zero reference. A small "dead band" in the voltage exists to prevent the AJTs from firing due to bias and noise in the control signal [7]. The "dead band" zone is realized with operational amplifiers and lead filters in the AJT circuitry. A complete description of the AJT circuits and schematic diagrams can be found in Appendix A, which is an excerpt from Schulthess' MSA thesis [19]. The AJTs have inherent non-linearities and a limited bandwidth, both of which must be examined in the modeling process.

Hallauer [7] defined the relationship between the output thrust ( $F(t)$ ) and the steady state output force ( $F_{ss}$ ) of an ideal AJT with a uniform valve time delay ( $\tau_d$ ) to a control signal ( $e(t)$ ) in Equation 2.1. The "dead band" is represented by  $e_d$ .

$$F(t) = \frac{1}{2}F_{ss}[1 + \text{sgn}(e(t - \tau_d))] \quad (2.1)$$

where

$$\begin{aligned} \text{sgn}[e(t)] &= 1, e(t) > e_d \\ \text{sgn}[e(t)] &= 0, |e(t)| < e_d \\ \text{sgn}[e(t)] &= -1, e(t) \leq -e_d \end{aligned}$$

Ideal on/off forces cannot be realized by the AJTs due to the dynamics of high speed air flow and the dynamics of the solenoid valves. The AJT experiences non-linear time delays between the time when the valve receives the control signal and the realization of full-on or full-off thrust [7]. The rise time ( $t_r$ ) is defined as the time

required for the response to rise from 10% to 90% of its final value [17]. The rise time from the control signal input to the steady state force output can be modeled as a second order critically damped system. The natural frequency ( $\omega_n$ ) of this system is defined in Equation 2.2 [20].

$$\omega_n = \frac{6}{t_r} \quad (2.2)$$

An illustration of a control signal  $e(t)$ , a switching signal  $\text{sgn}[e(t)]$ , the AJT steady state thrust ( $F_{ss}$ ), and an AJT output force  $F(t)$  is presented in Figure 2.1. The diagram also depicts the rise time ( $t_r$ ).

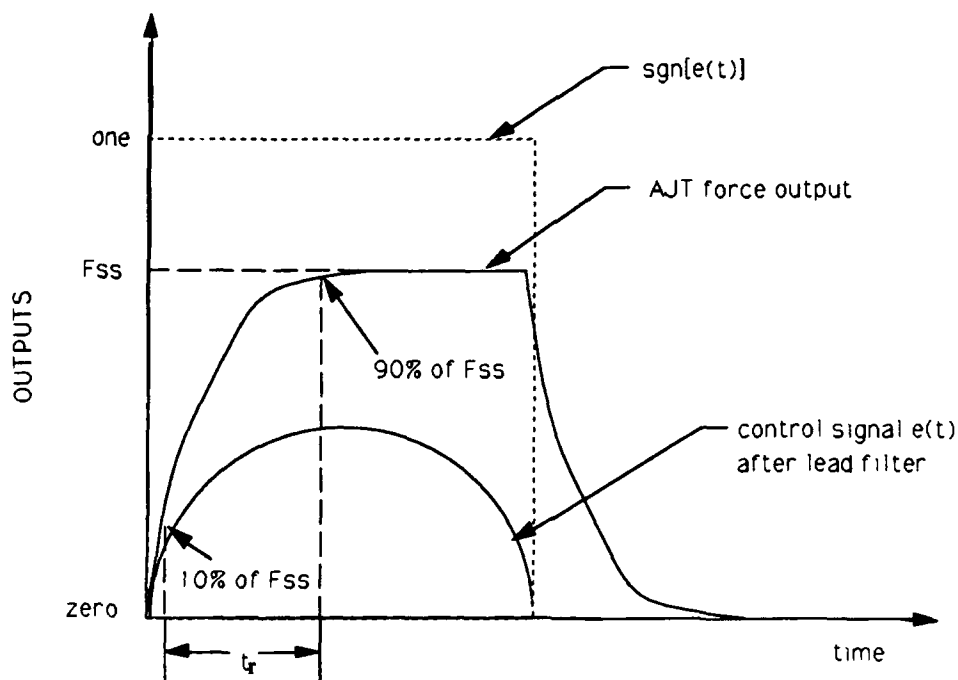


Figure 2.1: AJT signals

Equation 2.3 is the time domain step response of a second order system model of a "back to back" pair of AJTs, each projecting a force in opposite directions [20]. Due to the non-linear nature of the AJTs, the magnitude of the output force is not proportional to the magnitude of the control signal.

$$F(t) = F_{ss} \text{sgn}[e(t)][1 - \exp(-\omega_n(t - sw(t)))(1 + \omega_n(t - sw(t)))] \quad (2.3)$$

where the function  $sw(t)$  is defined as:

$$sw(t) = t, \text{ when } e(t) = 0 \quad (2.4)$$

The rise time delay can be modeled as a second order transfer function where  $s = j\omega$  as seen in Equation 2.5 [20].

$$G_{\tau_r}(j\omega) = \left. \frac{F_{ss}\omega_n^2}{(s + \omega_n)^2} \right|_{s = j\omega} = \frac{F_{ss}\omega_n^2}{(j\omega + \omega_n)^2} \quad (2.5)$$

A phase lag ( $\phi_d$ ) is associated with the rise time delay and Hallauer [7] recommended modeling it as:

$$\phi_d = -\omega\tau_d \quad (2.6)$$

This phase lag can be obtained from the second order transfer function model of the rise time in Equation 2.5.

$$\phi_{\tau_r} = \angle \frac{F_{ss}\omega_n^2}{(j\omega + \omega_n)^2} \quad (2.7)$$

The lead filter which precedes the transistors in the AJT switching circuit affects the phase lag of the AJT model. This lead filter and its phase lag are modeled as the following transfer function [20, 19]:

$$G_{LF}(s) = \frac{0.5s}{s + 1.5} \text{ and } \phi_{LF} = \angle \frac{0.5s}{s + 1.5} \quad (2.8)$$

The AJT rise time and lead filter transfer functions are combined to produce the model of the phase lag of the AJTs [2].

$$\phi_d = \phi_{\tau_r} + \phi_{LF} \quad (2.9)$$

The combined transfer function models of the rise time and the lead filter results in the finalized model of the AJTs. For convenience, the roots are altered slightly so as

to eliminate the repeated roots in the characteristic equation. This is accomplished by making the damping ratio ( $\zeta$ ) less than one, slightly below that of the critically damped case [20].

$$G(s) = \frac{F_{ss}\omega_n^2}{(s^2 + 2\zeta\omega_n s + \omega_n^2)} \quad (2.10)$$

Figure 2.2 is the non-linear block diagram used in SIMULINK to determine the AJT model effectiveness [20].

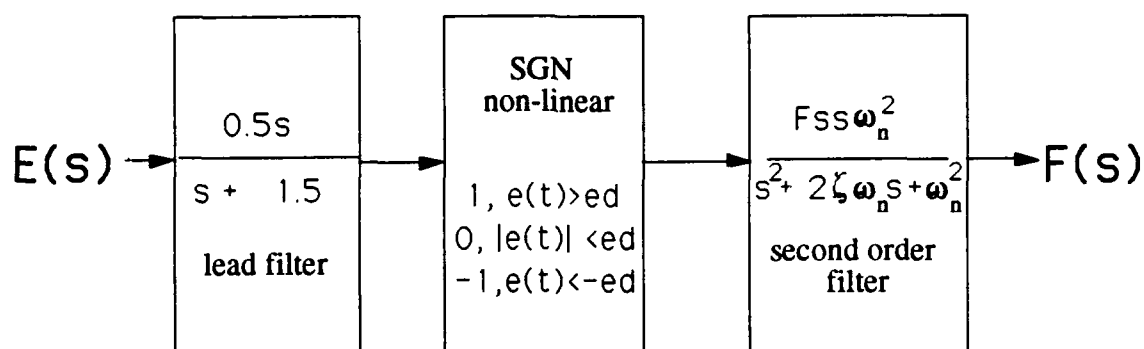


Figure 2.2: Non-Linear Block Diagram for AJT Model

Experimental results show that the AJTs have a steady state output force of 0.6 lbf. The results, determined by Shepherd and Schulthess at UWCSL, also show the actual air jet thrusters (AJTs) to have an effective bandwidth of 0-10 Hz. Above 10 Hz, the AJTs have a roll-off greater than 40 dB/dec and no longer follow the models frequency response. This explains the difficulty in using the AJTs alone to control the higher bending modes of the truss. The rise time ( $t_r$ ) from the control signal input to the steady state force output was found to be approximately 30 ms. Substituting the experimentally determined rise time ( $t_r$ ) in Equation 2.2, the natural frequency ( $\omega_n$ ) of the AJTs is determined to be 200 rad/sec [19, 20]. The experimental and theoretical phase plots, developed by Shepherd [20] are closely matched which confirms the proximity of the model to the actual hardware.

### 2.3 Reaction Mass Actuator Modeling

Theoretical modeling and experimental verification of the reaction (proof) mass actuators (RMAs) has been accomplished by Hallauer at USAFA and Barker and Shep-

herd at UWCSL [7, 2, 20]. A summary of their research is presented here to provide a more thorough analysis of the system model. Two reaction mass actuators (RMAs) are attached to the tip and midpoint of the truss with stingers. The RMAs roll on a tripod of steel ball bearings, in grooves to maintain one-dimensional motion, which simulate structurally-borne actuation. The RMAs are space-realizable actuators which do not require connections to the ground, and are self-contained except for connections to a power source and a sensor. An accelerometer is affixed to each of the stands which support the RMA in order to allow the measurement of relative acceleration between the truss and the RMA. The relative acceleration is determined using the difference between the truss mounted accelerometer signal and the RMA mounted accelerometer signal. The reaction (proof) mass actuator is a reaction-type force actuator which creates a force by reacting against an inertial mass [10]. The RMA relies on an electromagnetic interaction force ( $f_b$ ) between the proof mass ( $m_a$ ) and the system mass ( $m_s$ ) to "resist" undesired system motion [2].

The RMA consists of a moveable "proof mass," a fixed coil, a magnet inside the coil, a collocated sensor, a digital microcontroller, and power amplifier. All of the RMA components are mounted on a single fixture except for the external power amplifier. A current is applied via the power amplifier to the fixed coil which changes the polarity of the magnet, suspended inside the coil by a flexible suspension system attached to the reaction mass [20]. The magnet is attached to a stinger which in turn is connected to the joint of the truss structure, at the tip or midpoint. A schematic diagram of the RMA is shown in Figure 2.3.

The electromagnetic force ( $f_b$ ) exerted on the proof mass and thus, back to the structure, is expressed in the following equation:

$$f_b(t) = BLi(t) \quad (2.11)$$

where  $B$  is the magnetic flux density which is cut by the coil.  $L$  is the length of the wire in the annular gap between the proof mass and the coil and  $i(t)$  is the current in the coil [23].  $B$  is a function of the total magnetic flux supplied to the gap and the surface area of the two poles of the flux loop.  $L$  is a function of the mean diameter of the coil and the number of turns of wire per meter of coil length [23]. The product of  $B$  and  $L$  is specific to each RMA and is defined as the constant  $G_1$  with units of

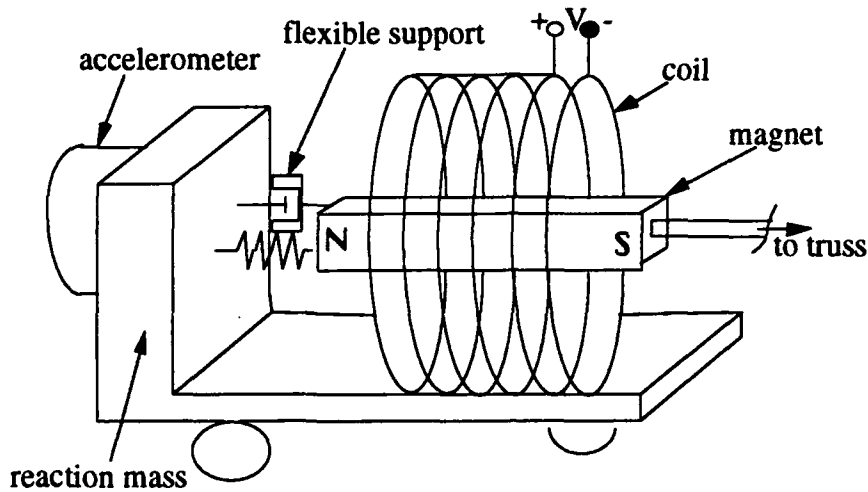


Figure 2.3: Reaction Mass Actuator (RMA) schematic

lbs/amp. This holds under the assumption that the total magnetic flux is cut by the coil and that the mean diameter of the coil is the average of the two poles [23]. The current supplied to the coil is proportional to the input voltage by the constant  $G_2$ , with units of volts/amp. Using the constants,  $G_1$  and  $G_2$ , Equation 2.11 can be modified to express the total force applied to the proof mass as

$$f_b(t) = G_1 G_2 v(t) \quad (2.12)$$

where  $v(t)$  is the total voltage applied across the coil [23]. By neglecting the back emf damping, assuming that no equilibrium restoring voltage exists, the total voltage across the coil ( $v(t)$ ) is equal to the command voltage  $e(t)$ . This is a valid assumption due to the large damping in the flexible suspension system which is greater than the damping the back emf is capable of generating [20].

The damping of the flexible support structure can be approximated as viscous damping ( $c$ ) and the stiffness approximated by a linear spring constant ( $k$ ). The assumption that the RMA can be modeled as a constant coefficient mass-spring-damper system leads to the following relationship:

$$f_b(t) - c\dot{x}(t) - kx(t) = G_1G_2e(t) - c\dot{x}(t) - kx(t) = m\ddot{x}(t) \quad (2.13)$$

The transfer function of the "stand alone" RMA, from Equation 2.13, is

$$\frac{F_b(s)}{E(s)} = \frac{G_1G_2ms^2}{ms^2 + cs + k} \quad (2.14)$$

$F_b(s)$  is the Laplace transform of the total force output and  $E(s)$  is the Laplace transform of the input (command) voltage. "Stand alone" implies that the RMA is attached to a rigid support structure [2, 7, 23].

The lateral dynamics of the system must be re-derived to include the dynamics of the RMAs attached at the tip and midpoint of the truss. Barker [2] and Shepherd [20] performed the derivation of the dynamic system equations of motion for the truss and RMAs. The truss is modeled as a mass-spring-damper system due to the simplicity of implementing the results into the MAPMODES finite element code. MAPMODES is a finite element code developed by Hallauer [6, 7] which is discussed in detail in Section 2.4. For simplicity, the mass of the RMA magnet is assumed to be insignificant and is neglected in the derivation. A diagram of the RMA attached to a node of the truss is shown in Figure 2.4 and defines the variables used throughout the derivation of the equations of motion [20].

The following equations were derived by Shepherd utilizing the Lagrangian method to obtain equations of motion of the RMAs [15, 20].

$$\mathcal{L} = T - V = \frac{1}{2}m_a\dot{x}_a^2 + \frac{1}{2}m_s\dot{x}_s^2 - \frac{1}{2}k_a(x_a - x_s)^2 - \frac{1}{2}k_sx_s^2 \quad (2.15)$$

For the coordinate  $x_s$ :

$$\begin{aligned} \frac{\partial \mathcal{L}}{\partial x_s} &= k_a(x_a - x_s) - k_sx_s \\ \frac{\partial \mathcal{L}}{\partial \dot{x}_s} &= m_s\dot{x}_s \\ \frac{d}{dt} \frac{\partial \mathcal{L}}{\partial \dot{x}_s} &= m_s\ddot{x}_s \\ Q_{x_s, n.c.} &= -c_s\dot{x}_s + c_a(\dot{x}_a - \dot{x}_s) + f_b(t) \end{aligned}$$

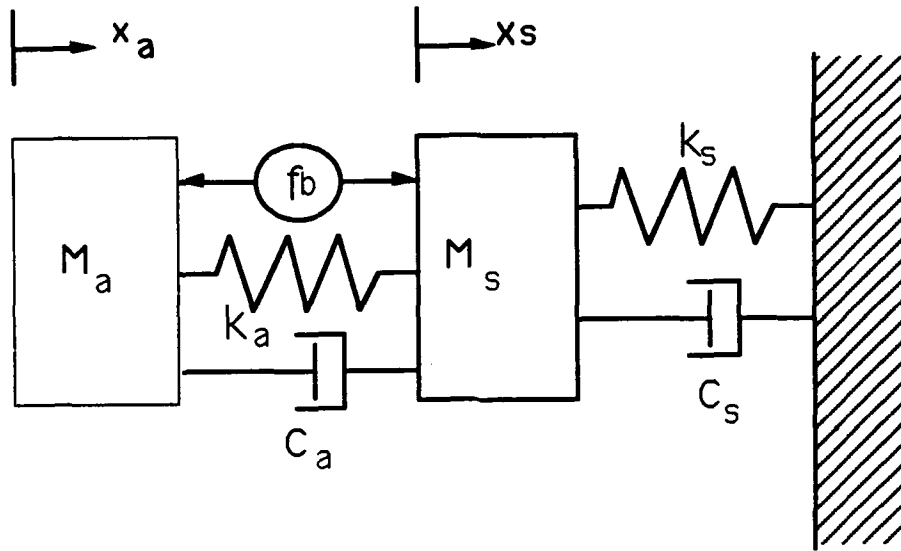


Figure 2.4: RMA Attached to a Truss Node

For the coordinate  $x_a$ :

$$\begin{aligned}\frac{\partial \mathcal{L}}{\partial x_a} &= -k_a(x_a - x_s) \\ \frac{\partial \mathcal{L}}{\partial \dot{x}_a} &= m_a \dot{x}_a \\ \frac{d}{dt} \frac{\partial \mathcal{L}}{\partial \dot{x}_a} &= m_a \ddot{x}_a \\ Q_{x_a n.c.} &= -c_a(\dot{x}_a - \dot{x}_s) - f_b(t)\end{aligned}$$

The resulting equations of motion are [20]:

$$\frac{d}{dt} \frac{\partial \mathcal{L}}{\partial \dot{q}_r} - \frac{\partial \mathcal{L}}{\partial q_r} = Q_{r n.c.} \quad (2.16)$$

$$m_s \ddot{x}_s - k_a(x_a - x_s) + k_s x_s = -c_s \dot{x}_s + c_a(\dot{x}_a - \dot{x}_s) + f_b(t) \quad (2.17)$$

$$m_a \ddot{x}_a + k_a(x_a - x_s) = -c_a(\dot{x}_a - \dot{x}_s) - f_b(t) \quad (2.18)$$

The equations of motions may be re-written as [20]:

$$m_s \ddot{x}_s + c_s \dot{x}_s - c_a(\dot{x}_a - \dot{x}_s) - k_a(x_a - x_s) + k_s x_s = +f_b(t) \quad (2.19)$$

$$m_a \ddot{x}_a + c_a(\dot{x}_a - \dot{x}_s) + k_a(x_a - x_s) = -f_b(t) \quad (2.20)$$

Equation 2.20 is easily transcribed into the matrix form first shown by Barker [2]:

$$\begin{bmatrix} m_s & 0 \\ 0 & m_a \end{bmatrix} \begin{bmatrix} \ddot{x}_s \\ \ddot{x}_a \end{bmatrix} + \begin{bmatrix} c_s + c_a & -c_a \\ -c_a & c_a \end{bmatrix} \begin{bmatrix} \dot{x}_s \\ \dot{x}_a \end{bmatrix} + \begin{bmatrix} k_s + k_a & -k_a \\ -k_a & k_a \end{bmatrix} \begin{bmatrix} x_s \\ x_a \end{bmatrix} = \begin{bmatrix} 1 \\ -1 \end{bmatrix} f_b \quad (2.21)$$

Choosing a relative coordinate  $x_{as} = x_a - x_s$  facilitates the implementation of the model into MAPMODES. The coordinate transformation removes the dynamic coupling in Equation 2.21 in favor of an inertially coupled mass matrix. Equation 2.21 written in terms of the relative coordinate  $x_{as}$  is [2, 20]:

$$\begin{bmatrix} m_s + m_a & m_a \\ m_a & m_a \end{bmatrix} \begin{bmatrix} \ddot{x}_s \\ \ddot{x}_{as} \end{bmatrix} + \begin{bmatrix} c_s & 0 \\ 0 & c_a \end{bmatrix} \begin{bmatrix} \dot{x}_s \\ \dot{x}_{as} \end{bmatrix} + \begin{bmatrix} k_s & 0 \\ 0 & k_a \end{bmatrix} \begin{bmatrix} x_s \\ x_{as} \end{bmatrix} = \begin{bmatrix} 0 \\ -1 \end{bmatrix} f_b \quad (2.22)$$

The advantage of this model is that the damping appears only in the diagonal of the damping matrix. This reflects the importance of the relative velocity between the reaction mass and the structure within the control law [2]. The matrices in Equation 2.22 are used to augment the flexible structure's system matrices with the RMA's mass, damping, and stiffness parameters. The addition of the RMAs increases the system's degrees of freedom by two and is discussed in more detail in Section 2.4 and Section 2.4.2.

Each of the RMAs is individually characterized on a test jig in the "stand alone" configuration [20]. The RMA is attached to a force gage, which is fixed to the rigid wall of the test jig, with a metal stinger. The stinger is in turn connected to the RMA's magnet. The RMA rides on ball bearings in machined grooves in the test jig to maintain axial alignment. Using the HP dynamic signal analyzer, a swept sine characterization is performed utilizing the signal input to the RMA amplifiers, set to a gain of 2, and the force gage is used to measure the output. The swept sine

program adjusts the input signal to maintain an output force of 0.5 lbf over the entire frequency range, to ensure measurement accuracy, and to refrain from overstraining the force gage [20]. The model is modified with a second order filter to represent the force gage in the device characterization. The experimental and theoretical frequency response plots for the each RMA, tip and midpoint, were shown by Shepherd [20]. The theoretical values of the mass, stiffness, and damping coefficients were chosen, by Shepherd [20], to closely resemble the experimental results. The final block diagram of the RMA model is shown in Figure 2.5 and the experimentally determined coefficients are listed in Table 2.1 [20]. There is close agreement between the RMA model and the experimental results at frequencies below 100 rad/sec, which is the bandwidth of the force gage used in model characterization.

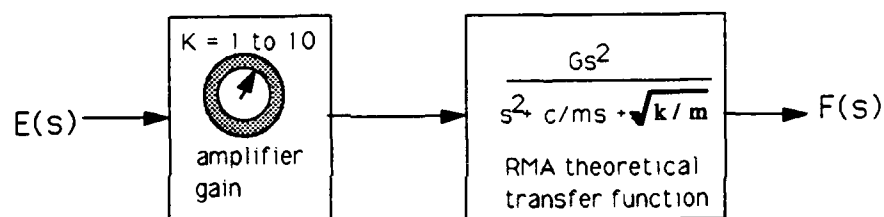


Figure 2.5: Block Diagram of RMA

Table 2.1: Experimentally Determined Values for RMA Models

constant	RMA tip	RMA midpoint
G	1 lbf/volt	1 lbf/volt
m	0.0097255 lbf $\frac{\text{sec}^2}{\text{in}}$	0.0097542 lbf $\frac{\text{sec}^2}{\text{in}}$
c	0.060 lbf sec/in	0.065 lbf sec/in
k	16.5 lbf/in	18.0 lbf/in
$\omega_n$	41.12 rad/sec	42.96 rad/sec
$\zeta$	0.0750	0.0776

## 2.4 Truss Modeling

A planar truss is considered to be one of the simplest forms of flexible structures. The truss can be modeled by considering its structure as an assembly of individual elements. If the forces and moments at the ends of each element are known from structural theory, the joints between the elements can be matched for compatibility of displacements. The forces at the joints can thus be determined by imposing equilibrium conditions on the system [21]. A finite element model (FEM) of the truss is a discrete approximation of the continuous system. Two FEM models of the truss will be developed: one is an eight order, two-input, model of the structure without RMAs and the second is a twelfth order, four-input model of the structure which includes the RMAs. The MAPMODES (Matrix Algebra Package / Structural MODES) Fortran code developed by Prof W.L. Hallauer at the United States Air Force Academy, CO, is used to determine the model with a finite number of degrees of freedom [6]. MAPMODES performs standard matrix algebra operations, calculates the mass and stiffness matrices for the truss system from the structural elements, solves for the static structural displacements by the matrix stiffness method, and solves the structural dynamics eigenvalue problem for natural frequencies, mode shapes, and generalized masses [6]. The finite element model is a system of first order, linear, differential equations of motion of the structure, known to control engineers as state space equations. The state space equations of the truss model can be reduced to facilitate control law design through the process of modal truncation. The reduced state space models are also augmented to include damping of the modes of the truss. The state space equations can then be evaluated to find the natural frequencies of the truss model and the approximate shapes of its bending modes. Experimental natural frequencies and mode shapes are compared to the finite element model results to verify the accuracy of the model.

### 2.4.1 Finite Element Model of the UWCSL Truss

Low order, linear finite element models of the UWCSL truss developed by Schulthess and Shepherd [19, 20] are the springboard for the two truss models used in this research. Both the existing and new finite element models are obtained through the MAPMODES program [6].

The complete truss structure is modeled as a combination of separate elements each input into MAPMODES. Each longeron and diagonal is modeled as a single-plane element with no bending freedom using standard stiffness and consistent mass matrices. The battens are modeled as rigid bar elements. The steel bars simply add to the batten inertia. The air jet thrusters and reaction mass actuators are also added to the structure by increasing the inertia at their connecting locations. The steel joints are assumed to be rigid. The properties of each of the truss members are assumed to be the same as the properties determined by Hallauer at USAFA [7] and are presented in Table 2.2.

Table 2.2: Average Mass and Stiffness Properties of Truss Members

Member	Orientation (deg)	Stiffness	Mass /Length ( $\frac{lb}{in^2}$ )	Length (in)
Diagonal	$\pm 45$	$6.14 \times 10^4$	$5.775 \times 10^{-5}$	19.69
Longitudinal	0	$9.71 \times 10^4$	$7.130 \times 10^{-5}$	13.92

In most finite element models, individual element coordinates and forces are transformed into global coordinates. These coordinate transformations ensure all input matrices are the same. In MAPMODES, the global coordinate system is based upon the center of gravity (CG) of each rigid batten. The various coordinate systems are shown in Figure 2.6 [19].

Coordinate system 1 is the orientation of the flexible truss elements as they exist in the actual hardware structure. The substructure stiffness and mass matrices, to be computed in MAPMODES, require the orientation of the truss members with respect to the x-axis and the length of the truss member in addition to the stiffness and mass of each member. A coordinate transformation,  $T_1$  (Equation 2.23), on system 1 is used to reduced the number of coordinates from four to three by realizing that  $y_1$  and  $y_2$  are identical (system 2).

$$T_1 = \begin{bmatrix} 1 & 0 & 0 \\ 0 & 1 & 0 \\ 0 & 0 & 1 \\ 0 & 1 & 0 \end{bmatrix} \quad (2.23)$$

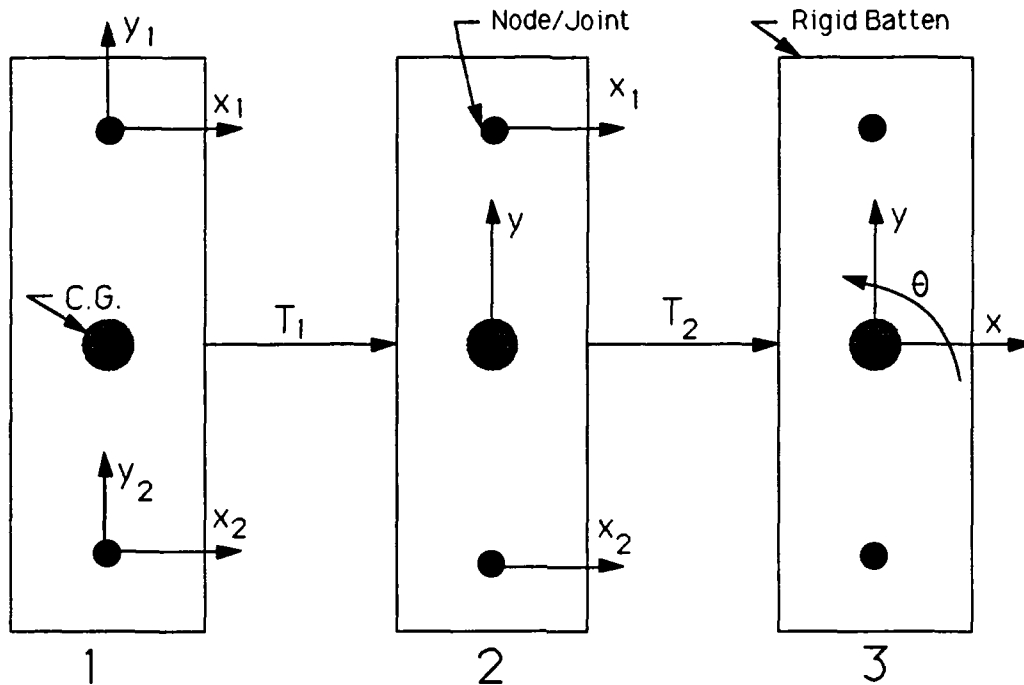


Figure 2.6: MAPMODES Coordinate Systems and Transformations

$T_2$  (Equation 2.24) is the coordinate transform used to obtain the C.G. coordinate system (3) from system 2. The final coordinates are  $x$ ,  $y$ , and  $\theta$ , where  $x$  indicates longitudinal translation,  $y$  transverse translation,  $\theta$  tip angular rotation, and  $c = 13.92$  [2].

$$T_2 = \begin{bmatrix} \frac{1}{2} & 0 & \frac{1}{2} \\ 0 & 1 & 0 \\ 0 & 0 & 1 \\ -\frac{1}{c} & 0 & \frac{1}{c} \end{bmatrix} \quad (2.24)$$

Data can be entered into the MAPMODES file in any coordinate system; however, the appropriate transformations to achieve the final solution in terms of C.G. coordinates must be performed.

The hub of the truss (station 0) is not truly fixed, but is constrained by a steel box beam attached to a steel table which is anchored into the concrete floor. The effect of the constraining structure on the flexible modes of the truss is approximated using the results obtained by Hallauer [8]. These results are from the truss at the

United States Air Force Academy, CO. The natural frequencies of the USAFA table were measured and using known geometry, mass, and rotational inertia, the stiffness values of the transverse and longitudinal constraints were inferred [8]. The UWCSL truss is attached directly to the box beam on the table while the USAFA truss is mounted directly to the table. The box beam is less stiff than the table; therefore, Schulthess and Shepherd modified the USAFA mass matrices to match the experimental UWCSL structure to the finite element model. The values for the constraining table found through this process have not been modified and present an uncertainty in the modeling process. The constraining table mass and stiffness matrices, as determined by Schulthess and Shepherd, are given in the C.G. coordinate system and presented in Equation 2.25 and Equation 2.26. The scalar values in front of the respective matrices are the scale factors used to match experimental data with the FEM for the UWCSL truss.

$$T_{mass} = 0.1 \times \begin{bmatrix} 1.238 & 0 & 0.0188 \\ 0 & 1.241 & -12.083 \\ 0.0188 & -12.083 & 248.78 \end{bmatrix} \quad (2.25)$$

$$T_{stiff} = 0.25 \times \begin{bmatrix} 2.862 \times 10^5 & 0 & 3.788 \times 10^4 \\ 0 & 1.958 \times 10^5 & -2.349 \times 10^6 \\ 3.788 \times 10^4 & -2.349 \times 10^6 & 8.020 \times 10^7 \end{bmatrix} \quad (2.26)$$

The next step is to supplement each of the truss nodes with inertia due to the addition of steel battens to lower the natural frequency of the structure. The new inertia at each node includes the rigid steel batten, a chordwise longitudinal truss member, two steel node joints, a bolt/washer combination, and two stainless steel plates glued to the bottom of the rigid batten to provide a smooth surface for the ball bearings [19]. The mass matrix, as determined by Schulthess, for the steel bar assembly in C.G coordinates is

$$M_{sb} = \begin{bmatrix} m & 0 & 0 \\ 0 & m & 0 \\ 0 & 0 & I_{zz} \end{bmatrix} \quad (2.27)$$

where the mass was measured to be  $0.0281 \frac{\text{lb}_f \text{s}^2}{\text{in}}$  and the moment of inertia of the

rigid batten  $I_{zz} = 0.690 \text{ lb}_f \text{s}^2 \text{in}$  [19].

The final addition to the MAPMODES input file is the matrix of concentrated masses of colocated air jet thruster/accelerometer combinations and the reaction mass actuator/accelerometer combinations attached at the tip and midpoint of the planar truss. The assumption is made that the AJTs are located at the joint and the accelerometer mass is lumped at a node. The matrix of concentrated masses for the accelerometer and AJT in C.G coordinates is

$$M_{AJT/Accel} = \begin{bmatrix} 2.804 \times 10^{-3} & 5.609 \times 10^{-3} & 7.559 \times 10^{-5} \end{bmatrix}. \quad (2.28)$$

The units for each element in  $M_{AJT/Accel}$  are  $\frac{\text{lb}_f \text{s}^2}{\text{in}}$ .

The reaction mass actuator (RMA)/accelerometer structure is also assumed to be attached to the joint at a node. The matrix of concentrated masses for the RMA and accelerometer in C.G. coordinates is

$$M_{RMA/Accel} = \begin{bmatrix} 2.804 \times 10^{-3} & 9.7255 \times 10^{-3} & 9.7452 \times 10^{-3} \end{bmatrix}. \quad (2.29)$$

The units for each element in  $M_{RMA/Accel}$  are  $\frac{\text{lb}_f \text{s}^2}{\text{in}}$  [20, 19]. The addition of the RMAs to the tip and midpoint of the truss adds 2 DOF to the system model and increases the number of inputs to the system by two. When augmented with the truss, the RMAs (mass-spring-dampers) reduce the response of structural modes and impose passive damping on the system.

From this input data, MAPMODES generates a 63 degree of freedom (DOF) model of the UWCSL truss, 3 DOF for each of the 21 battens (longitudinal translation ( $x$ ), transverse translation ( $y$ ), and rotation ( $\theta$ )). The 63 DOF linear model is a hundred and twenty-sixth order, two-input state space equation. The full-order, undamped FEM can be represented as the eigenvalue problem:

$$[M]\ddot{\mathbf{q}} + [K]\mathbf{q} = \mathbf{f}. \quad (2.30)$$

$[M]$  and  $[K]$  are the positive definite consistent mass and stiffness matrices.  $\mathbf{q}$  is the vector of generalized coordinates and  $\mathbf{f}$  is the vector of force and torque inputs [2].

### 2.4.2 Model Reduction

The high-order model generated by MAPMODES is difficult to implement and is computationally inefficient due to the large number of calculations required to process the state equations. The prime objective in model reduction is to achieve an accurate approximation of the high-order system with low-order models [12]. Low-order designs reduce the complexity of the system and facilitate low-order controller designs. An example is the LQ controller which is the same order as the plant and therefore, the system, without filters, is of order  $2n$ . Besides being easier to work with, low-order models facilitate the study of the dynamics of interest in the system.

There are many model reduction methods, each with its own algorithm and error criteria, which can be implemented to form low-order models, of order  $n_r$ . The method of modal truncation, described by Barker [2], reduces the full-order model to a reduced order model ( $2n_r < 2n$ ) using a procedure which preserves the dynamic response of the full-order model for the  $n_r$  selected DOF and the  $n_r$  selected modes. The procedure requires the solution of the generalized free vibration eigenvalue problem

$$[M]\ddot{\mathbf{q}} + [K]\mathbf{q} = \mathbf{0}. \quad (2.31)$$

MAPMODES solves the eigenvalue-eigenvector problem to determine the natural frequencies and mode shapes of the system. It is known that  $[M]$  and  $[K]$  are matrices and  $(\ddot{\mathbf{q}})$  and  $(\mathbf{q})$  are vectors, thus, for mathematical manipulation, the brackets in the eigenvalue problem are eliminated. Premultiplying Equation 2.31 by  $M^{-1}$ , the following terms are obtained:

$$M^{-1}M = I \quad (\text{the identity matrix})$$

$$M^{-1}K = A \quad (\text{the system matrix})$$

and

$$I\ddot{\mathbf{q}} + A\mathbf{q} = \mathbf{0}. \quad (2.32)$$

The system matrix ( $A$ ) defines the dynamic properties of the system and is generally not symmetric [21]. Assuming harmonic motion,  $\ddot{\phi} = -\lambda\phi$ , where  $\lambda = \omega^2$ , Equation 2.32 becomes

$$[A - \lambda I]\phi = \mathbf{0} \quad (2.33)$$

The characteristic equation of the system is the determinant equated to zero:

$$\det[A - \lambda I] = |A - \lambda I| = 0 \quad (2.34)$$

The roots ( $\lambda_i$ ) of the characteristic equation are the eigenvalues. The positive square root of the eigenvalues are the natural frequencies ( $\omega$ ) of the system. By substituting  $\lambda_i$  into the matrix equation, Equation 2.33, the eigenvector ( $\phi$ ) or corresponding normalized mode shape is obtained [21]. Only for the values of  $\omega$  which solve Equation 2.33 is there a non-zero solution for the eigenvectors. The number of eigenvalues and eigenvectors is equal to the number of degrees of freedom of the system.

The vector of eigenvalues can be transformed into a diagonal matrix ( $\Lambda$ ) by multiplying it with an identity matrix.

$$\Lambda = \text{diag}(\omega_1^2, \omega_2^2, \dots, \omega_n^2) \quad (2.35)$$

The corresponding eigenvector matrix, ( $\Phi$ ), is called the modal matrix.

The modal truncation procedure extracts the  $n_r$  selected modes from the matrix of eigenvalues. The large displacement and acceleration forces excited in the first four lateral bending modes of the truss are the dominant modes of the structure. The first four lateral bending modes are therefore retained for control law design during the model reduction process. Modal truncation involves removing an ( $n_r \times n_r$ ) matrix from the modal matrix. The reduced modal matrix rows correspond to the number of  $n_r$  selected DOF and the columns to the number of  $n_r$  selected modes [2]. The reduced set of dynamic equations becomes:

$$[M_r]\ddot{\mathbf{q}}_r + [K_r]\mathbf{q}_r = \mathbf{f}_r \quad (2.36)$$

where

$$M_r = \Phi_r^{-T} \Phi_r^{-1} \quad (2.37)$$

and

$$K_r = \Phi_r^{-T} \Lambda_r^2 \Phi_r^{-1} \quad (2.38)$$

$\mathbf{f}_r$  is the reduced vector of inputs corresponding to  $\mathbf{q}_r$ . The reduced eigenvalue matrix is  $\Lambda_r$  and the reduced modal matrix is  $\Phi_r$ . The method of modal truncation allows

the 63 DOF MAPMODES model to be reduced to a four DOF model (six DOF if the RMAs are included in the dynamics) in which the first four lateral vibrational modes are preserved.

### 2.4.3 Modeling of Truss Damping

The light damping of the structure must be included in the reduced dynamic equations to obtain an accurate model of the truss. The structural damping of the truss is modeled as linear viscous damping, ignoring non-linear Coulomb damping due to friction between the structure and ball-bearings [19]. The Coulomb damping is negligible except during small velocity excitation, which occurs primarily during the first bending mode [8]. It is assumed that no cross-coupling exists in the damping matrix such that viscous damping doesn't couple with undamped vibrational modes. The reduced dynamic equations can be supplemented to include viscous damping as [19, 20]:

$$[M_r]\ddot{q}_r + [C_r]\dot{q}_r + [K_r]q_r = f_r. \quad (2.39)$$

The reduced viscous damping matrix,  $C_r$ , is defined as

$$[C_r] = \Phi_r^{-T} [2\zeta\omega] \Phi_r^{-1} \quad (2.40)$$

where

$$[2\zeta\omega] = \text{diag}(2\zeta_s\omega_s) \text{ and } s = (1, 2, 3, 4). \quad (2.41)$$

and  $\zeta_r$  is the damping coefficient for each bending mode of the truss. The damping coefficients ( $\zeta_r$ ) can only be determined experimentally. The experimental approach for obtaining the damping coefficients is described in Section 2.5.1. The damping coefficients are subject to experimental variations and the model must be adjusted to incorporate these changes. The damping coefficients used in the models in this thesis, to more accurately simulate the damping of the actual truss at the time of experimentation, are in Table 2.4.

The final reduced order dynamic equations can be transformed into multi-input, multi-output (MIMO) state space models depending on the system configuration.

The next two sections describe the state space model configurations of the truss. The first configuration is an eighth order, two-input two-output, model without the RMAs attached which allows for AJT control actuation only. The second configuration is a twelfth order, four-input four-output, model for the truss with RMAs attached to the truss tip and midpoint which allows for both AJT and RMA actuation, either independent or hybrid.

#### 2.4.4 Eighth Order State Space Model

The reduced eighth order, two-input, dynamic equations can be transformed into state space form with the following structure:

$$\dot{\mathbf{x}} = \mathbf{Ax} + \mathbf{Bu} \quad (2.42)$$

$$\mathbf{Y} = \mathbf{Cx} + \mathbf{Du}. \quad (2.43)$$

$\mathbf{x}$  are the states, corresponding to the DOF in the reduced model, and  $\mathbf{u}$  is the vector of force inputs into the model.  $\mathbf{Y}$  is the output vector which is user defined.

Equation 2.39 can be transformed into the state space format by first multiplying by  $M_r^{-1}$  and isolating the highest derivative term,  $\ddot{\mathbf{q}}_r$ .

$$\ddot{\mathbf{q}}_r = -M_r^{-1}C_r\dot{\mathbf{q}}_r - M_r^{-1}K_r\mathbf{q}_r + M_r^{-1}\mathbf{f}_r \quad (2.44)$$

The next step is to reduce the second order linear equation into two first order equations. The state vector  $\mathbf{x}$  used to accomplish this can be defined as

$$\mathbf{x} = \begin{bmatrix} \dot{\mathbf{q}}_r \\ \mathbf{q}_r \end{bmatrix} = \begin{pmatrix} q_{tip} \\ q_{3/4} \\ q_{mid} \\ q_{1/4} \\ q_{tip} \\ q_{3/4} \\ q_{mid} \\ q_{1/4} \end{pmatrix} \quad (2.45)$$

$\mathbf{q}_r$  and  $\dot{\mathbf{q}}_r$  are each four element vectors corresponding to the specific generalized coordinates and their velocities which are retained in the reduced order truss model. The inputs are the force inputs from the AJTs at the truss tip and midpoint.

$$u = \begin{pmatrix} u_1 \\ u_2 \end{pmatrix} = \begin{pmatrix} f_{tip} \\ f_{mid} \end{pmatrix} \quad (2.46)$$

The resulting eighth order linear state equations are of the form (with  $I_4$  the 4 x 4 identity matrix and  $O_4$  the 4 x 4 null matrix):

$$\frac{d}{dt} \begin{bmatrix} \dot{q}_r \\ q_r \end{bmatrix} = \begin{bmatrix} -M_r^{-1}C_r & -M_r^{-1}K_r \\ I_4 & O_4 \end{bmatrix} \quad (2.47)$$

The C and D matrices are user defined to output the truss acceleration, velocity, and displacement based on the sensor locations on the truss. The numerical values which constitute the eighth order A and B matrices for the truss model are presented in Appendix B.

#### 2.4.5 Twelfth Order State Space Model

As with the eighth order model, the twelfth order, four-input, truss model dynamic equations can be transformed into state space format (see Equation 2.4.4). The state vector  $\mathbf{x}$  used in this model can be defined as

$$\mathbf{x} = \begin{bmatrix} \dot{\mathbf{q}}_r \\ \mathbf{q}_r \end{bmatrix} = \begin{pmatrix} \dot{q}_{tip} \\ \dot{q}_{3/4} \\ \dot{q}_{mid} \\ \dot{q}_{1/4} \\ \dot{q}_{5-1} \\ \dot{q}_{6-3} \\ q_{tip} \\ q_{3/4} \\ q_{mid} \\ q_{1/4} \\ q_{5-1} \\ q_{6-3} \end{pmatrix} \quad (2.48)$$

The truss stations' velocities and displacements have the same variable labels as the eighth order model in Section 2.4.4. Two new variables,  $q_{5-1}$  and  $q_{6-3}$  are the relative displacements between the reaction mass actuator positions and the corresponding truss position at the tip and midpoint. The first two inputs are the force inputs from the AJTs at the truss tip and midpoint. The second two inputs are the relative forces applied to both the truss station and the RMAs at each of the respective stations.

$$u = \begin{pmatrix} u_1 \\ u_2 \\ u_3 \\ u_4 \end{pmatrix} = \begin{pmatrix} f_{tip} \\ f_{mid} \\ f_{5-1(tip)} \\ f_{6-3(mid)} \end{pmatrix} \quad (2.49)$$

The resulting twelfth order linear state equations are of the form (with  $I_6$  the 6 x 6 identity matrix and  $O_6$  the 6 x 6 null matrix):

$$\frac{d}{dt} \begin{bmatrix} \dot{q}_r \\ q_r \end{bmatrix} = \begin{bmatrix} -M_r^{-1}C_r & -M_r^{-1}K_r \\ I_6 & 0_6 \end{bmatrix} \quad (2.50)$$

The C and D matrices are also user defined to output the truss acceleration, velocity, and displacement at the chosen truss locations. The numerical values which constitute the twelfth order A and B matrices are presented in Appendix B.

## 2.5 Truss Model Validation

The finite element models (FEM) of the flexible structure can be theoretically validated using the Euler-Bernoulli beam theory. The beam theory provides a method for determining the upper bounds on the natural frequencies of the truss and an estimate of the first four bending mode shapes [19]. A detailed derivation of the Euler-Bernoulli beam theory is in Appendix C. The beam theory results are shown in Table 2.3 and the normalized mode shapes in Figure 2.11 along with the results of the FEM and experimental results.

Experimental verification of the truss is a method of validating the finite element models by comparing the theoretical, the simulation, and the experimental natural frequencies and mode shapes. There is no analytical method of determining the

modal damping of the truss; therefore, experimentation is the only method of determining the modal damping coefficients used in the modeling of the damping of the truss. The experimental results provide a foundation for fine tuning the reduced finite element model's damping to more precisely reflect the actual structure. There are two models of the truss (Sections 2.4, 2.4.4, and 2.4.5) and therefore two experimental configurations: one is a two-input, two-output structure without RMAs and the second is a four-input, four-output structure which includes the RMAs. Three experiments were conducted on the open loop UWCSL truss, to verify and fine tune the models. The tests were: swept sine resonant frequency determination, determination of the damping modal coefficients, and mode shape determination. Simulations of the truss models were performed using SIMULINK. The simulation results were obtained using the same techniques as the experimental procedures and were used for comparison with experimental results. The experimental procedures for each of the tests is detailed in Appendix D.

#### *2.5.1 Experimental Configuration without RMAs*

The UWCSL truss in this configuration has two accelerometers mounted directly to the structure, one at the tip and one at the midpoint. These two accelerometers provide the two inputs to the control laws. The actuators are the "back to back" air jet thruster pairs attached to the tip and midpoint of the truss. The three experimental tests were conducted on this truss configuration and the results were compared to the eighth order model developed in Section 2.4.4.

#### *Swept Sine Resonant Frequency Determination*

The resonant natural frequencies of the open loop truss were obtained using an HP dynamic signal analyzer's swept sine function. A fixed sine signal at a level of 0.05 volt peak was selected as the input signal to the tip AJTs of the truss. The acceleration signal from the tip accelerometer on the truss was measured. The result of the swept sine procedure was a Bode plot of the input signal to tip acceleration of the truss for the selected frequency range. A transfer function of the FEM of the truss, augmented with the AJT models, was calculated and its Bode plot determined. The experimental and FEM Bode plot of the truss without RMAs is shown in Figure 2.7. The shape of

Table 2.3: UWCSL Truss without RMAs: Resonant Natural Frequencies

Mode	Modal Frequencies (Hz)		
	Beam Theory	FEM	Truss Hardware
1	1.53	1.51	1.485
2	9.62	8.89	9.14
3	26.93	23.30	24.545
4	52.71	41.4	42.678

the Bode plots changed over different testing periods (as temperature, air pressure, dust on the ball bearings, etc. varied) but the peaks remained virtually constant. The peaks of the Bode plot are the resonant natural frequencies of the truss which are listed in Table 2.3. The experimental and FEM results show a close agreement in the overall shape of the magnitude portion of the Bode plot, especially as to the locations of the poles and zeros. The phase of the linear model drops more quickly than the experimental data due to the modeling of the AJTs. The bandwidth of the AJTs may be clearly seen, as the phase and magnitude of the truss plummet at 120 rad/sec in the experimental data, a phenomenon reflected by the linear model which rolls off at about 40 dB/decade and seeks 360 degrees of phase lag [20].

#### *Determination of Damping Coefficients*

Once the resonant natural frequencies of the truss have been found, the viscous damping coefficient for each mode can be determined. This was accomplished by exciting the truss at its resonant frequencies using the fixed sine function of an HP Dynamic Signal Analyzer (DSA). The input signal from the DSA was used to control the tip AJTs which, in turn, excited the bending modes of the truss. Acceleration at the truss tip and midpoint was recorded from the accelerometers at these respective positions. The input signal was shut off after a full range of motion was recorded by the accelerometers. The truss was then allowed to decelerate freely until it returned to its equilibrium state of zero acceleration. The results of this procedure are plots of free decaying acceleration signals at each of the modal frequencies. Figure 2.8 and Figure

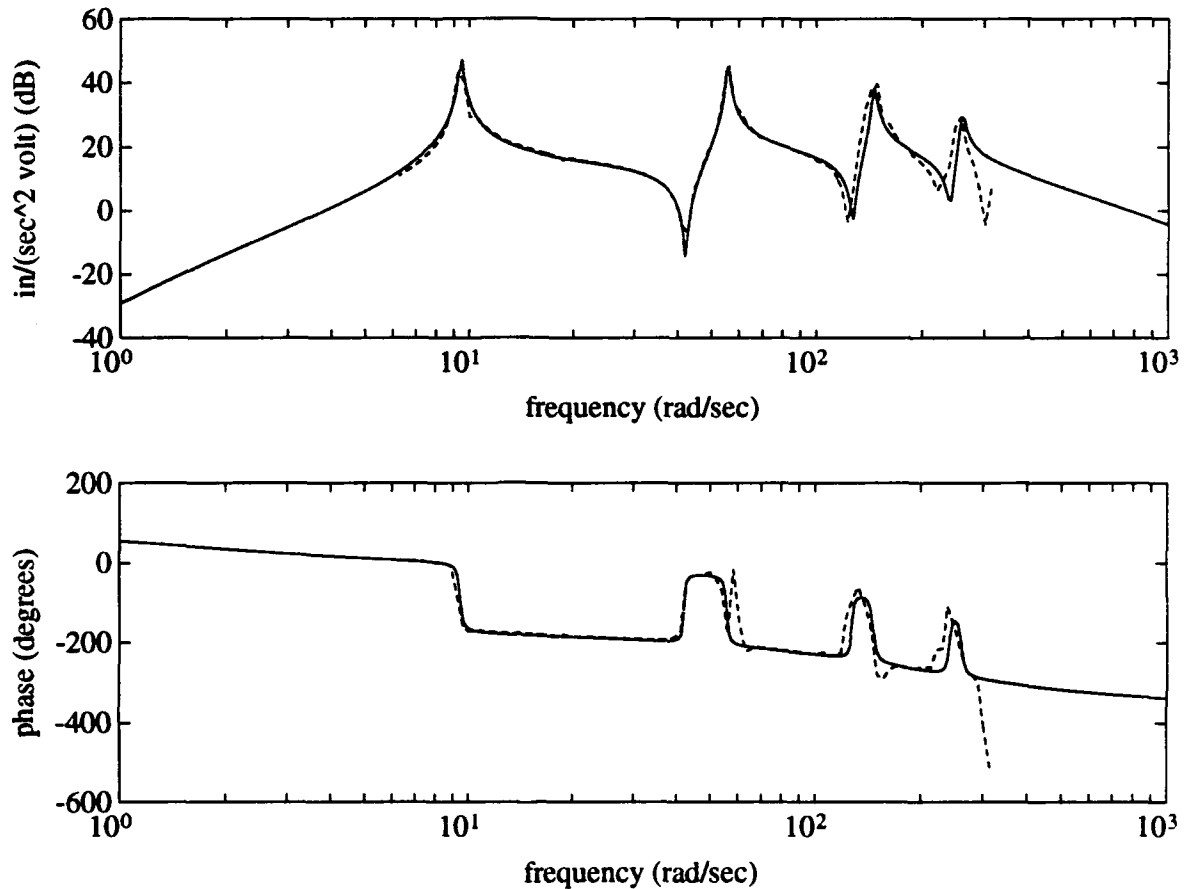


Figure 2.7: Frequency Response: Experimental(Dashed), FEM(Solid)

2.9 are the free decaying tip acceleration signals for the simulated and experimental UWCSL truss without the RMAs attached. The experimental accelerometer measurements are in volts/g and were converted to inches/sec<sup>2</sup> by the constant 9.9588 for comparison to the simulation results. The resolution of the plots does not reflect all of the other modes which were excited along with the specific resonant frequency for each mode. These harmonic mode accelerations are superimposed on the desired frequency signal and are the cause of the apparent "strange" behavior of the fourth mode's experimental results. The model assumes only linear, viscous damping, and is therefore subject to errors caused by non-linear Coulomb (dry-friction) damping and structural (hysteretic) damping [20].

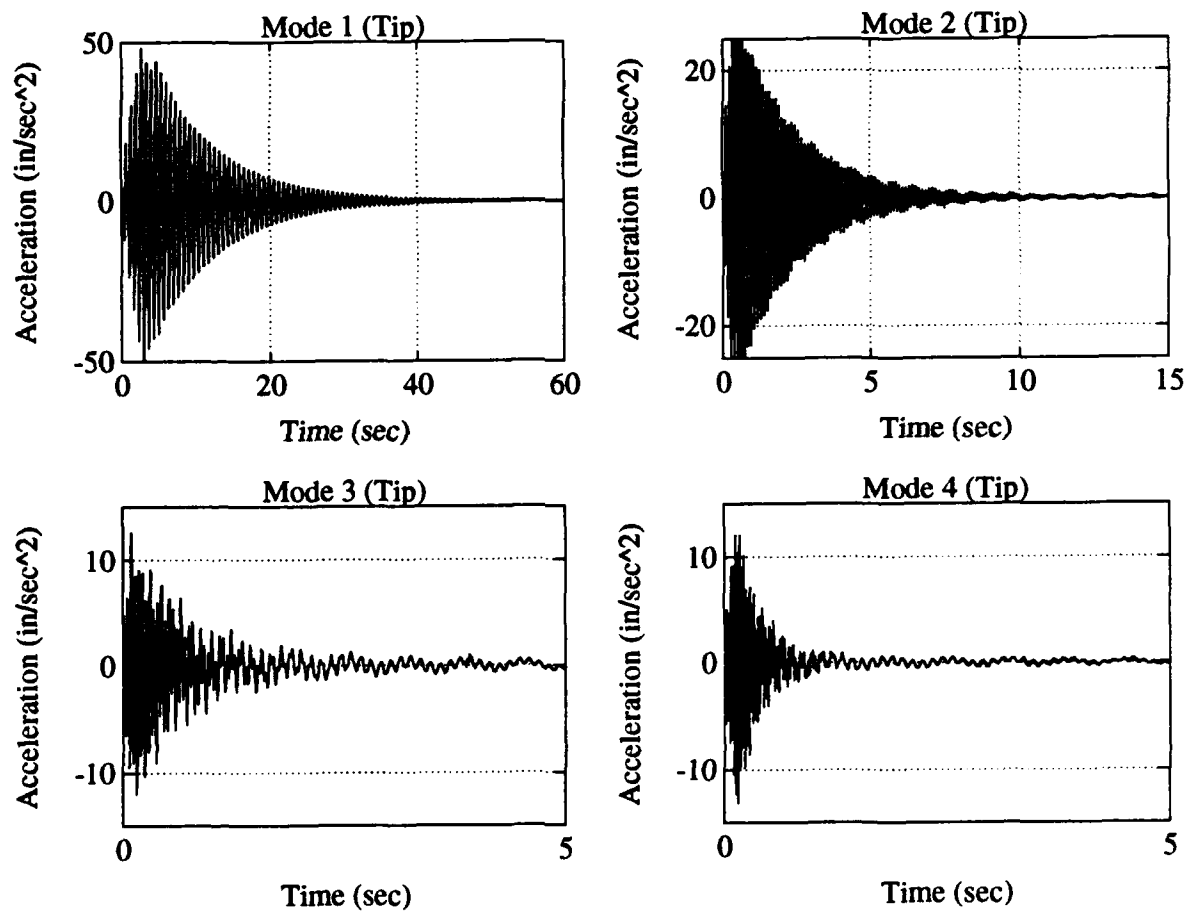


Figure 2.8: Tip Free Decay: Simulation without RMAs

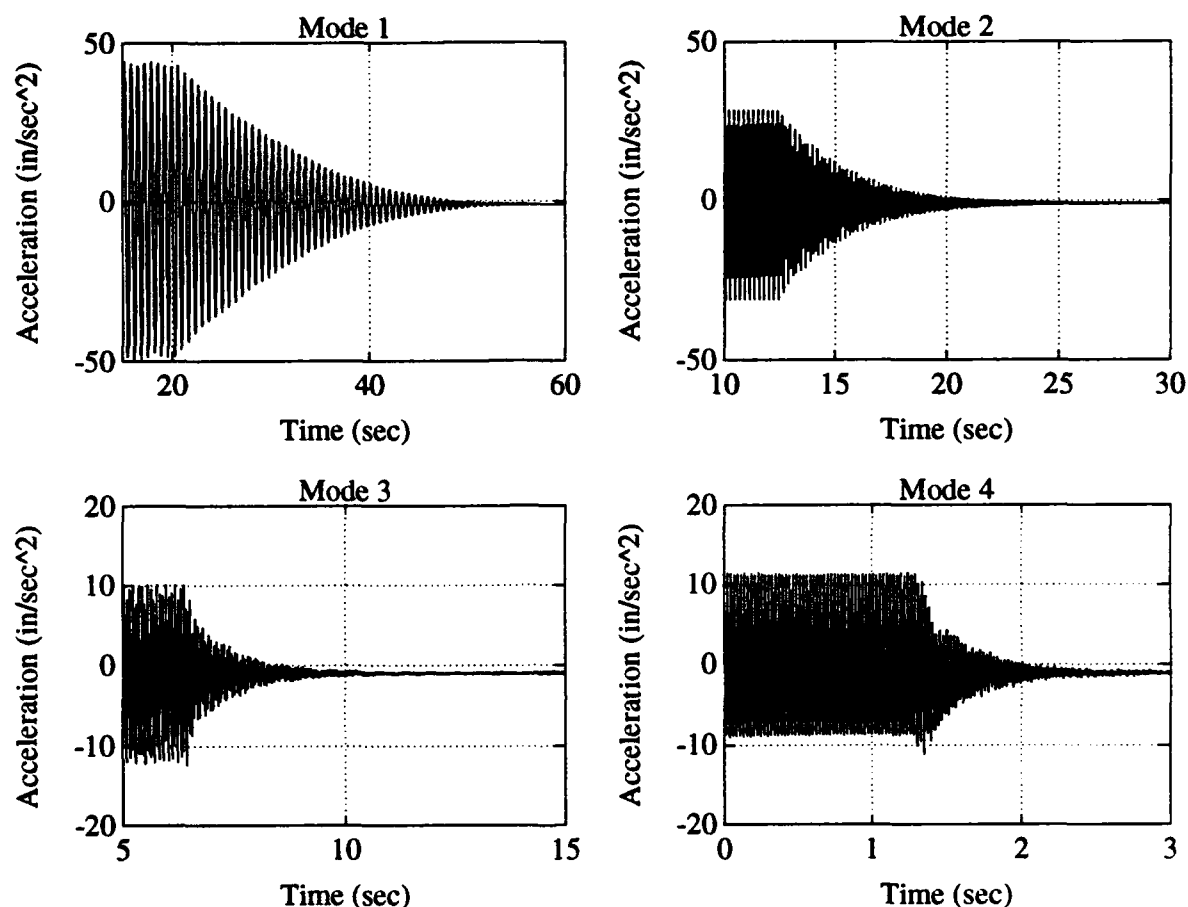


Figure 2.9: Tip Free Decay: Experimental Results without RMAs

Figure 2.8 and Figure 2.9 can be evaluated using different numerical techniques to determine the viscous damping coefficient at each of the modes. The logarithmic decrement method was applied to obtain the results in this thesis. The procedure is described by Thompson [21] and is outlined below.

Consider a viscously damped second order free vibration expressed by the general equation

$$x(t) = A \exp^{-\zeta \omega_n t} \sin(\sqrt{1 - \zeta^2} \omega_n t + \phi) \quad (2.51)$$

which is shown graphically in Figure 2.10. Introducing a new term, the logarithmic

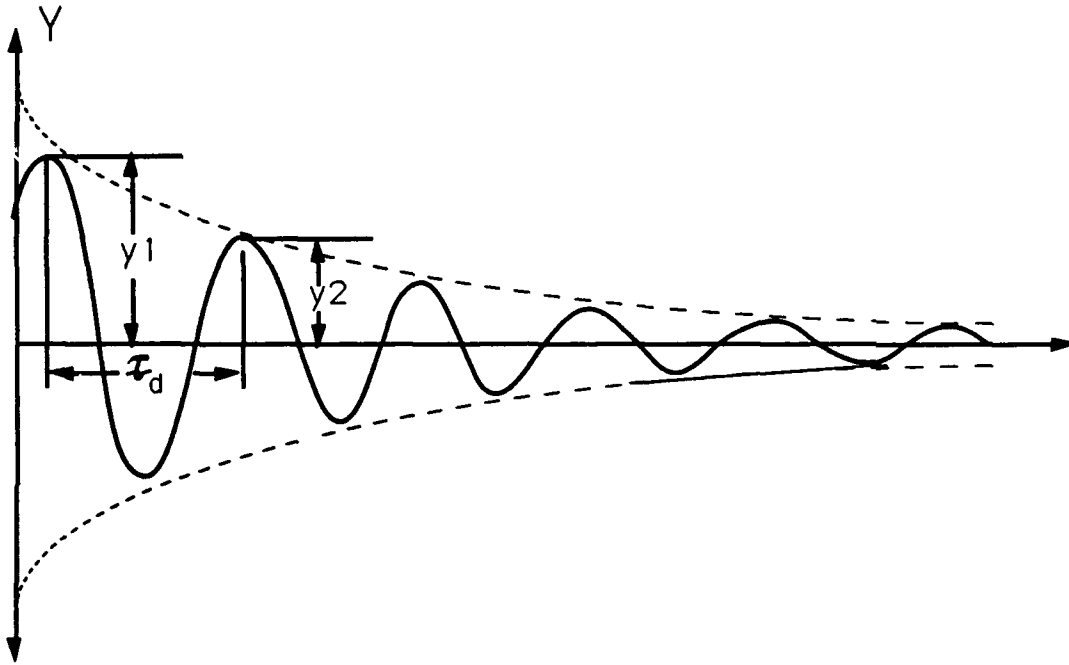


Figure 2.10: Second Order Free Vibration

decrement ( $\delta$ ), which is defined as the natural logarithm of the ratio of any two successive amplitudes, it is possible to measure the rate of decay of the oscillations. The logarithmic decrement ( $\delta$ ) can be expressed as [21]:

$$\delta = \ln \frac{x_1}{x_2} = \ln \frac{\exp^{-\zeta\omega_n t_1} \sin(\sqrt{1-\zeta^2}\omega_n t_1 + \phi)}{\exp^{-\zeta\omega_n(t_1+\tau_d)} \sin(\sqrt{1-\zeta^2}\omega_n(t_1 + \tau_d) + \phi)} \quad (2.52)$$

The sine terms are equal for multiples of  $n\tau_d$ , therefore Equation 2.52 reduces to:

$$\delta = \ln \frac{\exp^{-\zeta\omega_n t_1}}{\exp^{-\zeta\omega_n(t_1+\tau_d)}} \quad (2.53)$$

which may be simplified to yield:

$$\delta = \ln \exp^{\zeta\omega_n \tau_d} = \zeta\omega_n \tau_d = \zeta\omega_n \frac{2\pi}{\omega_d} \quad (2.54)$$

The damped natural frequency  $\omega_d$  is equal to  $\omega_n \sqrt{1-\zeta^2}$  and therefore Equation 2.54 becomes

$$\delta = \frac{2\pi\zeta}{\sqrt{1-\zeta^2}} \quad (2.55)$$

By rearranging the terms in the exact exact equation, the damping ratio can be defined as

$$\zeta = \frac{\delta}{\sqrt{4\pi^2 + \delta^2}} \quad (2.56)$$

For lightly damped structures, the logarithmic decrement between peaks is small and the expression

$$\zeta = \frac{\delta}{2\pi} \quad (2.57)$$

may be used with minimal loss of accuracy. A similar mathematical approach for decaying signals with peaks separated by  $n$  cycles results in the logarithmic decrement method being expressed as [20]:

$$\delta = \frac{1}{n} \ln \frac{x_1}{x_{n+1}} \quad (2.58)$$

Although the damping coefficients are derived for the displacement signal of Figure 2.10, the acceleration signals of the truss will decay in the same logarithmic proportion as the displacement signal for low frequency, lightly damped modal vibrations [20]. The logarithmic decrement method can therefore be used to determine the damping coefficient of the UWCSL truss. To realize an average logarithmic decrement  $\delta$  the peaks measured are at 90 percent and 10 percent of full displacement amplitude and Equation 2.58 is applied where  $n$  cycles are counted between the two measurement points. The truss midpoint and tip values of each of the two truss configurations were averaged to obtain the damping coefficients of the truss without RMAs ( $\zeta_{AJT}$ ). The damping coefficients are shown in Table 2.4. These values were incorporated into the modeling process to represent viscous damping of each mode of the truss as discussed previously in Section 2.4.3. The damping ratios of the third and fourth modes are not as accurate as the first two modes due to the use of the log decrement method and the multiple modes measured by the accelerometers at the higher natural frequencies. Table 2.4 also shows the settling time of the acceleration signal from controller activation to equilibrium.

### *Mode Shape Determination*

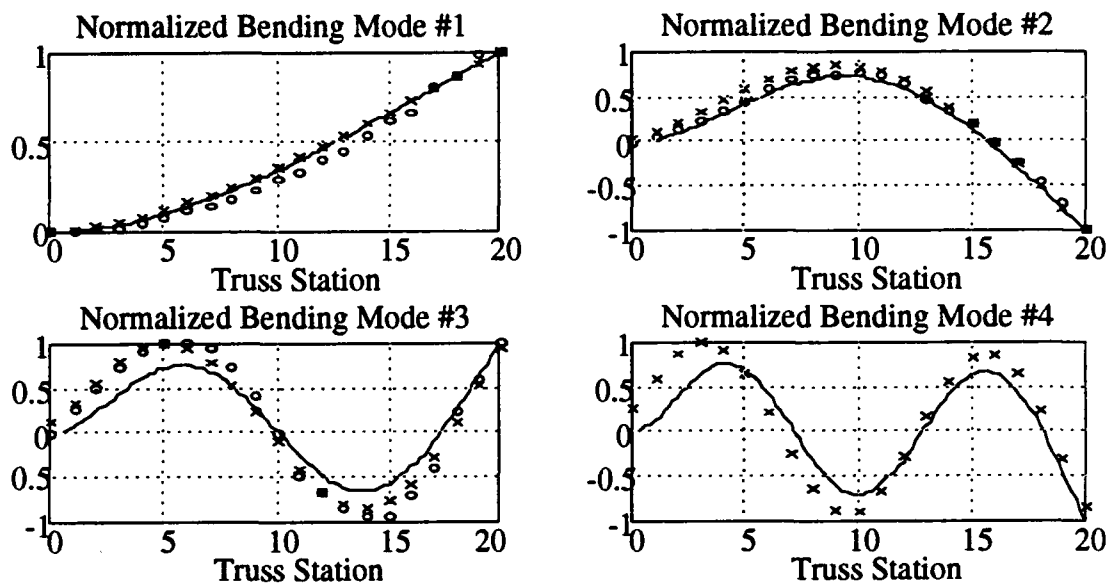
The mode shapes of the truss, without the RMAs attached, were obtained by exciting the truss, with a fixed sinusoidal signal to the tip AJTs, at its first three resonant frequencies. The lateral displacement of the truss at each of the twenty truss bays was measured using an Electro-Mike position sensor. By normalizing the peak values of displacement at each of the nodes to the point of greatest displacement, the mode shape at each of the resonant frequencies was determined. The fourth bending mode of the truss consisted of displacements below the noise threshold of the position sensor, and so only the first three modes were measured for FEM validation [20]. Figure 2.11 shows the experimental bending modes of the UWCSL truss plotted with the beam theory and reduced finite element model predictions.

### *2.5.2 Experimental Configuration with RMAs*

The UWCSL truss in this configuration has two accelerometers mounted directly to the structure, one at the tip and one at the midpoint, and two accelerometers mounted on the RMAs. The four accelerometers provide the inputs to the control laws for differential acceleration. The actuators are the "back to back" air jet thruster pairs and the RMAs attached to the tip and midpoint of the truss. The swept sine resonant frequency determination and the determination of the damping modal coefficients tests were conducted on this truss configuration. The mode shape determination was not performed for this configuration. The results were compared to the twelfth order

Table 2.4: UWCSL Truss without RMAs: Experimentally Determined Damping Ratios  $\zeta_{AJT}$

Mode	$\zeta_{AJT}$	Settling Time
1	0.01190	35.75
2	0.00863	12.84
3	0.01307	4.80
4	0.01555	1.44



Beam Theory ("x"es), Experimental ("o"s), and FEM(solid)

Figure 2.11: UWCSL Truss: Normalized Mode Shapes

model developed in Section 2.4.5.

The addition of RMAs to the truss reduces the response of structural modes and imposes passive damping on the system. The damping ratio of a structural mode of interest can be increased by matching the frequency of the RMAs to the truss bending mode frequency and positioning the RMAs at points of maximum modal displacement [16]. On the UWCSL truss, the RMAs act at positions of maximum displacement for the second mode (see Figure 2.11). The natural frequencies of the RMAs occur at 6.544 Hz for the tip RMA and 6.837 Hz for the midpoint RMA [20], both of which are approximately 2.5 Hz below the second mode and above the first bending mode. Therefore, the RMAs add significant damping to the second bending mode of the truss.

#### *Swept Sine Resonant Frequency Determination*

The same swept sine resonant frequency determination procedure, described in Section 2.5.1, was applied to the truss configuration with the RMAs attached. A fixed sine signal at a level of 0.05 volt peak was selected as the input signal to the tip AJTs

of the truss. The acceleration signal from the tip accelerometer on the truss was measured. The experimental and FEM Bode plots of the truss with the RMAs attached are shown in Figure 2.12. The resonant natural frequencies are the peaks of the Bode plot and are listed in Table 2.5. The addition of the RMAs to the structure changed the resonant natural frequency of the second mode due to the additional mass and passive damping of the RMAs and accelerometer structure. The experimental and FEM results show a close agreement in the overall shape of the magnitude portion of the Bode plot.

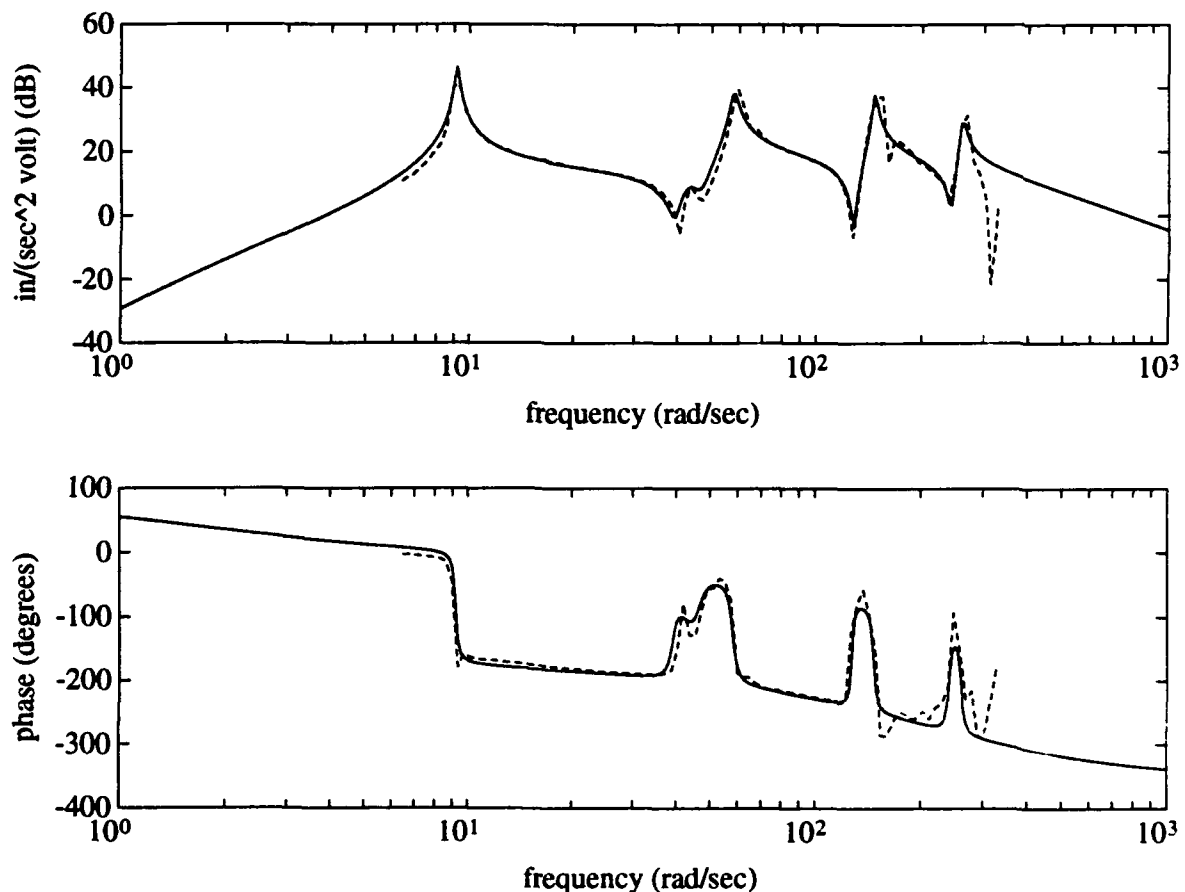


Figure 2.12: Frequency Response: Experimental(Dashed), FEM(Solid)

Table 2.5: UWCSL Truss with RMAs: Resonant Natural Frequencies

Mode	Natural Frequency (Hz)
1	1.485
2	9.508
3	24.545
4	42.678

#### *Determination of Damping Coefficients*

Using the resonant natural frequencies of the truss found from Figure 2.12, the viscous damping coefficient for each mode can be determined using the same procedure described in Section 2.5.1. Figure 2.13 and Figure 2.14 are the free decaying tip acceleration signals for the experimental and simulated UWCSL truss with the RMAs attached. Notice that the magnitude of the acceleration is lower for the RMA augmented truss than the truss without RMAs due to the passive damping of the RMAs.

Figure 2.13 and Figure 2.14 can also be evaluated using the logarithmic decrement method described in Section 2.5.1. The resulting damping coefficients of the RMA augmented truss ( $\zeta_{RMA}$ ) are shown in Table 2.6 along with the settling time of the acceleration signal from controller activation to equilibrium. The fourth column of Table 2.6 reflects the changes in the damping ratio between the two truss configurations. The  $\log_{10}$  of the ratio of the damping coefficients of the truss with RMAs to the damping coefficients of the truss without RMAs is used in favor of percentages because of the large increases in damping which is achieved [20]. The final column is the difference between the settling times of the truss without RMAs and the truss with RMAs. The damping ratios of the third and fourth modes involve more experimental error than the first two modes due to the use of the log decrement method and the multiple modes measured by the accelerometers at the higher natural frequencies.

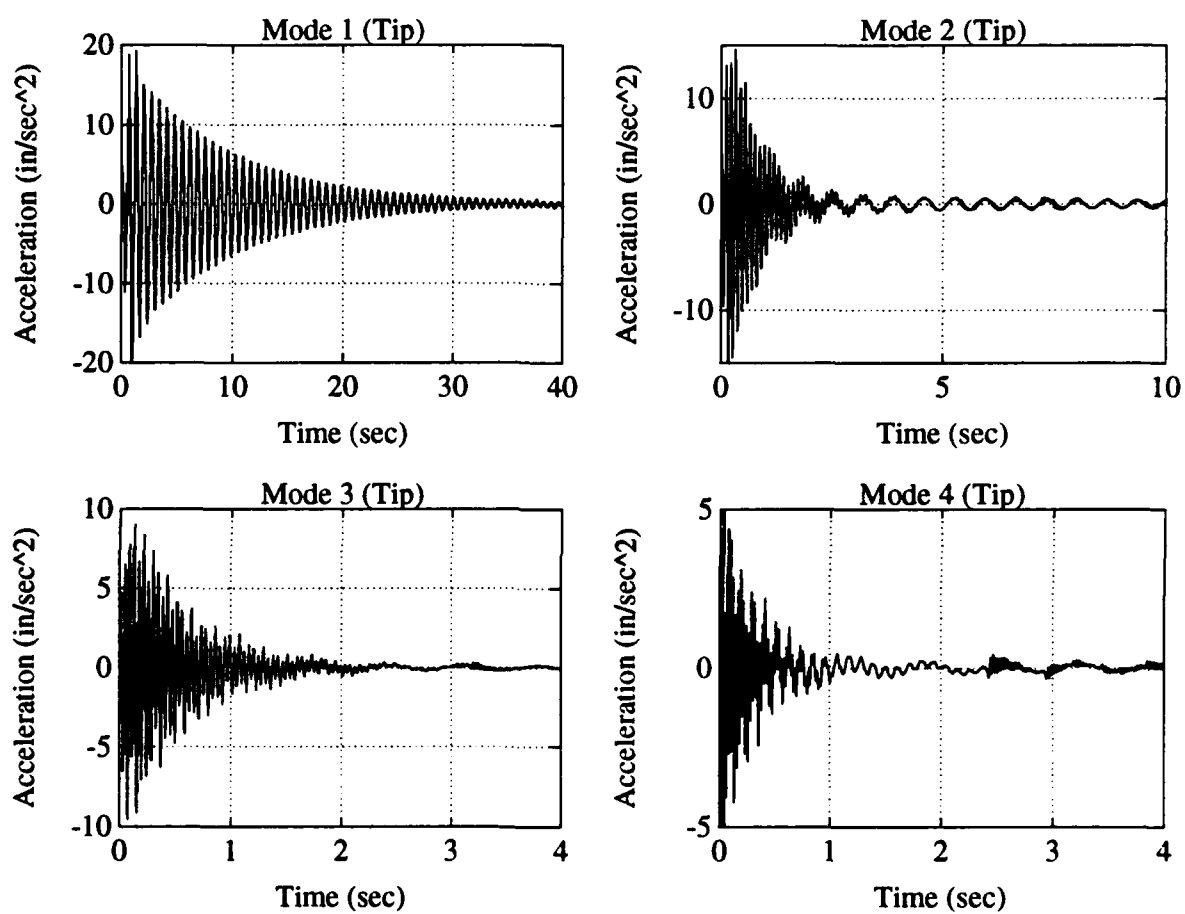


Figure 2.13: Tip Free Decay: Simulation with RMAs

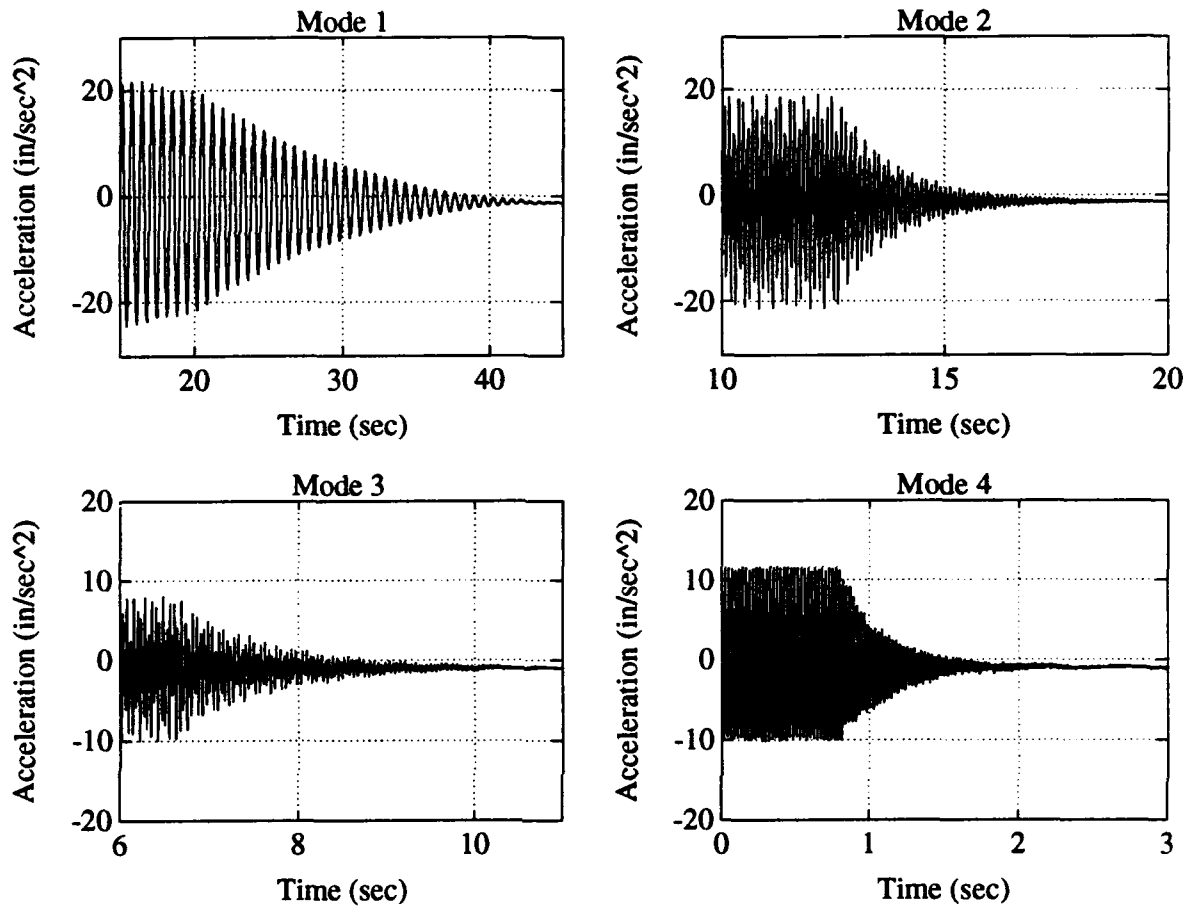


Figure 2.14: Tip Free Decay: Experimental Results with RMAs

Table 2.6: UWCSL Truss with RMAs: Experimentally Determined Damping Ratios ( $\zeta_{RMA}$ )

Mode	$\zeta_{RMA}$	Settling Time	$\log \left[ \frac{\zeta_{RMA}}{\zeta_{AJT}} \right]$	$\Delta$ Time
1	0.01800	30.38	0.17970	3.37
2	0.01801	7.41	0.31943	5.43
3	0.01531	4.05	0.06859	0.75
4	0.01270	1.61	-0.08796	-0.17

## Chapter 3

# CLASSICAL ANALOG CONTROL LAW SYNTHESIS AND VALIDATION

### *3.1 Overview*

The system models of the UWCSL flexible truss, configured with and without RMAs, were theoretically developed and experimentally verified with results reported in Chapter 2. The close approximation of the models to the actual truss hardware allows for more precise and efficient control law design and it is expected that there will be good agreement between the simulation and experimental results.

The simplest type of vibration control with on-off actuators is active damping which emulates ideal Coulomb friction thus increasing the damping ratio of lightly damped systems[7]. This type of vibration control is accomplished through negative velocity feedback in a closed loop system. The velocity signals for feedback can be obtained through integration of the accelerometer signals from the tip and midpoint accelerometers on the truss.

Previous research has been accomplished in the development of classical control laws for the UWCSL flexible truss. Vibration suppression through velocity feedback to the AJTs and RMAs, both independently and in a hybrid configuration, was first examined by Hallauer [7] at USAFA and modified for application to the UWCSL truss by Schulthess and Shepherd [19, 20]. This chapter examines the theoretical development, simulation, and experimental validation of classical analog velocity feedback for the UWCSL truss.

### *3.2 Approximate Integrator for Velocity Feedback*

The sensors on the UWCSL truss are servo accelerometers mounted at the truss tip and midpoint and on each of the RMA support structures. The accelerometers measure lateral acceleration of the truss at their respective positions and output continu-

ous voltage signals on the order of 38.8 volts/g [7]. This value was obtained through the use of resistors in the accelerometer circuits which are described in Appendix A. Velocity signals can be obtained by integrating the acceleration signals. Ideal or "exact" integration is difficult to implement in actual hardware because of small DC voltages which cannot be entirely removed from the circuitry. The bias from these DC voltages causes the integrator to drift and can create significant changes in the voltage output of the integrator. Bias in a feedback signal can be destabilizing to the system to which it is returned and is not a desirable result. Instead of relying on an "exact" integrator to obtain the velocity signal, an approximate integrator can be used. The second order approximate integrator developed for implementation in the control laws was obtained from the Martin Marietta Astronautics Group [7] and is defined by the differential equation.

$$\ddot{e}_{vi} + \Omega \dot{e}_{vi} + \Omega^2 e_{vi} = \frac{1}{RC} \dot{e}_{ai} \quad (3.1)$$

$e_{ai}$  is the adjusted acceleration signal.  $e_{vi}$  is the velocity signal.  $\Omega$  and  $RC$  are the user-specified frequency constant and integrator time constant respectively. Taking the Laplace transform of Equation 3.1 yields

$$s^2 E(s)_{vi} + s\Omega E(s)_{vi} + \Omega^2 E(s)_{vi} = s \frac{1}{RC} E(s)_{ai} \quad (3.2)$$

Manipulation of the terms in Equation 3.2 results in the transfer function of velocity signal to adjusted acceleration signal:

$$G(s) = \frac{E(s)_{vi}}{E(s)_{ai}} = \frac{s/RC}{s^2 + \Omega s + \Omega^2} \quad (3.3)$$

The DC gain of the approximate integrator is zero when  $s = j\omega = 0$ , and its frequency response is close to that of ideal integration for frequencies above 4 Hz as shown in Figure 3.1.

A state space representation of the approximate integrator is more convenient for implementation in actual hardware. The state space equations come from reducing Equation 3.1 into the following, first order differential equations:

$$\dot{e}_{vi} = -\Omega e_{vi} + \Omega e_2 + \frac{1}{RC} e_{ai}$$

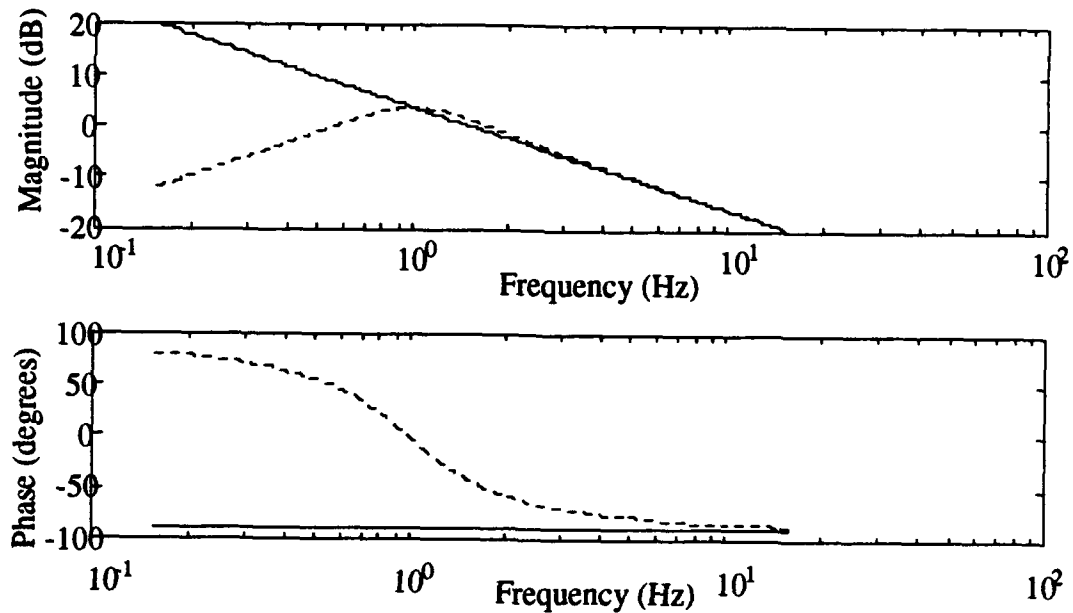


Figure 3.1: Frequency Response: Ideal Integrator (Solid), Approximate Integrator (Dashed)

$$\dot{e}_2 = -\Omega e_{vi} \quad (3.4)$$

The states are velocity ( $e_{vi}$ ) and  $e_2 = -\Omega \int e_{vi} dt + const.$  Equation 3.4 can be rewritten in the following matrix form:

$$\begin{bmatrix} \dot{e}_{vi} \\ \dot{e}_2 \end{bmatrix} = \begin{bmatrix} -\Omega & \Omega \\ -\Omega & 0 \end{bmatrix} \begin{bmatrix} e_{vi} \\ e_2 \end{bmatrix} + \begin{bmatrix} \frac{1}{RC} \\ 0 \end{bmatrix} [ e_{ai} ]$$

$$y = \begin{bmatrix} -1 & 0 \end{bmatrix} \begin{bmatrix} e_{vi} \\ e_2 \end{bmatrix} + \begin{bmatrix} 0 \end{bmatrix} [ e_{ai} ] \quad (3.5)$$

Figure 3.2 is the analog computer diagram of the approximate integrator state space equations in Equation 3.5. The GP-6 and EAI-20 analog computers were wired

to implement the approximate integrator circuit. The value of the user-specific constants  $\Omega$  and  $RC$  were chosen to be  $0.2\pi$  and 1 respectively [7]. The input to the analog circuit is the adjusted acceleration signal ( $e_{ai}$ ). For the truss configuration without RMAs, the adjusted acceleration signal is the difference between the accelerometer signal and a DC offset. For the truss configured with RMAs and two additional accelerometers, the adjusted acceleration signal is the difference between the two acceleration signals at each truss location. A detailed description of the adjusted acceleration signal for each controller is in Section 3.3 and Section 3.4. It is also important to note that the integrators and summers of an analog computer invert the incoming signals. Figure 3.2 shows a negative velocity signal as the output which is convenient for negative feedback purposes [20].

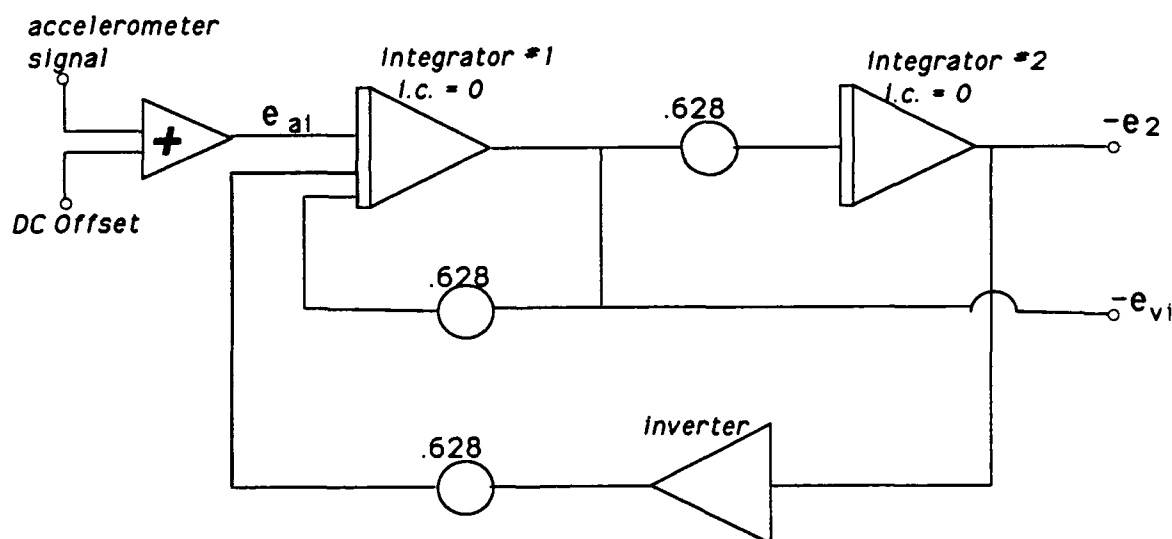


Figure 3.2: Approximate Integrator for Analog Computer Implementation

### 3.3 Classical Analog Control Using AJT Actuation

The first attempt at active damping of the UWCSL truss was negative velocity feedback to the tip and midpoint AJTs. The accelerometer mounted at the truss tip was used to obtain the acceleration signal. An approximate integrator, of the type discussed in Section 3.2, was implemented to obtain the velocity signal from the tip

acceleration signal. The adjusted acceleration signal ( $e_{ai}$ ) input to the approximate integrator analog circuit is the difference between the accelerometer output signal and the tip accelerometer DC offset. The DC offset value is a result of the accelerometer measuring the gravitational pull on the truss which is due to the slight tilt of the supporting table. The output of the analog computer was a negative tip velocity signal. The velocity signal was routed through the AJT control circuit and used to fire the tip AJTs to dampen the vibrations of the truss. This procedure was duplicated for the accelerometer and AJTs at the truss midpoint. The control law for AJT vibration suppression is a fourth order, two-input, two-output controller comprised of two uncoupled second order approximate integrators.

### 3.3.1 Non-Linear Simulation

SIMULINK was used to simulate the truss and the control law for AJT vibration suppression. A block diagram of the SIMULINK closed loop system for the AJT controller is in Appendix E. The eighth order finite element model developed in Section 2.4.4 was used in simulation because the RMAs were not connected to the truss hardware in the AJT controller configuration. The tip and midpoint signal approximate integrators were modeled by the transfer function from Equation 3.3. The AJTs were modeled as non-linear actuators which included a lead filter, a dead zone, a transistor, and a second order filter to incorporate the rise time delay between the control signal and the development of full force from the AJTs [19]. The rise time filter was expressed as the transfer function

$$G_{rr}(s) = \frac{F_{ss}\omega_n^2}{s^2 + 2\zeta\omega_n s + \omega_n^2} \quad (3.6)$$

where  $F_{ss}$  is the steady state force of 0.6 lbf,  $\zeta = 0.96$ , and  $\omega_n = 200 \text{ rad/sec}$ .

The simulation used a sinusoidal function, at the resonant natural frequencies of the first four modes of the truss, as the input signal to the tip AJTs to excite the truss model to its bending modes. The excitation signal was processed through a switch which controlled the length of time that the truss was excited before the controllers were activated. The excitation time was adjusted to closely match the magnitude of the acceleration signals of the simulation to the magnitude of the experimental acceleration signals. Figure 3.3 is a plot of the tip accelerations for the first four

Table 3.1: AJT Controller: Approximate Simulation Settling Times in Seconds

Mode	S. Time (O.L.)	S. Time (C.L.)	$\Delta$ Time
1	40	4	36
2	12	3	9
3	3	3	0
4	2	2	0

modes of the truss in a closed loop model implementing the AJT control law. The simulation results in Figure 3.3 predict the response of the truss to the AJT controller. The excitations between 5 and 6 seconds in the first mode simulation results were due to a firing of the tip AJTs in the simulation which caused the accelerations to increase slightly before damping passively to equilibrium. The tip AJT firing was due to a problem in the modeling of the non-linear dead-band of the AJT solenoid valves. This burst of acceleration should not be present in the experimental results. Comparison of the simulated open loop model, without RMAs, and the AJT controller model simulation plots (Figures 2.8 and 3.3) demonstrates the AJT controller's effectiveness in increasing the damping of the first two modes of the truss and its minimal effect on the third and fourth modes. Table 3.1 shows the approximate simulated settling times (S. Time) of the open loop model, without RMAs, and of the AJT controller. It also shows the difference of the open loop model and the AJT controller settling times ( $\Delta$  Time). The damping ratios were not calculated for simulation results.

Simulation results predicted the theoretical response of the truss to the AJT controller and the next logical step was implementation of the controller on actual hardware.

### 3.3.2 Experimental Results

The truss was excited to its first four bending modes using the fixed sine function of an HP Dynamic Signal Analyzer (DSA) as the control input to the tip AJTs. Acceleration at the truss tip and midpoint was recorded from the accelerometers at these two positions. Once a full range of motion was recorded by the accelerometers,

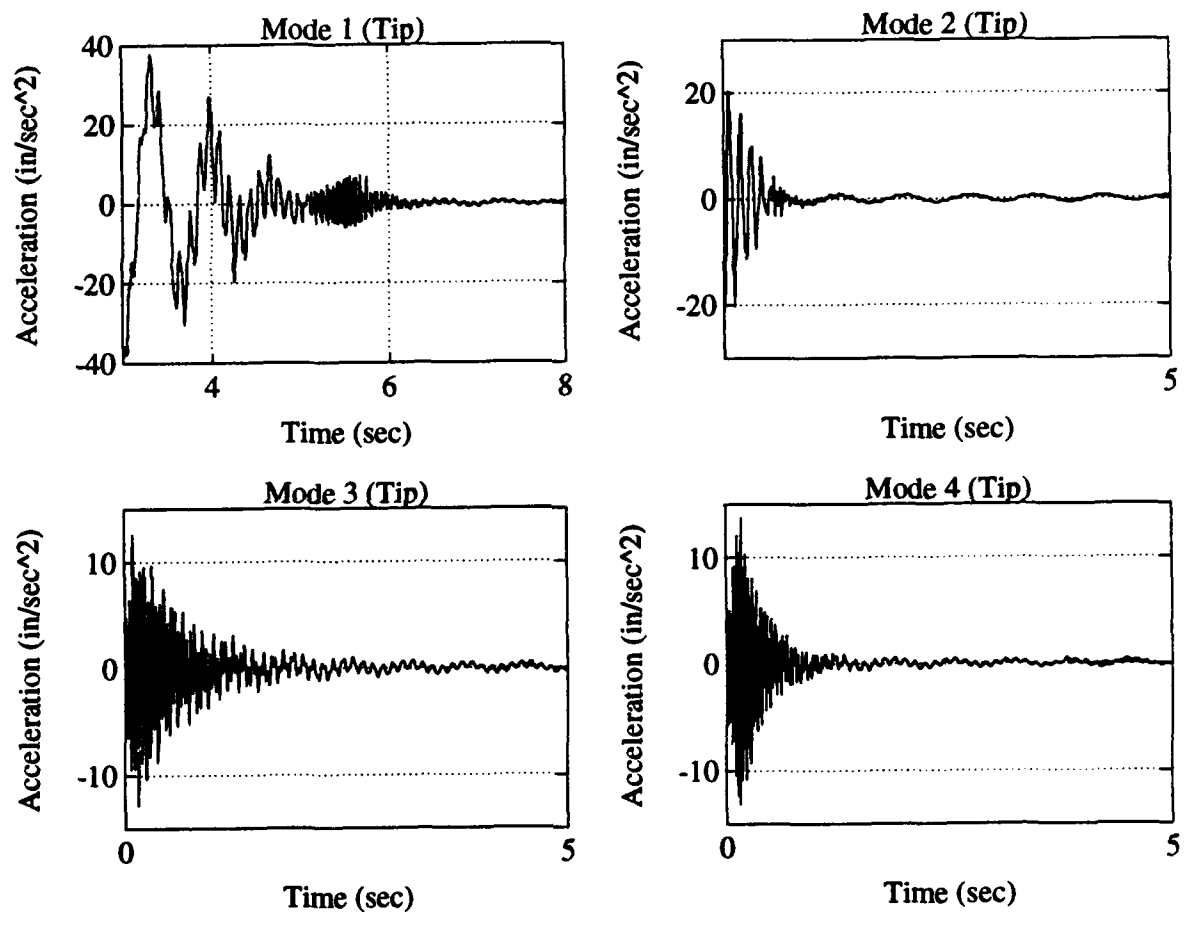


Figure 3.3: Simulation of AJT Controller

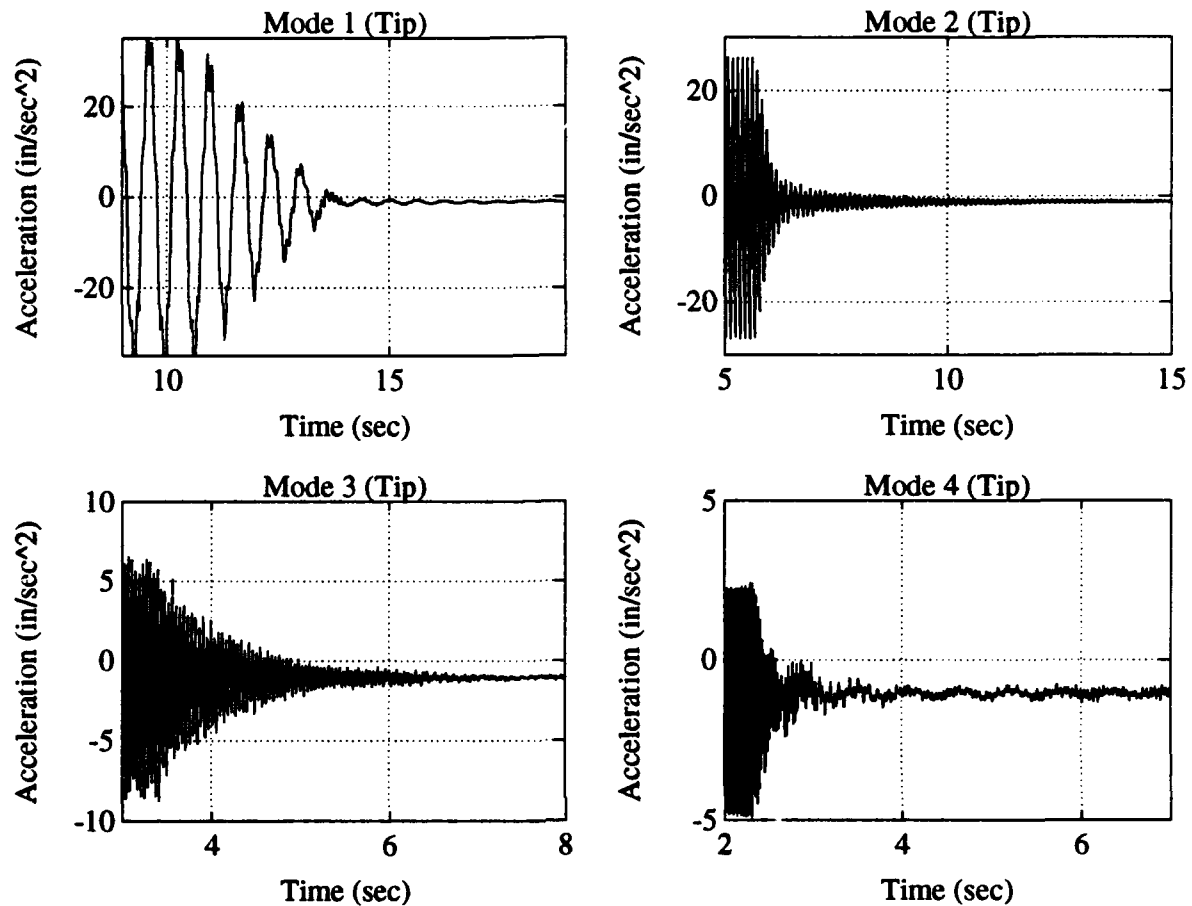


Figure 3.4: Experimental AJT Controller

the excitation signal was shut off and the control signal was activated. Figure 3.4 and Figure 3.5 are plots of the experimental tip and midpoint acceleration signals of the UWCSL truss with active damping through the AJT controller. As expected, the experimental results were similar to the non-linear simulation results. The first mode acceleration signals were cleaner than the simulated results, a result of the existence of non-linear friction which was neglected in simulation. The AJTs also functioned properly, with respect to their dead-bands, and did not create the disturbances seen in the simulation. The experimental settling times of each of the modes was approximately the same as the simulated settling time. The damping ratios of the experimental closed loop AJT controller ( $\zeta_{clAJT}$ ) were calculated using the logarithmic decrement method. The damping ratios and the settling time (S. Time) are listed in Table 3.2. Table 3.2 also includes the  $\log_{10}$  ratio of the damping coefficients

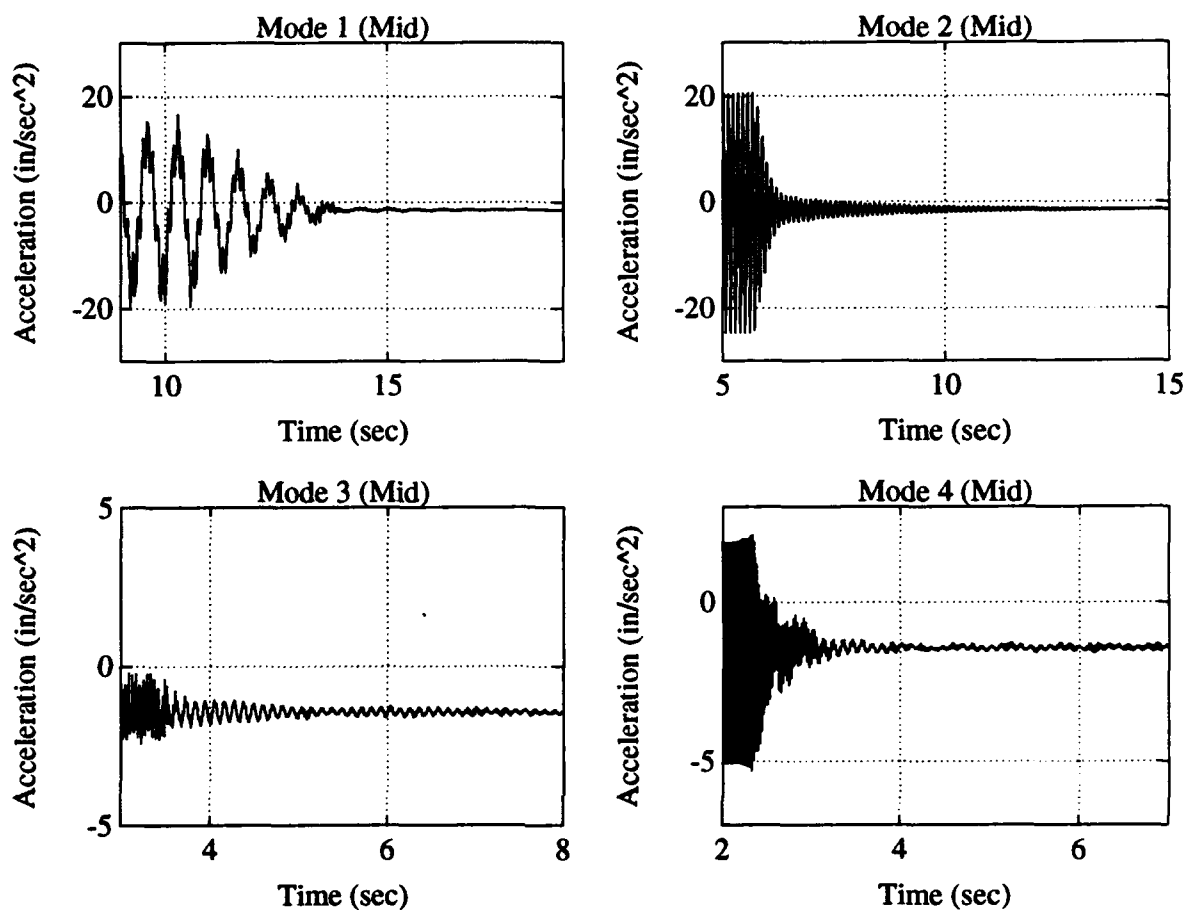


Figure 3.5: Experimental AJT Controller

of the closed loop truss with the AJT controller to the open loop truss, without RMAs ( $\zeta_{AJT}$ ), and the difference between the settling times of the open loop truss, without RMAs, and the closed loop truss ( $\Delta$  Time).

The first and second modes show a strong increase in the damping ratios while decreasing the respective settling times. It should be noted that the AJTs did not fire when the control law was initiated for the third and fourth bending modes of the UWCSL truss. The damping ratios and settling times for the third and fourth modes should therefore be the same as the open loop experimental results. The results are different due to error in determining the damping ratios using the logarithmic decrement method because of the multiple modes measured by the accelerometers at high frequencies. The experimental results for the third and fourth modes show a decrease in the damping ratios from the open loop case, while at the same time, the settling

Table 3.2: AJT Controller: Experimentally Determined Damping Ratios ( $\zeta_{clAJT}$ )

Mode	$\zeta_{AJT}$	S. Time (O.L.)	$\zeta_{clAJT}$	S. Time	$\log \left[ \frac{\zeta_{clAJT}}{\zeta_{AJT}} \right]$	$\Delta$ Time
1	0.01190	35.75	0.05383	6.44	0.65548	29.31
2	0.00863	12.84	0.02356	2.72	0.43616	10.12
3	0.01307	4.80	0.01002	2.63	-0.11538	2.17
4	0.01555	1.44	0.00646	0.70	-0.38140	0.74

times decrease.

The simulation and experimental results demonstrate the effectiveness of the AJTs in controlling the first and second mode disturbances of the truss. This is a favorable result because most of the displacement and motion is excited by the first two modes. The experimental results demonstrate that the AJTs do not drive any of the modes unstable. The AJTs do not misfire during the third and fourth modes as discussed by Shepherd [20]. The destabilizing AJT misfires reported by Shepherd were due to a saturation of the control circuit and its capacitors. The saturation was a result of the large amplitude (1 Vpk) of the fixed sine function of the HP Dynamic Signal Analyzer which was the control input to the tip AJTs. Reducing the level of the fixed sine input to 0.05 Vpk eliminated the saturation and the AJT misfirings. The failure of the AJTs to dampen the third and fourth mode vibrations indicates that velocity feedback to the AJTs alone is not an adequate solution to completely suppress all of the modal vibrations.

### 3.4 Classical Analog Control Using RMA Actuation

Another attempt at active damping of the UWCSL truss is negative velocity feedback to the tip and midpoint RMAs. The RMA control force is limited by its mass, location, and natural frequency. Two classical control methods of velocity feedback to the RMAs have previously been examined: pure proportional velocity feedback of the two truss velocity signals (tip and mid) and relative feedback with a gain on each velocity signal, to match signal magnitudes of the tip and RMA accelerometer

signals, with an RMA amplifier gain on the difference of the two modified signals at each location [20]

Straight velocity feedback, after integrating the tip and midpoint truss mounted accelerometer signals, resulted in a poor increase in the overall damping of the truss. The root locus of the eigenvalues of the closed loop system showed little or no stability improvement for gains within the range of the RMA amplifier (1 to 10) [20]. Stability was only improved for the second mode of vibration which was expected due to the addition of mass at the tip and midpoint. This was demonstrated through the passive damping in the open loop simulation and experimental results in Chapter 2. The only positive aspect of straight proportional feedback was the use of just two accelerometers.

Relative velocity feedback between the truss and RMA mounted accelerometer signals was the second method of classical control applied to the RMAs [7]. Different procedures were utilized to obtain the simulation and experimental results. The experimental magnitude of the acceleration signals from each of the accelerometers was different, while the truss was at equilibrium, due to voltage offset in the hardware. In order to allow each acceleration to be equally weighted in the feedback loop, the magnitudes of the signals were forced to be equal through the application of gains. The tip RMA and truss mounted accelerometers' output signals were 0.12 and 0.54 volts respectively. The truss mounted accelerometer signal was amplified by a gain ( $K_{tt}$ ) of 0.57 and the difference of the two signals became the adjusted acceleration signal ( $e_{ai}$ ) input to the tip approximate integrator analog circuit. The midpoint RMA and truss mounted accelerometers' output signals were 0.12 and 0.14 volts respectively. The truss mounted accelerometer signal was amplified by a gain ( $K_{mt}$ ) of 1.2 and the difference of the two signals became the adjusted acceleration signal ( $e_{ai}$ ) input to the midpoint approximate integrator analog circuit. This was not a problem in the simulation model because identical sensors were used and the acceleration signals were of equal magnitude. The relative velocities ( $\dot{q}_{5-1}$  and  $\dot{q}_{6-3}$ ) out of the approximate integrators were applied in proportional feedback through the RMA amplifiers. The proportional feedback control laws are:

$$f_{5-1(tip)} = -k_t \dot{q}_{5-1}$$

Table 3.3: RMA Feedback Gains on Truss Velocities

Signal	Feedback Gain	Value
$\ddot{q}_{truss\ tip}$	$k_{tt}$	0.57
$\ddot{q}_{truss\ mid}$	$k_{tt}$	1.20
$\dot{q}_{tip}$	$k_t$	6.00
$\dot{q}_{mid}$	$k_m$	1.90

$$f_{6-3(mid)} = -k_m \dot{q}_{6-3} \quad (3.7)$$

where  $k_t$  and  $k_m$  are the gains applied through the RMA amplifier to the respective velocities. The RMA amplifier gains were limited to values below 7 because higher gains resulted in actuator instability. When high amplifier gains were applied to the RMA velocity feedback signals, the acceleration signals from the RMA mounted accelerometers recorded violent oscillations while the truss accelerometer signals tended to zero [16, 20]. The values of the relative RMA velocity feedback gains and the signals to which they are applied are in Table 3.3.

The control law for RMA vibration suppression is therefore a fourth order, four-input, two-output controller comprised of two uncoupled second order approximate integrators with two constant gains in simulation and four constant gains in experimentation.

#### 3.4.1 Non-Linear Simulation

SIMULINK was used to simulate the truss and the control law for RMA vibration suppression. A block diagram of the SIMULINK closed loop system for RMA controller is in Appendix E. The twelfth order finite element model developed in Section 2.4.5 was used in this simulation. The tip and midpoint approximate integrators were modeled by the transfer function from Equation 3.3. The RMA models were developed in Section 2.3.

Just as in the AJT controller simulation, a sinusoidal function, at the resonant natural frequencies of the first four modes of the truss, was the input signal to the tip AJTs to excite the truss model to its bending modes. The truss modes were excited

Table 3.4: RMA Controller: Approximate Simulation Settling Times in Seconds

Mode	S. Time (O.L.)	S. Time (C.L.)	$\Delta$ Time
1	40	20	20
2	12	2	10
3	3	1.5	1.5
4	2	1	1

until the magnitude of the simulated acceleration signal matched the magnitude of the experimental acceleration signals. Figure 3.6 is a plot of the simulated tip accelerations for the first four modes of the truss in a closed loop model implementing the RMA relative velocity control law. The simulation results in Figure 3.6 predict the response of the truss to the RMA controller.

Comparison of the simulated open loop model, without RMAs, and the closed loop RMA controller model simulation plots (Figures 2.8 and 3.6) demonstrates the effectiveness of the RMA in increasing the damping of the second, third and fourth modes of the truss. Table 3.4 shows the approximate simulated settling times (S. Time) of the open loop model, without RMAs, and of the RMA controller. It also shows the difference of the open loop model and the RMA controller simulated settling times ( $\Delta$  Time). The damping ratios were not calculated for simulation results. The results show that the RMA controller had little effect, beyond passive damping due to the added mass of the RMAs, on the first mode. Once the simulation was accomplished, the experimental implementation was evaluated.

### 3.4.2 Experimental Results

The truss was excited to its first four bending modes using the fixed sine function of an HP Dynamic Signal Analyzer (DSA) as the control input to the tip AJTs. Acceleration at the truss tip and midpoint was recorded from the accelerometers at their respective positions. Once a full range of motion was recorded by the accelerometers, the excitation signal was shut off and the control signal was activated. Figure 3.7 and Figure 3.8 are plots of the experimental tip and midpoint acceleration signals of the

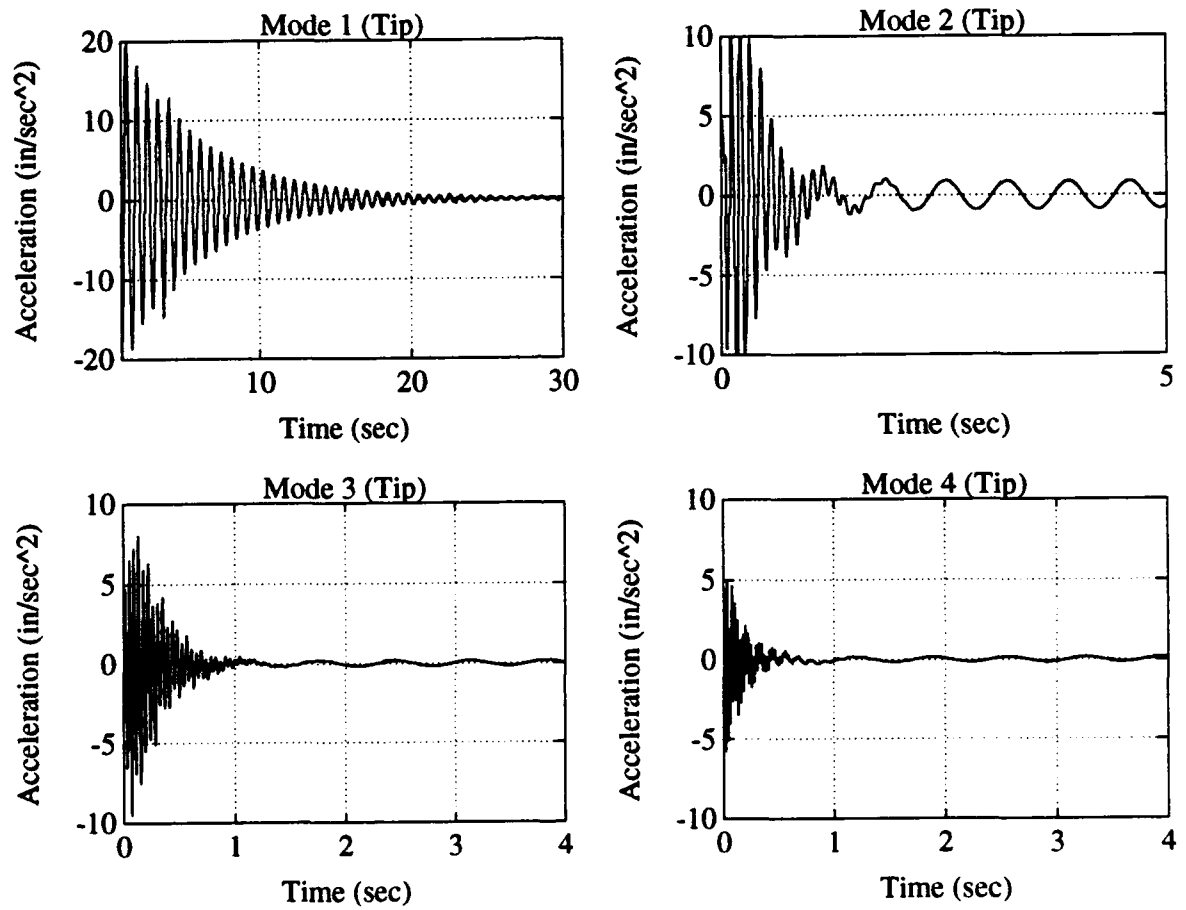


Figure 3.6: Simulation of RMA Controller

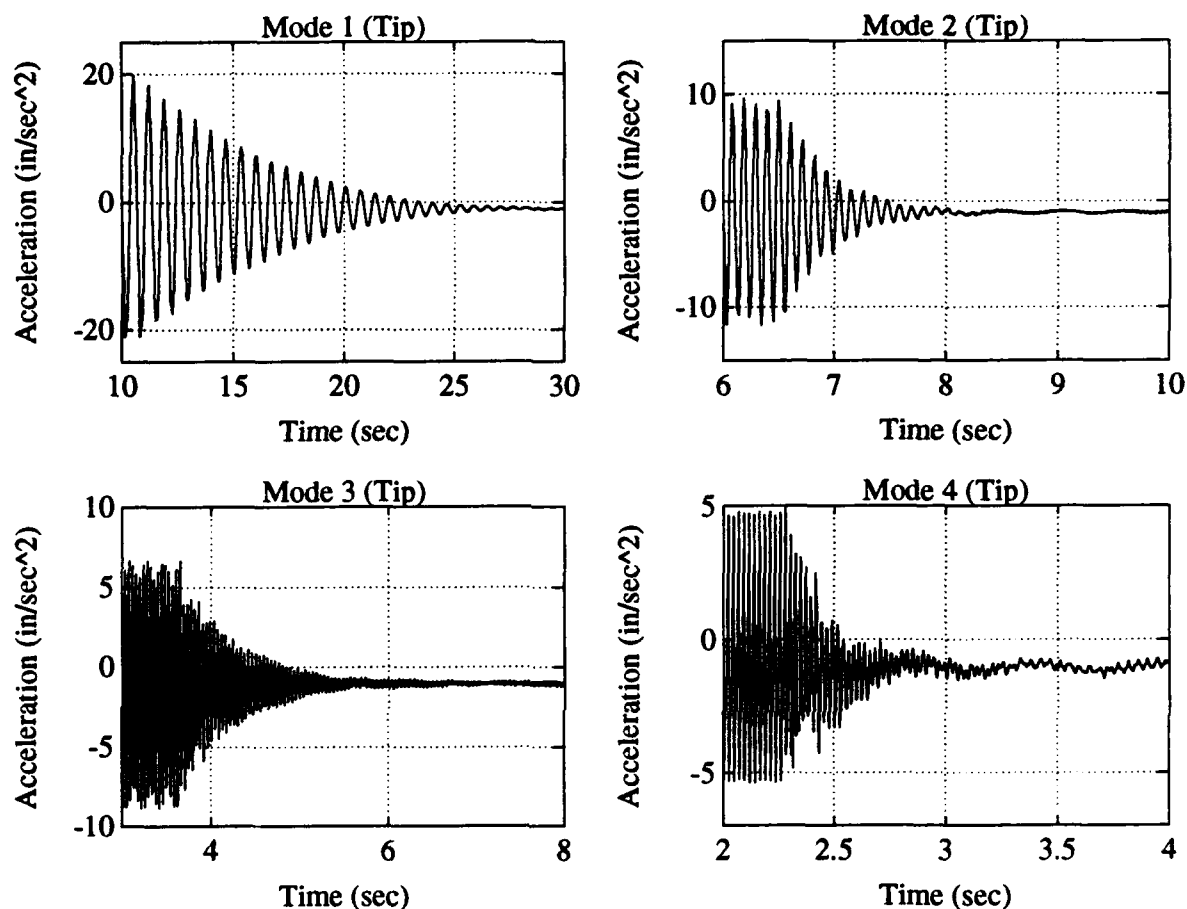


Figure 3.7: Experimental RMA Controller

UWCSL truss with active damping through the RMA controller. The experimental results were similar to the non-linear simulation predicted results in that the settling time of the tip accelerations of both were approximately equal. Table 3.5 shows the experimental tip acceleration settling times (S. Time) as well as the damping ratios of the experimental closed loop RMA controller ( $\zeta_{clRMA}$ ). The damping ratios were calculated using the logarithmic decrement method and the tabulated results are the average of the tip and midpoint values. Table 3.5 also includes the  $\log_{10}$  ratio of the damping coefficients of the closed loop truss with the RMA controller to the damping coefficients of the open loop truss, without RMAs and the difference between the settling times of the two configurations ( $\Delta$  Time). The RMA controller had a small, but

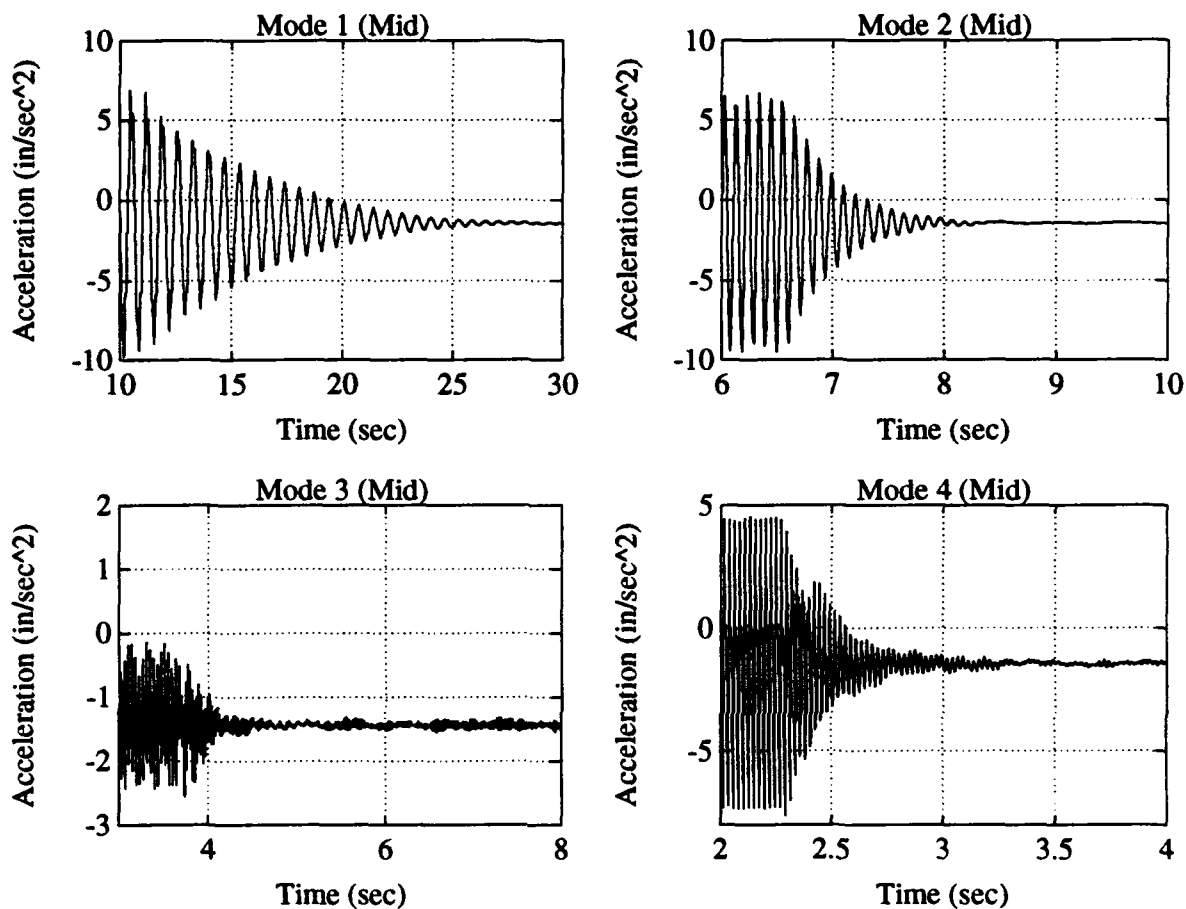


Figure 3.8: Experimental RMA Controller

favorable effect on the damping of the first mode due to the additional mass at the tip and midpoint of the truss. The second mode was dramatically improved in both its settling time and damping ratio. The third and fourth mode settling times were also decreased. The damping ratios of the third and fourth modes still decreased, but less than the decrease observed with the AJT controller.

The experimental results demonstrate the effectiveness of the RMAs in controlling the second and third modes of the truss. The RMA controller did not perform as well on the first mode as the AJT controller. The RMA controller performed slightly better than the AJT controller in improving the damping ratio and settling time of the second mode. The RMA controller's performance was noticeably better than the

Table 3.5: RMA Controller: Experimentally Determined Damping Ratios ( $\zeta_{clRMA}$ )

Mode	$\zeta_{AJT}$	S. Time (O.L.)	$\zeta_{clRMA}$	S. Time (C.L.)	$\log \left[ \frac{\zeta_{clRMA}}{\zeta_{AJT}} \right]$	$\Delta$ Time
1	0.01190	35.75	0.02323	16.97	0.29059	18.78
2	0.00863	12.84	0.02584	2.92	0.47796	9.92
3	0.01307	4.80	0.01169	2.60	-0.04859	2.80
4	0.01555	1.44	0.01177	0.63	-0.12096	0.81

AJT controller in improving the third and fourth mode's damping ratios although it is still greater than the open loop damping ratio. The settling time improvement of the RMA controller over the AJT controller was minimal. The damping ratios of the third and fourth mode are still less than the open loop damping ratios which could be due to experimental error in determining the damping ratios using the log decrement method because of the multiple modes measured by the accelerometers at the higher frequencies.

### 3.5 Classical Analog Control Using Hybrid Actuation

In Section 3.3, a velocity feedback controller for the AJTs was developed and implemented. The AJT controller was effective in increasing the damping of the low frequency, high displacement modes of the truss. It was however, ineffective in controlling the high frequency vibrations. In Section 3.4, a relative velocity controller for the RMAs was developed and implemented. The RMA controller was effective only in controlling the higher frequency vibrational modes of the truss. By using both of the independently designed controllers together, functioning simultaneously, it is expected that a more effective controller will be achieved. Hybrid actuation is the term coined by the USAFA team to describe "the simultaneous functioning of two or more types of structure-borne actuators in active vibration control each having a frequency band of greatest effectiveness which is different from the bands of the other types." [7] In this case, the hybrid controller is the combination of the AJT and RMA controllers where no design effort is made to couple the two controllers. The second

mode vibrations of the truss are damped by both the AJT and RMA controllers when functioning independently and therefore, the hybrid controller is predicted to have its best results on the second mode.

The control law for hybrid vibration suppression is therefore an eighth order, four-input, four-output controller comprised of four uncoupled second order approximate integrators with two constant gains in simulation and four constant gains in experimentation.

### *3.5.1 Non-Linear Simulation*

SIMULINK was used to simulate the truss and the hybrid AJT and RMA controller. A block diagram of the SIMULINK closed loop system for the hybrid controller is in Appendix E. The twelfth order finite element model developed in Section 2.4.5 was used in this simulation. The hybrid controller in simulation is simply the combination of the AJT and RMA simulated controllers from Sections 3.3 and 3.4.

Again, a sinusoidal function, at the resonant natural frequencies of the first four modes of the truss, was the input signal to the tip AJTs to excite the truss model to its bending modes. The truss modes were excited until the magnitude of the simulated acceleration signal matched the magnitude of the experimental acceleration signals. Figure 3.9 is a plot of the simulated tip accelerations for the first four modes of the truss in a closed loop model implementing the hybrid control law. The simulation results in Figure 3.9 predict the response of the truss to the hybrid controller. The excitations between 4 and 6 seconds in the first mode simulation were caused by the AJT model firing, as was explained in Section 3.3. The RMAs acted on the high frequency vibrations and reduced them quickly to equilibrium. This burst of acceleration should not be present in the experimental results; however, the influence of the RMAs may be noticeable. The improved effectiveness of the hybrid controller in increasing the damping of all of the modes of the truss was demonstrated through comparison of the simulated open loop model, without RMAs, and the closed loop hybrid controller model simulation plots (Figures 2.8 and 3.9). Table 3.6 shows approximate simulated settling times (S. Time) of the open loop model, without RMAs, and of the hybrid controller. The difference of the open loop model and the hybrid controller simulated settling times ( $\Delta$  Time) is also reported in Table 3.6. The

Table 3.6: Hybrid Controller: Approximate Simulation Settling Times in Seconds

Mode	S. Time (O.L.)	S. Time (C.L.)	$\Delta$ Time
1	40	4	36
2	12	2	10
3	3	2	1
4	2	1	1

damping ratios were not calculated for simulation results. The results show that the hybrid controller does in fact combine the effective damping of the AJT and RMA individual controllers as predicted. The next step was experimental implementation which should confirm the simulation results.

### 3.5.2 Experimental Results

The truss was excited to its first four bending modes using the fixed sine function of an HP Dynamic Signal Analyzer (DSA) as the control input to the tip AJTs. Acceleration at the truss tip and midpoint was recorded from the accelerometers at their respective positions. Once a full range of motion was recorded by the accelerometers, the excitation signal was shut off and the hybrid control signal was activated. Figure 3.10 and Figure 3.11 are plots of the experimental tip and midpoint acceleration signals of the UWCSL truss with active damping through the hybrid controller. The experimental results were similar to the non-linear simulation predicted results in that the settling time of the tip accelerations of both were approximately equal. The experimental results did not create the large disturbances seen in the first mode of the simulation due to AJT firings. However, a disturbance did occur, at approximately 12 seconds on the experimental tip acceleration plot, due to RMA control forces acting on the truss. Table 3.7 shows the experimental tip acceleration settling times (S. Time) as well as the damping ratios of the experimental closed loop RMA controller ( $\zeta_{clRMA}$ ). The damping ratios were calculated using the logarithmic decrement method and the tabulated results are the average of the tip and midpoint values. Table 3.5 also includes the  $\log_{10}$  ratio of the damping coefficients of the closed loop truss

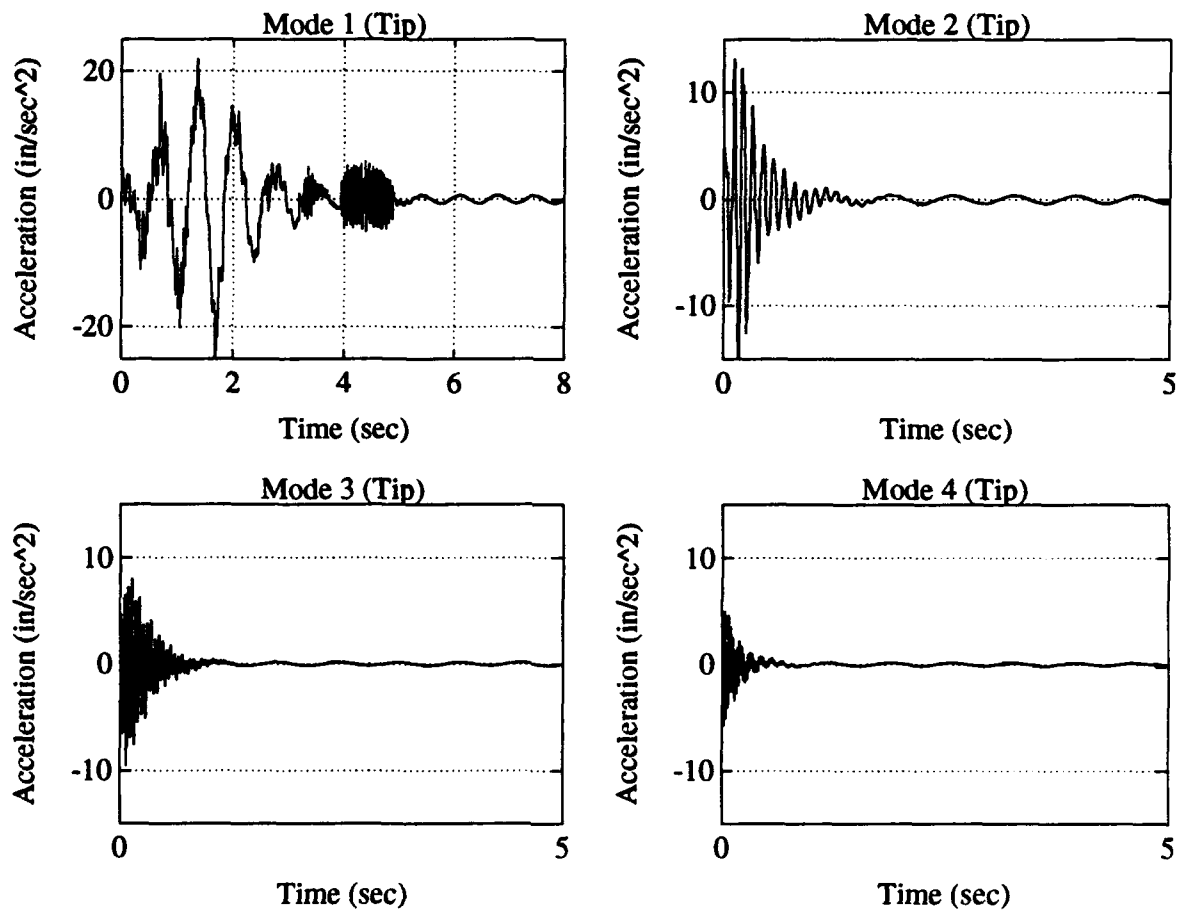


Figure 3.9: Simulation of Hybrid AJT and RMA Controller

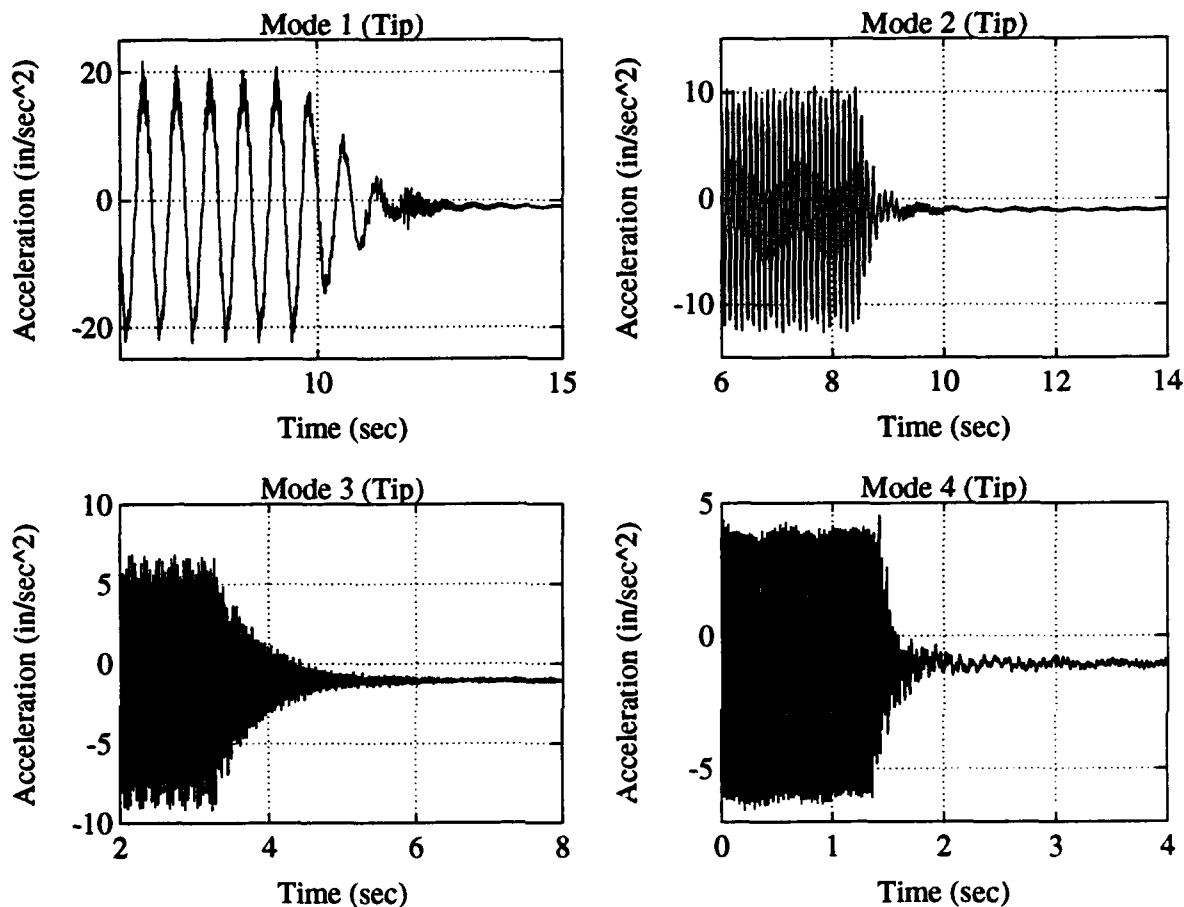


Figure 3.10: Experimental Hybrid AJT and RMA Controller

with the RMA controller to the damping coefficients of the open loop truss, without RMAs, and the difference between the settling times of the two configurations ( $\Delta$  Time). The hybrid controller performed as expected, combining the low frequency damping from the AJTs and the high frequency RMA damping. The damping ratios of all of the modes was increased, especially the damping ratios of the first two modes. The settling times of all of the modes was also decreased dramatically.

The experimental results demonstrate the effectiveness of the hybrid controller for vibration suppression of the first four bending modes of the truss. The hybrid controller out performed the individual AJT and RMA controllers as was expected.

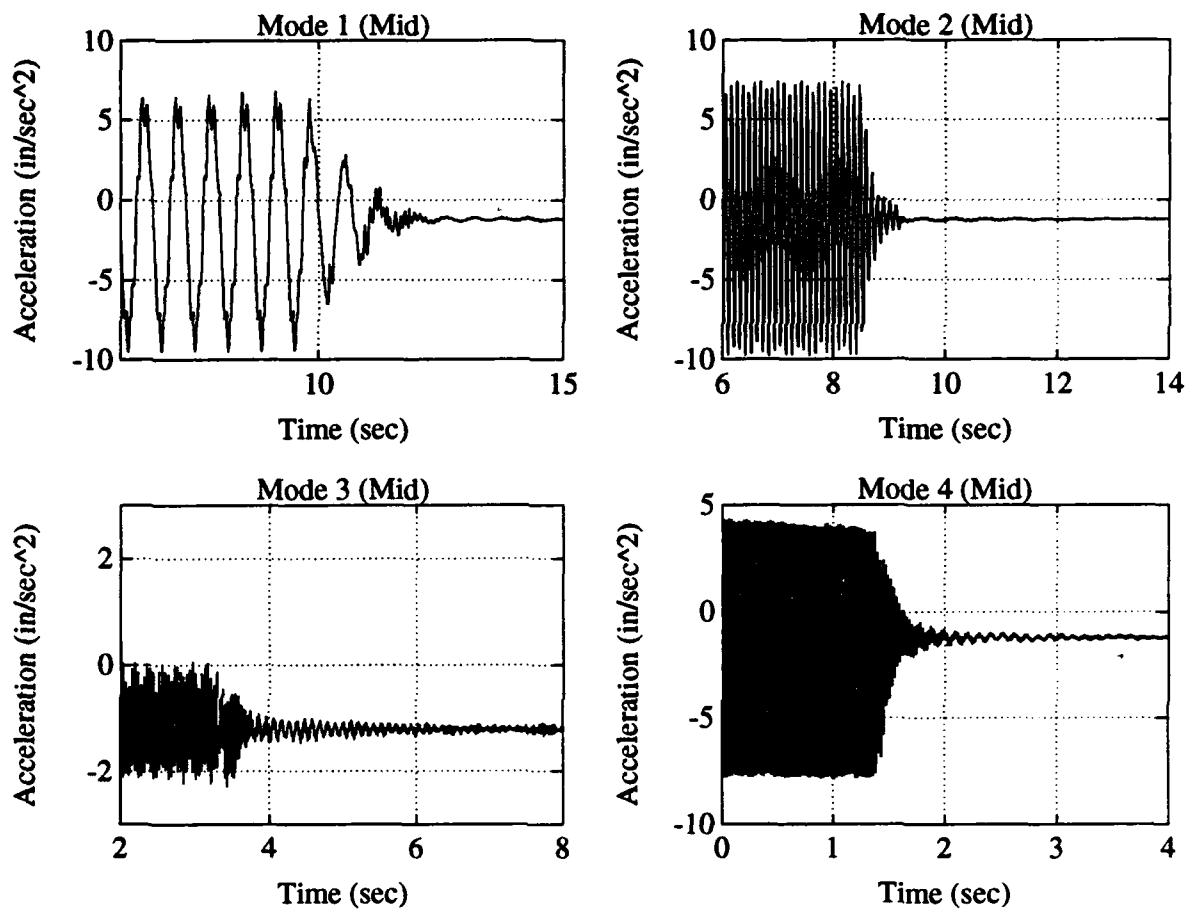


Figure 3.11: Experimental Hybrid AJT and RMA Controller

Table 3.7: Hybrid Controller: Experimentally Determined Damping Ratios ( $\zeta_{clHYB}$ )

Mode	$\zeta_{AJT}$	S. Time (O.L.)	$\zeta_{clHYB}$	S. Time (C.L.)	$\log \left[ \frac{\zeta_{clHYB}}{\zeta_{AJT}} \right]$	$\Delta$ Time
1	0.01190	35.75	0.08955	4.25	0.87856	31.50
2	0.00863	12.84	0.04466	0.94	0.71391	11.60
3	0.01307	4.80	0.01498	2.04	0.05918	2.76
4	0.01555	1.44	0.01654	0.63	0.02680	0.81

## Chapter 4

# DIGITAL CONTROL: DISCRETIZATION AND DIGITIZATION OF CLASSICAL ANALOG CONTROL LAW

### 4.1 Overview

Three classical control laws, using classical design methods, were implemented with analog computers for vibration suppression of the first four bending modes of the UWCSL truss. Continuous velocity feedback to the AJTs and RMAs, both independently and in a hybrid configuration, demonstrated the effectiveness of active damping to control vibrations. Digital implementation is desired to facilitate modifications to gains and for ease in applying new control laws to the existing system. Direct digital control design is the preferred method of developing discrete control laws for a system; however, initial design and validation of the digital control law was based on the continuous controller already established and proven for the UWCSL truss. The initial digital controller for the truss is therefore an "emulation" of the continuous designs [4]. Emulation, the discretization process, will produce discrete equivalents for each of the control laws discussed in Chapter 3. In this chapter, we examine the theoretical development of the discretization process and simulation of the digital control laws on the truss models. Also reported here is the experimental validation of the simulated digital AJT and RMA controllers and a comparison of the performance of the two continuous and digital controllers.

### 4.2 Digital Control

The continuous controllers designed and implemented in Chapter 3 respond to the complete time history of the input signal and the return signal in the feedback loop. In digital control, the input signal is defined, or variable, only at distinct instants of time. A sampler converts the continuous-time signal to a discrete-time signal based

on a specified sampling period ( $T$ ). The sampling period is assumed to be fixed for the digital design in this thesis although future work may be done to examine multiple or variable sampling rates in digital control of the UWCSL truss. The sampler is commonly referred to as an analog to digital (A/D) converter or filter. The sampling period ( $T$ ) can be determined in two ways. The first method is to provide a clock which supplies a pulse or interrupt every  $T$  seconds. The A/D converter sends a value to the computer each time an interrupt arrives. The second method is to access the A/D converter upon completion of each cycle during the execution of code and then to send a new value to the computer. This free running method therefore has its sampling period ( $T$ ) fixed by the computational code. The A/D converter outputs a discrete and "quantized" signal at the specified sampling period [4]. The quantization size ( $q$ ) of the sampled output of the A/D converter is the fixed number of places of accuracy of the digits, usually in binary. A digital signal is a signal which is discrete and quantized [4].

The digital controller must take into account the sampling period ( $T$ ) and the quantization size ( $q$ ) of the digital signal which it receives as input. If  $T$  and  $q$  are small (a sampling frequency of 50 or more times the system bandwidth and a 16-bit word size) the digital signal is considered to be nearly continuous. With small values of  $T$  and  $q$ , the continuous controller design can be digitized using the emulation method. The goal of emulation is to find the best digital controller to match the desired continuous controller. There is no exact solution to this problem because a complete time history of the controller input signal is not available in the discrete realm. Emulation of the continuous controllers from Chapter 3 is discussed in Section 4.3.

The output of the digital controller is a digital signal which must be converted to a continuous-time signal before being applied to the circuits and amplifiers of the truss hardware. A zero-order hold (ZOH) is the most common type of digital to analog (D/A) converter which accepts the digital sample of the output signal and holds its value constant until the next sample is sent. A piecewise constant output of the D/A is a signal which can be applied to the hardware of a system.

A block diagram of a basic continuous-time and a digital control system is shown in Figure 4.1. The variables with  $(t)$  represent continuous signals and variables with  $(kT)$  depict digital signals. The following are the variables and their representations

in the block diagram:  $r(t)$  is the reference input,  $u(t)$  is the control signal,  $y(t)$  is the plant output,  $e(t)$  is the error signal which is the difference between the reference input and the returned plant output,  $e(KT)$  is the discrete error signal,  $u(KT)$  is the discrete control signal. The clock is shown because it synchronizes the digital controller, but it is not an explicit part of the signal flow in the control loop.

The most important impact of implementing a digital control system is the time delay associated with the computational time of the system and the D/A converter. This delay depends primarily on the speed of the digital computer, the digital signal processing boards, and the software. Another important factor is the complexity of the digital controller and the number of computational cycles required to obtain the output signal for feedback.

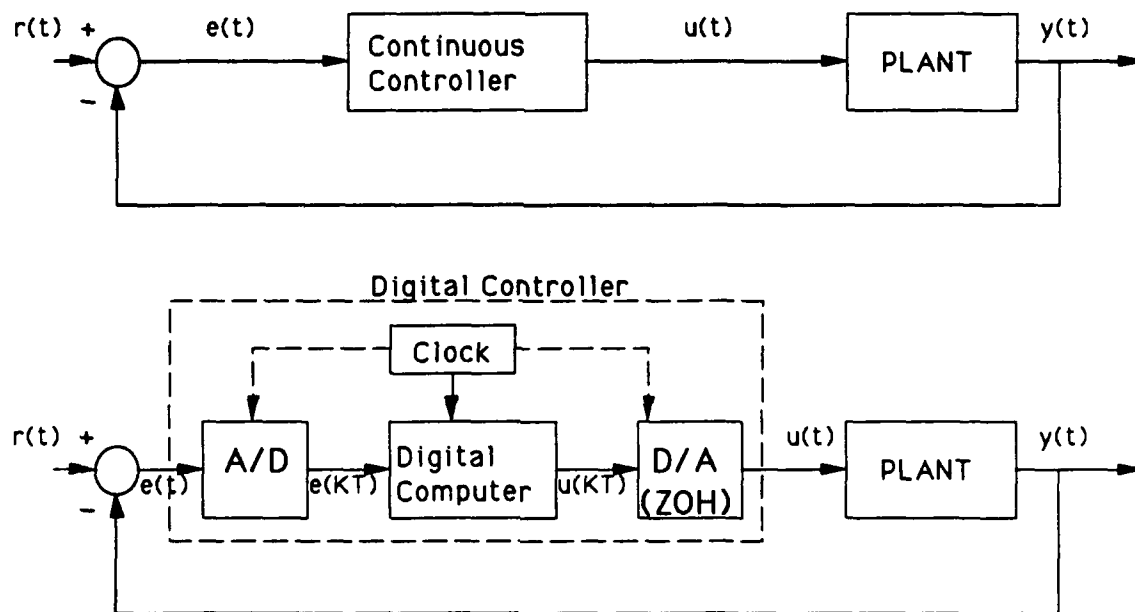


Figure 4.1: Block Diagram of a Continuous and Digital Control System

### 4.3 Emulation by Tustin's Method

Emulation is the process of transforming the differential equation which represents the continuous controller into a difference equation with a solution that approximates the solution of the original differential equation. The derivation of three rules, "based on the selection of the approximation of the incremental area term" of the difference equations, is described in Franklin [4]. Each of the rules makes different assumptions about what happens to the signal and the area under the signal between sample points. The three numerical integration rules are forward, backward, and trapezoid rules. The trapezoid rule provides for more accuracy in discrete integration and results in the following approximation for the frequency variable ( $s$ ) of a Laplace transform:

$$s \approx \frac{2z-1}{Tz+1} \quad (4.1)$$

$T$  is the sampling period and  $z$  has the same role in the discrete system  $z$ -transform that  $s$  has in the Laplace transform.

Tustin's method, or the bilinear transformation, is the substitution of the trapezoid rule approximation for the frequency variable of a Laplace transform (Equation 4.1). Although Tustin's method was used in this thesis, it should be noted that all of the methods of emulation, except the forward rule, guarantee a stable discrete system if the original continuous model is stable. Tustin's method can be summarized by the following rule: "Given a continuous transfer function,  $H(s)$ , a discrete equivalent can be found by the substitution [4]:

$$H_T(z) = H(s)|_{s=(2/T)[(z-1)/(z+1)]} \quad (4.2)$$

The continuous control laws designed and implemented in Chapter 3 utilize approximate integrators to obtain velocity signals from each acceleration signal. Section 3.2 describes the development of the state space equations of the continuous approximate integrators (Equation 3.5) which have the following matrix form:

$$\begin{aligned} \dot{\mathbf{x}}(t) &= \mathbf{A}\mathbf{x}(t) + \mathbf{B}e(t) \\ u(t) &= \mathbf{C}\mathbf{x} + \mathbf{D}e(t) \end{aligned} \quad (4.3)$$

where  $e(t)$  is the continuous acceleration signal from the accelerometers and  $u(t)$  is the continuous velocity signal output. The Laplace transform of Equation 4.3 is:

$$\begin{aligned} s\mathbf{X} &= A\mathbf{X} + BE \\ U &= C\mathbf{X} + DE \end{aligned} \quad (4.4)$$

Applying Tustin's method, substituting the approximation for "s" (Equation 4.1) into Equation 4.4, results in the z-transform equivalent [4]:

$$\begin{aligned} \frac{2(z-1)}{T(z+1)}\mathbf{X} &= A\mathbf{X} + BE \\ \text{or} \\ (z-1)\mathbf{X} &= \frac{AT}{2}(z+1)\mathbf{X} + \frac{BT}{2}(z+1)E \\ U &= C\mathbf{X} + DE \end{aligned} \quad (4.5)$$

The time domain equation for the state of the z-transform equivalent is

$$\mathbf{x}(k+1) - \mathbf{x}(k) = \frac{AT}{2}(\mathbf{x}(k+1) + \mathbf{x}(k)) + \frac{BT}{2}(e(k+1) + e(k)). \quad (4.6)$$

Collecting all of the  $k+1$  terms on the left side of the equation leads to the discrete state term  $\mathbf{w}(k+1)$  as seen below [4]:

$$\begin{aligned} \mathbf{x}(k+1) - \frac{AT}{2}\mathbf{x}(k+1) - \frac{BT}{2}e(k+1) &= \mathbf{x}(k) + \frac{AT}{2}\mathbf{x}(k) + \frac{BT}{2}e(k+1) \\ &= \sqrt{T}\mathbf{w}(k+1) \end{aligned} \quad (4.7)$$

From Equations 4.6 and 4.7, a mathematical derivation can be accomplished to describe the discrete equivalent of the continuous system, at a specified sampling period (T), in the following matrix form [4]:

$$\begin{aligned} \dot{\mathbf{w}}(k+1) &= \Phi\mathbf{w}(k) + \Gamma\epsilon(k) \\ u(k) &= H\mathbf{w}(k) + J\epsilon(k). \end{aligned} \quad (4.8)$$

Table 4.1: Tustin Method: Discrete State Space Matrices

$\Phi$	$(I + \frac{AT}{2})(I - \frac{AT}{2})^{-1}$
$\Gamma$	$(I - \frac{AT}{2})^{-1}B\sqrt{T}$
$H$	$\sqrt{TC}(I - \frac{AT}{2})^{-1}$
$J$	$D + C(I - \frac{AT}{2})^{-1}BT/2$

$\Phi$ ,  $\Gamma$ ,  $H$  and  $J$  in Equation 4.8 are defined in Table 4.1.

The emulation process is dependent on the desired sampling period ( $T$ ) of the discrete model. Emulation via Tustin's method was accomplished using MATLAB [14], a high-performance software package for numeric analysis, matrix computation, and signal processing. Multiple digital controller models were designed by adjusting the sampling period of the design and performing iterations in MATLAB. Three of the discrete controller (approximate integrator) models are in Appendix F. The digital model chosen for use in simulation and experimental implementation was dependent on the sampling period attainable in the actual computer hardware. The hardware and software used in the digital control of the UWCSL truss are discussed in Section 4.4.

#### 4.4 LABVIEW: Digital Data Acquisition and Control

The digital controllers for UWCSL were processed by a digital computer using National Instruments' LABVIEW 2 [11] software package which is designed for data acquisition and control, data analysis, and data presentation. LABVIEW is an acronym for Laboratory Virtual Instrument Engineering Workbench. LABVIEW is a programming language which replaces text-based code with intuitive graphic objects called virtual instruments (VIs). For the digital controller application reported in this thesis, the LABVIEW code was implemented on a Macintosh Quadra 900 equipped with a National Instruments NB-MIO-16 Input/Output board. The NB-MIO-16 board is a high-performance multifunction analog, digital, and timing input/output board.

Programming in LABVIEW involves building virtual instruments from the nu-

merous functional blocks in palette-type menus and connecting blocks with wires to enable data to pass from one block to the next. Front panels serve as the interactive interface for supplying inputs to the system, observing the outputs, and controlling the flow of data. All of the virtual instruments and block diagrams are combined in a modular hierarchy to produce the desired complex programs. The LABVIEW hierarchy, front panels, and block diagrams for both the digital AJT and the digital RMA controllers are in Appendix F. Each of these digital controllers is discussed in more detail in Sections 4.5 and 4.6 respectively.

Signals are processed through the digital computer in the following sequence. Acceleration signals from the truss enter the NB-MIO-16 I/O board through connections to the truss control panel. The I/O board utilizes a 12-bit A/D converter to create discrete binary representations of the analog signals. The LABVIEW virtual instrument program samples the binary data and converts it from binary to decimal representation. The decimal values of the discrete acceleration signals are then computationally manipulated to obtain the adjusted acceleration signals ( $e_{ai}$ ) which are the inputs to the digital approximate integrators. The output of the digital approximate integrators is discrete, negative velocity for feedback to the actuators. These discrete velocity signals are then scaled to binary values. The binary digital signals are then passed back through two multiplying 12-bit D/A converters which are located on the I/O board. The resulting piecewise continuous signals are the return signals for feedback to the control circuits or amplifiers of the actuators.

Two separate LABVIEW programs were developed for implementation of digital controllers to the UWCSL truss, one for the digital AJT controller and another for the digital RMA controller. Each of the programs is a combination of front panels and block diagrams utilizing LABVIEW virtual instruments (VIs) instead of text-based code. Each of the VIs represents a function which can be "wired" to other functions in the block diagram to allow the flow of data from one block to another [11]. The first function of the LABVIEW program established the input and output capabilities of the program and identified their locations. The I/O board has a sampling period of 50 to 100 kilo-Hertz for both the input A/D converter and output D/A converter. The binary digital acceleration signals from the I/O board were then read into the block diagram where they were scaled from binary format to decimal values. The decimal signals were manipulated to obtain the adjusted acceleration signals which

were the inputs to the digital approximate integrators. The digital approximate integrators are state space equation representations of difference equations derived using Tustin's emulation method. The difference equations require the past values of the states, velocity and displacement, in order to determine the digital, negative velocity signals used for feedback to the actuators of the truss. The past values of the states were obtained using "shift registers" which transfer values from the current execution cycle of the block diagram to the beginning of the next cycle [11]. The decimal values of the digital, negative velocity signals were scaled to binary representation and then written to the D/A converter of the I/O board at the end of each cycle of the program. The digital approximate integrators and the return signals to the truss were dependent on the computational time required to execute each cycle of the VI based program. After the completion of each cycle, the output signals were sent to the I/O board and new input values were obtained. Therefore the sampling period of the digital controller was based on the computational speed of the digital computer to execute one cycle or loop of the program. The sampling period cannot be smaller than the computational time required to execute one cycle, but can be longer. A millisecond "wait" VI in LABVIEW causes the execution of the code to "wait" a specific number of milliseconds before completing the execution of the cycle and beginning another. The "wait" causes the computational delay to be constant unless the time required to complete the cycle is longer than specified time.

Computational delays and therefore the sampling periods of the digital controllers were a direct result of the complexity of the program and digital approximate integrators. The original VI block diagrams utilized the data acquisition capabilities of LABVIEW to observe the signals flowing in and out of the program as well as the values computed within each of the execution cycles. These VIs provided plots, in the front panels, as well as numerical updates of any number of values within the block diagram structure. The complexity of the system created a dramatic increase in computational time due to automatic screen refreshing and the additional computations required to plot the data on the screen. Although the graphic displays were helpful in observing the signals, all of the extraneous data acquisition and numerical updates were removed from the front panels and the block diagrams for the final implementation of the control laws.

The computational time required for the execution of one cycle of the program

was determined by forcing the code to execute a large number of cycles and recording the time required to complete the process. The total execution time was divided by the specified number of cycles to evaluate the computational time delays associated with each cycle. The computational time was determined to be between 9 and 10 milliseconds and therefore, a 10 millisecond "wait" was implemented into the block diagram to keep the sampling period constant. The emulation of the analog control laws for implementation was therefore based on a 10 millisecond sampling period (T).

#### *4.5 Digital AJT Controller*

Just as with the continuous control laws, the first attempt at active damping of the UWCSL truss through digital control laws was with negative velocity feedback to the tip and midpoint AJTs. The truss mounted accelerometers at the tip and midpoint were used to obtain the acceleration signals. The adjusted acceleration signals, the difference between the acceleration signals and the respective D.C offsets, were processed through a sampler or A/D converter to obtain the digital signals. The outputs of the digital approximate integrators are the digital, negative velocity signals of the tip and midpoint of the truss. The digital velocity signals were converted to piecewise continuous velocity signals through the use of a zero-order hold (ZOH) and routed through the AJT control circuits to fire the AJTs which dampen the vibrations of the truss. The control law for digital AJT vibration suppression is a fourth order, two-input, two-output controller comprised of two uncoupled second order, digital approximate integrators.

##### *4.5.1 Non-Linear Simulation*

SIMULINK [14] was used to simulate the truss and the digital control law for AJT vibration suppression. A block diagram of the SIMULINK closed loop system for the digital AJT controller is in Appendix E. The eighth order finite element model developed in Section 2.4.4 was used in simulation because the RMAs were not connected to the truss hardware in the AJT controller configuration. The tip and midpoint digital approximate integrators were modeled as discrete blocks in SIMULINK using the digital state space equations which were derived using Tustin's method in Section 4.3. Each of the discrete blocks in SIMULINK has a built-in sampler at its input and

a zero-order hold at its output. A 10 millisecond sample period ( $T$ ) was specified for each of the discrete blocks, as this was the smallest sampling period LABVIEW could achieve due to computational delays. When the discrete blocks are mixed with continuous blocks in simulation, the output in between the sampling time of the discrete blocks is held constant with a zero-order hold function. The inputs to the discrete blocks are updated only at the specified sampling periods [14]. The AJTs were modeled as the same non-linear actuators used in the analog simulation.

The simulation used a sinusoidal function, at the resonant natural frequencies of the first four modes of the truss, as the input signal to the tip AJTs to excite the truss model to its bending modes. The excitation signal was processed through a switch which controlled the length of time that the truss was excited before the controllers were activated. The excitation time was adjusted to closely match the magnitude of the acceleration signals of the digital simulation to the magnitude of the acceleration signals from analog simulation. Figure 4.2 is a plot of the simulated tip accelerations for the first four modes of the truss in a closed loop model implementing the digital AJT control law with a sampling period of 10 milliseconds. The simulation results in Figure 4.2 predict the response of the truss to the digital AJT controller. The excitations between 4 and 6 seconds in the first mode results were due to the same misfiring of the tip AJTs that occurred in the simulated analog AJT controller due to a problem in the modeling of the non-linear dead-band of the AJT solenoid valves. This burst of acceleration is not expected to be present in the experimental results.

Comparison of the simulated acceleration plots of the analog AJT controller and the digital AJT controller with a sampling period of 10 milliseconds (Figures 3.3 and 4.2) reveals the close approximation of the digitized controller to the continuous control law. The plots of the digital acceleration signals have slightly longer settling times than the analog results due to the discrete nature of the signal and the computational delays of the computer, but this difference is minimal. Both the analog and digital AJT controllers were effective in increasing the damping of the first two modes of the truss and had little effect on the third and fourth modes. Table 4.2 shows approximate simulated settling times (S. Time) of the open loop model, without RMAs, the analog AJT controller, and the digital AJT controller. As previously discussed, the damping ratios were not calculated for the simulation results.

Simulation results predict that the theoretical response of the truss to the digital

Table 4.2: Digital AJT Controller: Approximate Simulation Settling Times in Seconds

Mode	S. Time (O.L.)	S. Time (Analog)	S. Time (Digital)
1	40	4	4.5
2	12	3	3
3	3	3	3
4	2	2	2

AJT controller will be close to the response of the truss to the analog AJT controller. The next logical step was implementation of the controller through a digital computer to the truss hardware to verify the simulation results.

#### 4.5.2 Experimental Results

The truss was excited to its first four bending modes using the fixed sine function of an HP Dynamic Signal Analyzer (DSA) as the control input to the tip AJTs. Acceleration at the truss tip and midpoint was recorded from the accelerometers at their respective positions. Once a full range of motion was recorded by the accelerometers, the excitation signal was shut off and the digital AJT controller was activated. The acceleration signals were processed through the A/D converter on the digital signal processing (DSP) board and read into the LABVIEW digital AJT controller program. After LABVIEW scaled the binary signal from the DSP boards into decimal values, the difference between the accelerometer output signal and the tip accelerometer DC offset was used to form the adjusted acceleration signals ( $e_{ai}$ ). The adjusted acceleration signals are the inputs to the digital state space equations of the approximate integrators. The negative tip and midpoint velocity signals out of the digital approximate integrators were converted to binary values and returned to the DSP board. The signals were passed through the D/A converter to create the piecewise continuous signals which were used by the AJT control circuits to fire the AJTs to dampen truss vibrations.

Figure 4.3 and Figure 4.4 are plots of the experimental tip and midpoint acceler-

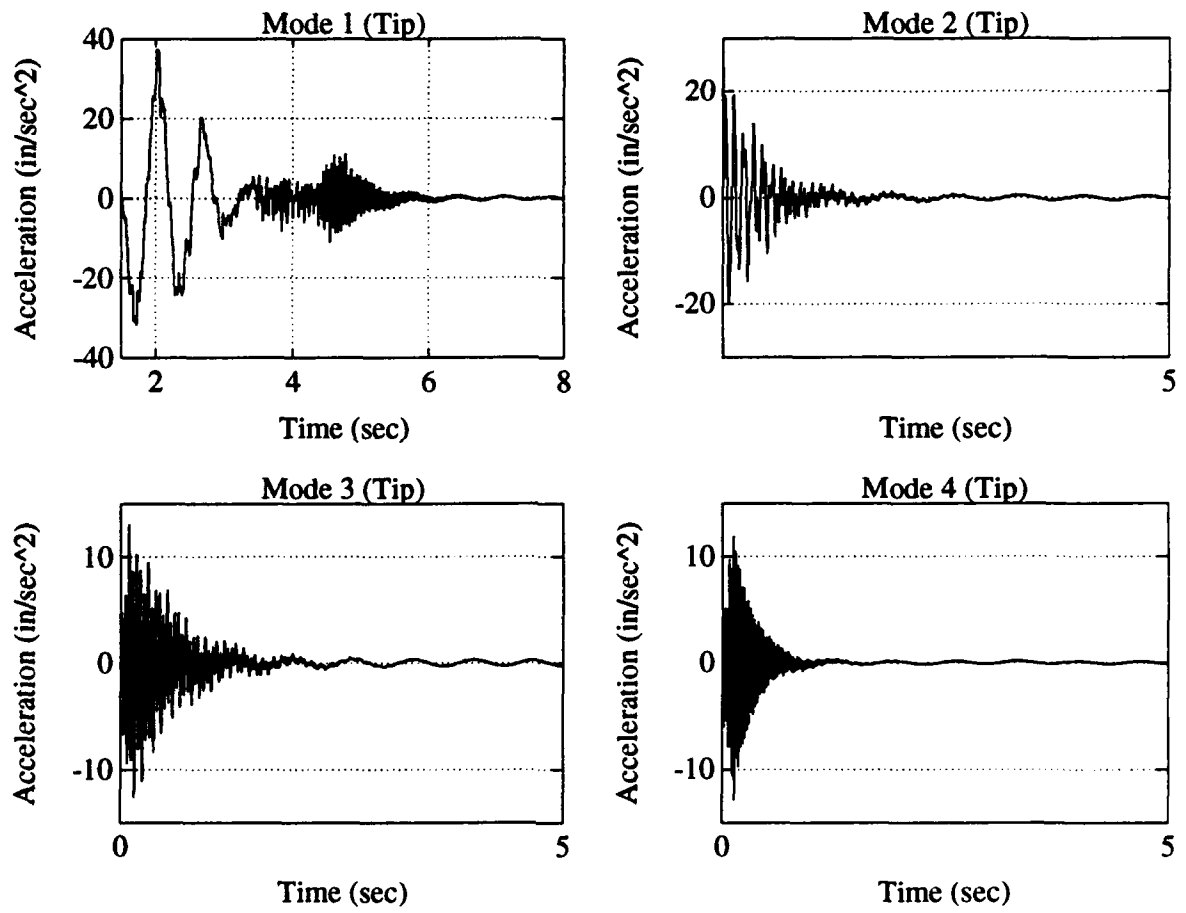


Figure 4.2: Simulation of Digital AJT Controller

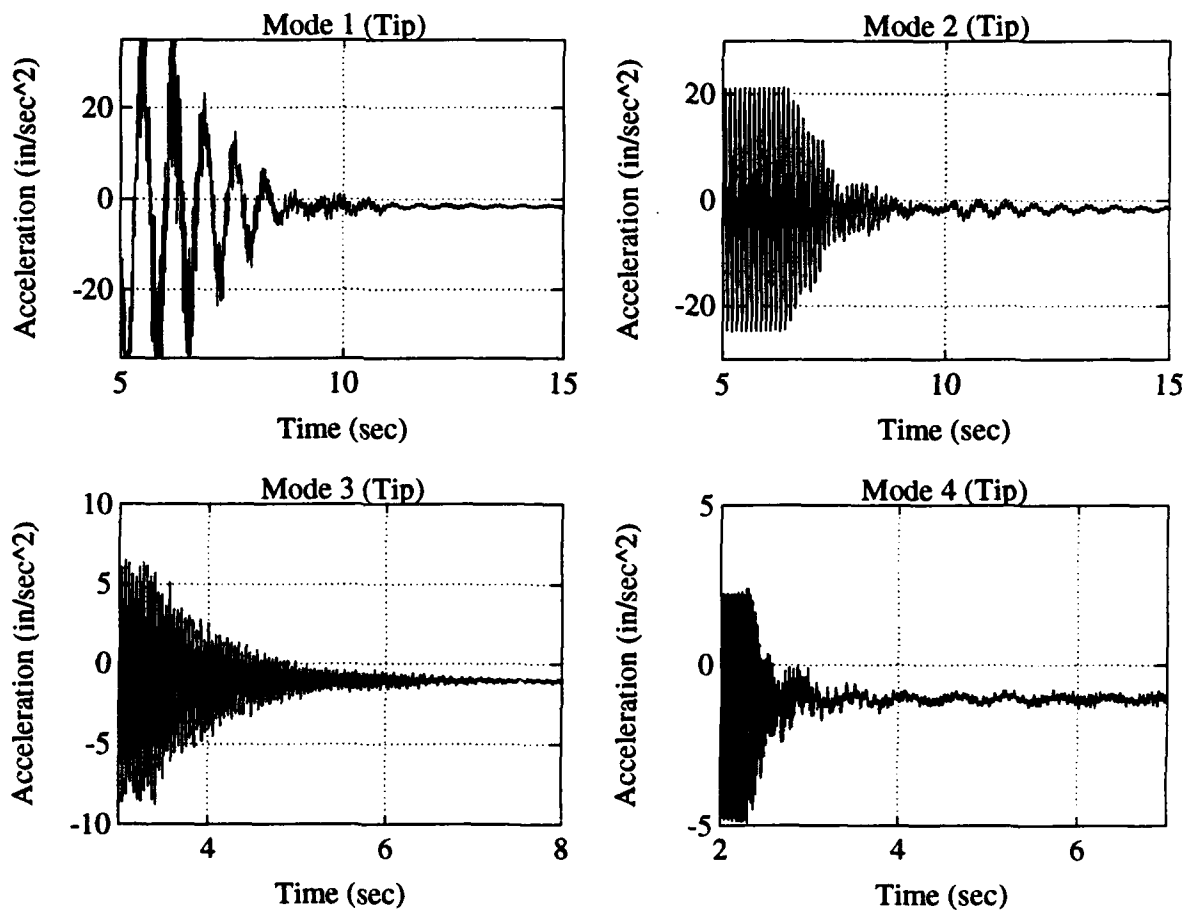


Figure 4.3: Experimental Digital AJT Controller

ation signals of the UWCSL truss with active damping provided by the digital AJT controller. The experimental results matched the non-linear simulation predicted results with approximately equal settling times for the tip acceleration plots. The experimental results did not create the large disturbances seen in the first mode of the simulation due to AJT dead-band related misfirings. It should be noted that the AJTs did not fire to dampen the third and fourth modes of the truss. This is the same result seen in the analog AJT controller and discussed in Section 3.3. Table 4.3 shows a comparison of the experimental damping ratios of the experimental open loop truss ( $\zeta_{AJT}$ ), the closed loop analog AJT controller ( $\zeta_{clAJT}$ ), the closed loop digital AJT controller ( $\zeta_{clDAJT}$ ). The damping ratios were calculated using the logarithmic

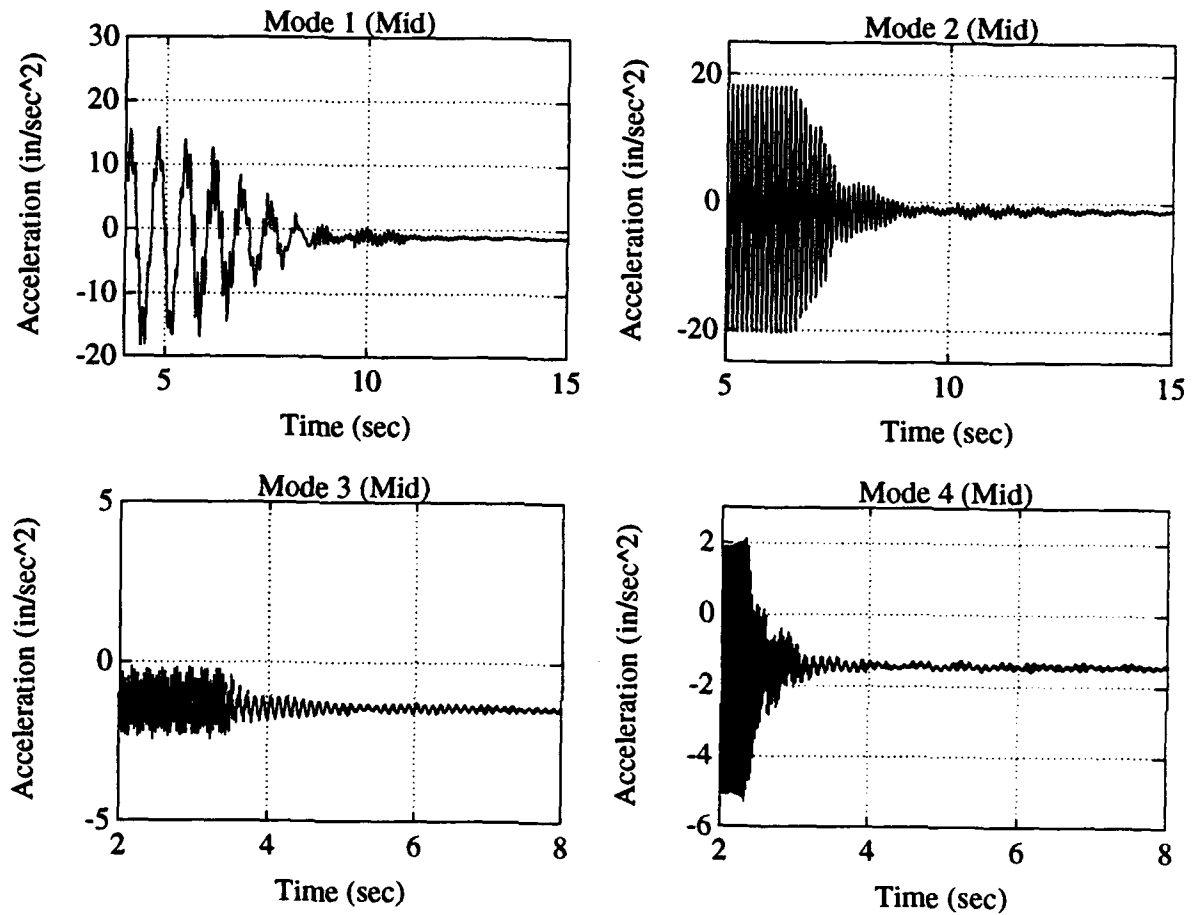


Figure 4.4: Experimental Digital AJT Controller

decrement method. The damping ratios for the third and fourth modes of the digital AJT controller were not calculated due to the difficulty in isolating the desired mode shapes from the multiple modes recorded during experimental measurements and the fact that the AJTs did not fire to dampen these modes. Table 4.3 also shows comparison of the settling times (S.T.) of the open loop truss, the analog AJT controller, and the digital AJT controller. The digital AJT controller performed as expected, closely matching the experimental damping ratios and settling times of the analog AJT controller for the first two modes.

The experimental results demonstrate the similarity of the digital AJT controller and the analog AJT controller for vibration suppression of the first two modes and

Table 4.3: Digital AJT Controller: Experimentally Determined Damping Ratios

Mode	$\zeta_{AJT}$	$\zeta_{clAJT}$	$\zeta_{clDAJT}$	S.T.(O.L.)	S.T.(Analog)	S.T.(Digital)
1	0.01190	0.05383	0.05844	35.75	6.44	5.45
2	0.00863	0.02356	0.02046	12.84	2.72	2.61
3	0.01307	0.01002	-	4.80	2.63	2.62
4	0.01555	0.00646	-	1.44	0.70	0.72

verify the simulation predicted results.

#### 4.6 Digital RMA Controller

The second attempt at active damping of the UWCSL truss through digital control laws was with negative relative velocity feedback to the tip and midpoint RMAs. The relative velocity feedback process was previously discussed in Section 3.4. The truss mounted accelerometers at the tip and midpoint of the truss and the RMA structure mounted accelerometers were used to obtain the acceleration signals. The acceleration signals at each truss location are multiplied by gains in order to match the magnitudes of the truss and RMA signals. The adjusted acceleration signals are the difference of the resulting accelerometer signals at each truss location. The adjusted acceleration signals are processed through a sampler or A/D converter to obtain the digital signals. The outputs of the digital approximate integrators are the digital, negative relative velocity signals of the tip and midpoint of the truss. The digital velocity signals are converted to piecewise continuous velocity signals through the use of a zero-order hold and routed through the RMA amplifiers to cause the RMAs to dampen the vibrations of the truss. The control law for digital RMA vibration suppression is a fourth order, four-input, two-output controller comprised of two uncoupled second order, digital approximate integrators with two constant gains in simulation and four constant gains in experimentation.

#### 4.6.1 *Non-Linear Simulation*

SIMULINK [14] was used to simulate the truss and the digital control law for RMA vibration suppression. A block diagram of the SIMULINK closed loop system for the digital RMA controller is in Appendix E. The twelfth order finite element model developed in Section 2.4.5 was used in this simulation. The tip and midpoint digital approximate integrators were modeled as discrete blocks in SIMULINK using the digital state space equations which were derived using Tustin's method in Section 4.3. Each of the discrete blocks in SIMULINK has a built-in sampler at its input and a zero-order hold at its output. A 10 millisecond sample period ( $T$ ) was specified for each of the discrete blocks, as this was the smallest sampling period LABVIEW could achieve due to computational delays. The RMA models were developed in Section 2.3.

Just as in the AJT controller simulation, a sinusoidal function, at the resonant natural frequencies of the first four modes of the truss, was the input signal to the tip AJTs to excite the truss model to its bending modes. The excitation signal was processed through a switch which controlled the length of time that the truss was excited before the controllers were activated. The excitation time was adjusted to closely match the magnitude of the acceleration signals of the digital simulation to the magnitude of the acceleration signals from analog simulation. Figure 4.5 is a plot of the tip accelerations for the first four modes of the truss in a closed loop model implementing the digital RMA control law with a sampling period of 10 milliseconds. The simulation results in Figure 4.5 predict the response of the truss to the digital RMA controller.

Comparison of the simulated acceleration plots of the analog RMA controller and the digital RMA controller with a sampling period of 10 milliseconds (Figures 3.6 and 4.5) reveals the close approximation of the digitized controller to the continuous control law. The plots of the digital acceleration signals have longer settling times than the analog results, for the last three modes, due to the discrete nature of the signal and the computational delays of the computer. The digital RMA simulation settling times are still of the same order magnitude as the analog RMA settling times and less than the open loop model in all but the fourth mode. Both the analog and digital AJT controllers were effective in increasing the damping of the second

Table 4.4: Digital RMA Controller: Approximate Simulation Settling Times in Seconds

Mode	S. Time (O.L.)	S. Time (Analog)	S. Time (Digital)
1	40	20	20
2	12	2	3
3	3	1.5	2.5
4	2	1	2

and third modes of the truss. The analog controller had more effect on the fourth mode of the truss than the digital controller which was due to the higher frequency of this mode and the restricted sampling time of the digital controller. The sampling period, 10 milliseconds, was less than the recommended 50 times the frequency of the fourth mode of the truss. The A/D converter on the NB-MIO-16 I/O board converted the analog signal to a 12-bit word size and not the recommended 16-bit word size [4]. The effect of these hardware restrictions creates a less than ideal approximation of the continuous signal at higher frequencies. This results in some computational errors when applying the emulation method to digitize the continuous controller. This could be the reason that the digital controller simulation plots have more acceleration signal oscillations than the analog RMA controller simulation plots. Table 4.4 shows approximate simulated settling times (S. Time) of the open loop model, without RMAs, the analog AJT controller, and the digital AJT controller. Again, the damping ratios were not calculated for the simulation results. The simulation results in Figure 4.5 predict the response of the truss to the digital RMA controller. The next step is to implement the digital RMA controller experimentally.

#### 4.6.2 Experimental Results

The truss was excited to its first four bending modes using the fixed sine function of an HP Dynamic Signal Analyzer (DSA) as the control input to the tip AJTs. Acceleration at the truss tip and midpoint was recorded from the accelerometers at their respective positions. Once a full range of motion was recorded by the accelerome-

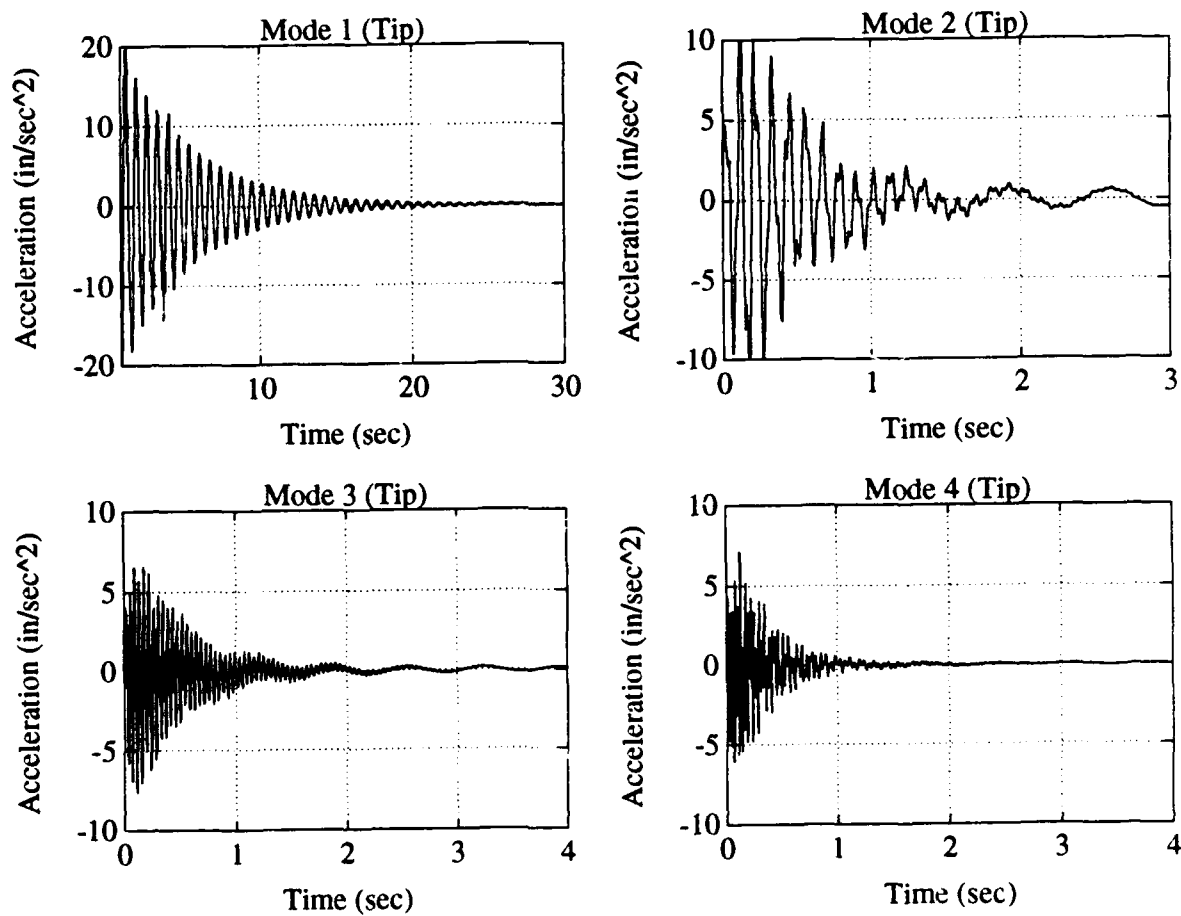


Figure 4.5: Simulation of Digital RMA Controller

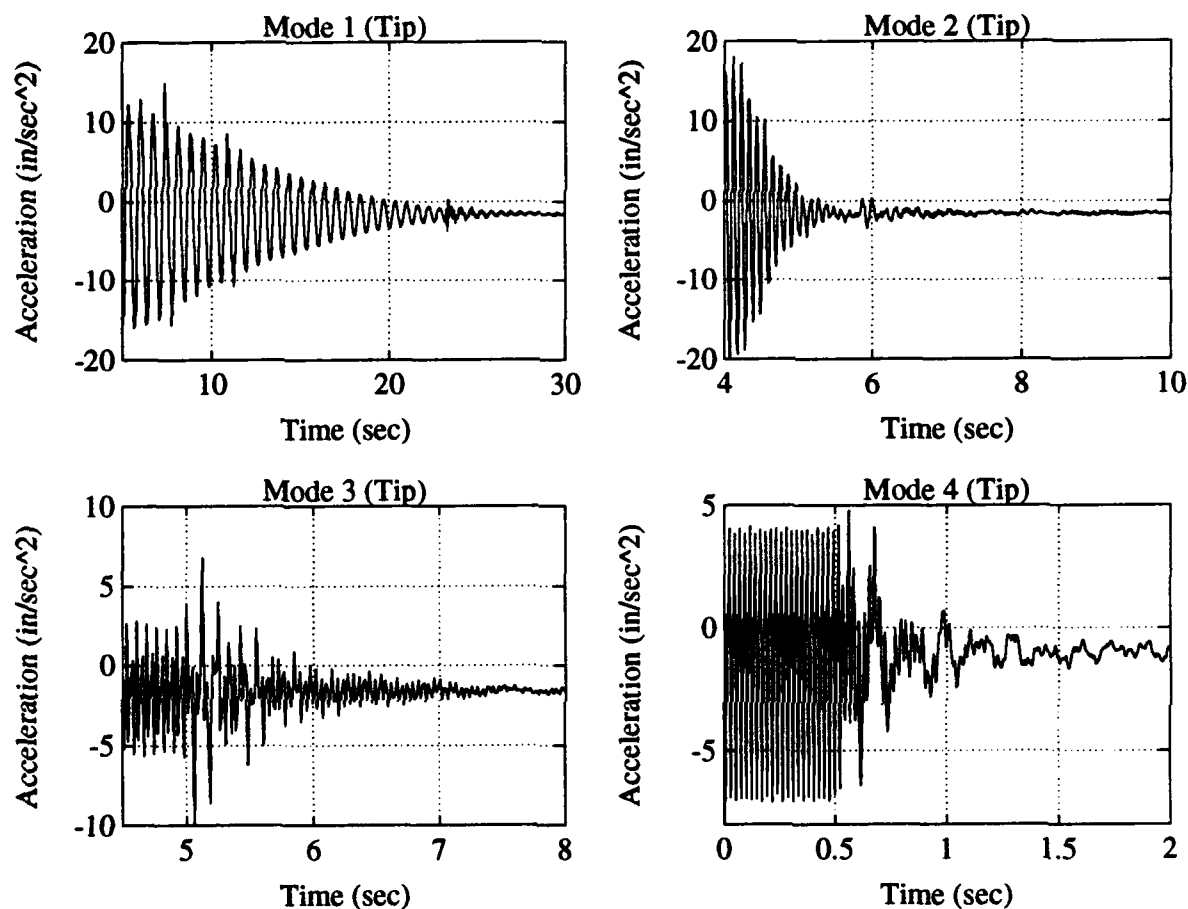


Figure 4.6: Experimental Digital RMA Controller

ters, the excitation signal was shut off and the digital RMA controller was activated. The four acceleration signals were processed through the A/D converter on the digital signal processing (DSP) board and read into the LABVIEW digital AJT controller program. The LABVIEW program then scaled the binary signal from the DSP boards into decimal values. Gains were applied to the truss mounted accelerometer signals in order to match the magnitudes of the truss and RMA accelerometer signals. The difference of the new truss mounted acceleration signals and the acceleration signals of the RMA mounted accelerometers at each truss location was used to form the adjusted acceleration signals ( $e_{ai}$ ). The adjusted acceleration signals are the inputs to the digital state space equations of the approximate integrators. The negative tip

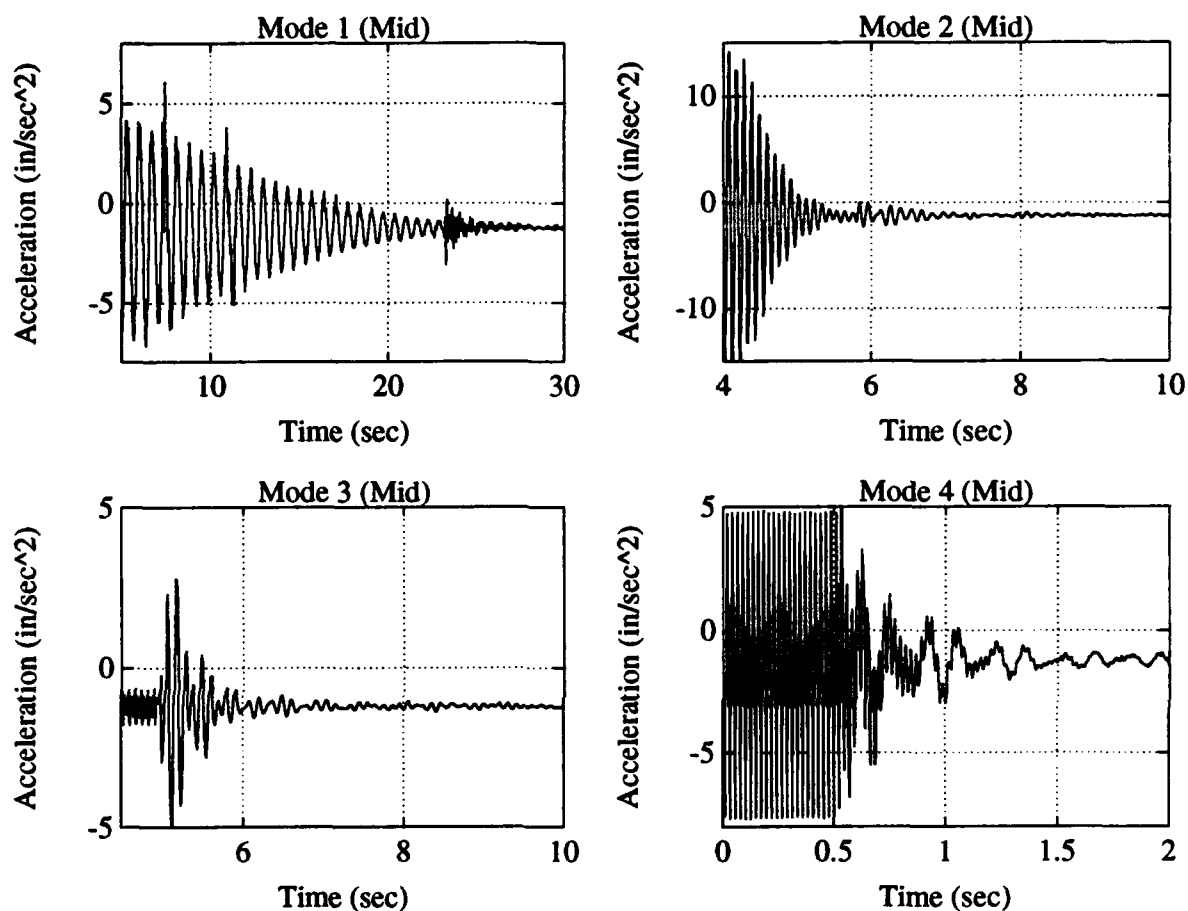


Figure 4.7: Experimental Digital RMA Controller

and midpoint relative velocity signals out of the digital approximate integrators were converted to binary values and returned to the DSP board. The signals were passed through the D/A converter to create the piecewise continuous signals which were passed to the RMA amplifiers which caused the RMAs to dampen truss vibrations.

Figure 4.6 and Figure 4.7 are plots of the experimental tip and midpoint acceleration signals of the UWCSL truss with active damping provided by the digital RMA controller. The experimental results were similar to the non-linear simulation predicted results in that the settling time of the tip accelerations of both were approximately equal. The RMA controller did little to control the first mode of the truss as predicted by the simulation and was the same result seen in the analog RMA

Table 4.5: Digital RMA Controller: Experimentally Determined Damping Ratios ( $\zeta_{clDRMA}$ )

Mode	$\zeta_{AJT}$	$\zeta_{clRMA}$	$\zeta_{clDRMA}$	S.T.(O.L.)	S.T.(Analog)	S.T.(Digital)
1	0.01190	0.02323	0.01120	40	16.97	22.97
2	0.00863	0.02594	0.02705	12	2.92	2.81
3	0.01307	0.01169	-	3	2.60	2.52
4	0.01555	0.01177	-	2	0.63	1.00

controller discussed in Section 3.4. The experimental acceleration plots of the third mode have a spike in acceleration when the digital RMA controller is activated which is larger than the amplitude of the steady state mode excitation. This was due to a pulse through the controller when the RMA controller was activated. Table 4.5 shows a comparison of the experimental damping ratios of the experimental open loop truss ( $\zeta_{AJT}$ ), the closed loop analog RMA controller ( $\zeta_{clRMA}$ ), and the closed loop digital RMA controller ( $\zeta_{clDRMA}$ ). The damping ratios were calculated using the logarithmic decrement method. The damping ratios for the third and fourth modes of the digital RMA controller were not calculated due to the difficulty in isolating the desired mode shapes from the multiple modes recorded during experimental measurements. Table 4.5 also shows a comparison of the settling times (S.T.) of the open loop truss, the analog RMA controller, and the digital RMA controller. The digital AJT controller performed as expected, closely matching the experimental damping ratios and settling times of the analog AJT controller for the first two modes.

The experimental results demonstrate the similarity of the digital RMA controller and the analog RMA controller for vibration suppression of the first two modes and verify the simulation predicted results.

#### 4.7 Digital Hybrid Controller

As in the analog controller design process, discussed in Chapter 3, it is expected that a more effective digital controller will be achieved if both the digital AJT and digital

RMA controllers are used together in a hybrid configuration. The digital hybrid controller is the combination of the digital AJT and digital RMA controllers where no design effort is made to couple the two controllers. The second mode vibrations of the truss are damped by both the digital AJT and digital RMA controllers when functioning independently and therefore, the digital hybrid controller is predicted to have its best results on the second mode. The control law for digital hybrid vibration suppression is an eighth order, four-input, four-output controller comprised of four uncoupled second order, digital approximate integrators with two constant gains in simulation and four constant gains in experimentation.

#### *4.7.1 Non-Linear Simulation*

SIMULINK [14] was used to simulate the truss and the digital control law for digital hybrid vibration suppression. A block diagram of the SIMULINK closed loop system for the digital hybrid controller is in Appendix E. The twelfth order finite element model developed in Section 2.4.5 was used in this simulation. The digital hybrid controller in simulation is simply the combination of the digital AJT and digital RMA simulated controllers from Sections 4.5 and 4.6.

Again, a sinusoidal function, at the resonant natural frequencies of the first four modes of the truss, was the input signal to the tip AJTs to excite the truss model to its bending modes. The excitation signal was processed through a switch which controlled the length of time that the truss was excited before the controllers were activated. The excitation time was adjusted to closely match the magnitude of the acceleration signals of the digital simulation to the magnitude of the acceleration signals from analog simulation. Figure 4.8 is a plot of the tip accelerations for the first four modes of the truss in a closed loop model implementing the digital RMA control law with a sampling period of 10 milliseconds. The simulation results in Figure 4.8 predict the response of the truss to the digital RMA controller. The excitations between 4 and 6 seconds in the first mode results were due to the same misfiring of the tip AJTs that occurred in the simulated hybrid AJT controller due to a problem in the modeling of the non-linear dead-band of the AJT solenoid valves. The excitation is larger than the digital AJT simulation results due to the addition of the digital RMA controllers damping the higher frequencies of this excitation. This burst of accelera-

tion is not expected to be present in the experimental results as demonstrated in the analog hybrid controller experimental results. A small excitation from the activation of the RMAs may occur during experimentation with the digital hybrid controller, as was shown in the experimental analog hybrid acceleration plots (Figures 3.10 and 3.11).

Comparison of the simulated acceleration plots of the analog AJT controller and the digital AJT controller with a sampling period of 10 milliseconds (Figures 3.3 and 4.8) reveals the close approximation of the digitized controller to the continuous control law. The plots of the digital acceleration signals have longer settling times than the analog results due to the discrete nature of the signal and the computational delays of the computer. At higher frequencies, the digital hybrid controller did not perform as well as the analog hybrid controller because of the restricted sampling period of the digital controller. Both the simulated analog and digital hybrid controllers were equally effective in increasing the damping of all the modes of the truss. Table 4.6 shows approximate simulated settling times (S. Time) of the open loop model, without RMAs, the analog hybrid controller, and the digital hybrid controller. As previously discussed, the damping ratios were not calculated for the simulation results.

Experimental implementation of the digital hybrid controller was not accomplished due to restrictions on number of outputs available on the digital signal processing board. At this time, only two output signals can be returned from the digital computer to the hardware. One of the recommendations for future research on the UWCSL truss is the implementation of the digital hybrid controller. Experimental results of the digital hybrid controller should resemble the simulated results presented in this thesis.

Table 4.6: Digital Hybrid Controller: Approximate Simulation Settling Times in Seconds

Mode	S. Time (O.L.)	S. Time (Analog)	S. Time (Digital)
1	40	4	5
2	12	2	2.5
3	3	2	2.5
4	2	1	1.5

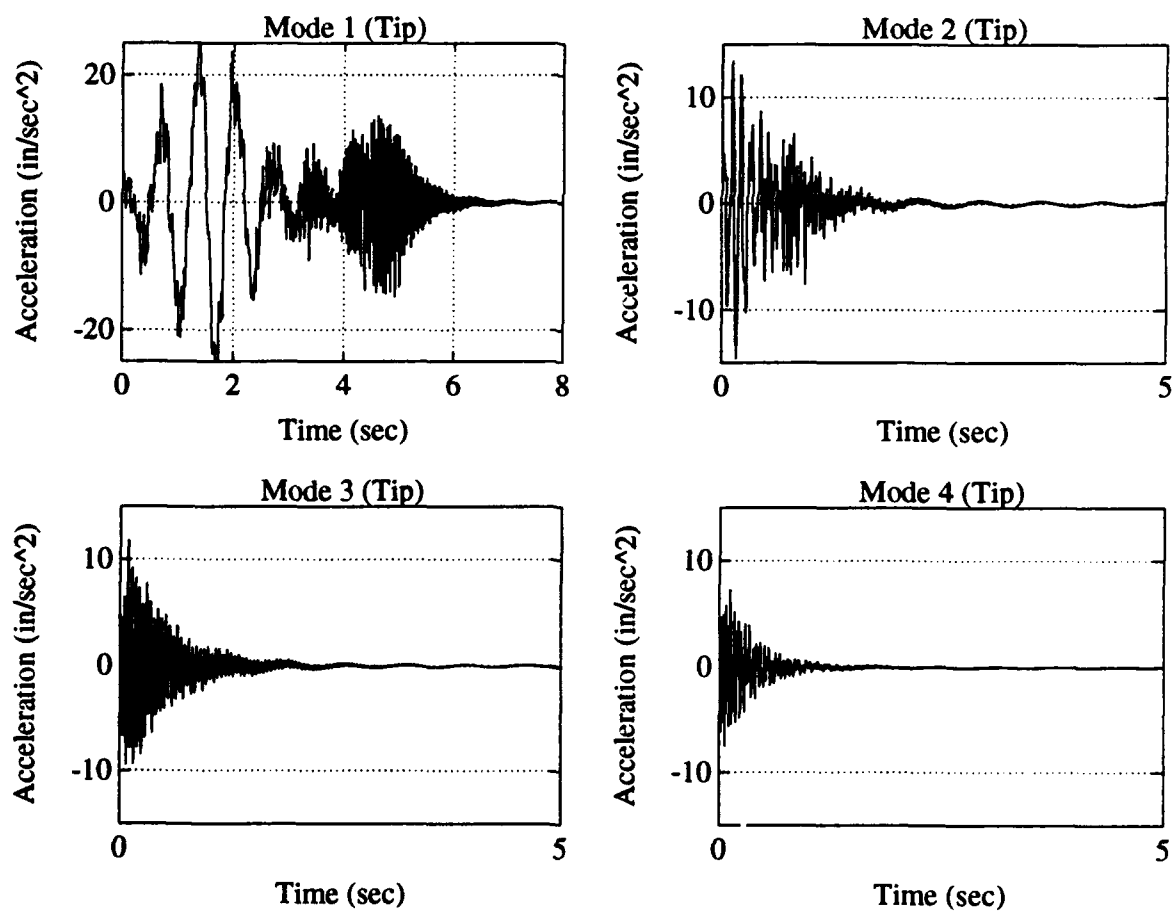


Figure 4.8: Simulation of Digital Hybrid Controller

## Chapter 5

# LINEAR QUADRATIC REGULATOR DESIGN

### 5.1 Overview

In Chapters 2 and 3, analog and digital classical control laws were theoretically developed, simulated, and experimentally implemented to control the vibrations of the UWCSL truss. These continuous and digital controllers used negative velocity feedback to the AJTs and RMAs, both independently and in a hybrid configuration, to effectively dampen the first four bending modes of the truss. Although the controllers, especially the hybrid method, obtained significant decreases in the settling times and appreciable increases in the damping ratios of the UWCSL truss, the question of whether the controllers' performance was accomplished in the best possible or optimal manner still arises. The search for an optimal solution is arbitrary unless a mathematical description of the optimal problem is defined.

The description of an optimal control problem consists of the system to be controlled, the task to be accomplished, the constraints on the system, and the criterion for judging performance [3]. In this chapter we examine the theoretical development and simulation of the optimal Linear Quadratic Regulator (LQR) method of control law design for the reaction mass actuators (RMAs) using the twelfth order model of the truss (see Section 2.4.5). Simulation results for the LQR full-state feedback controller for the RMAs, acting independently and in a hybrid configuration with the analog AJT controller from Chapter 3 are presented.

### 5.2 Full-State Feedback Design Problem

The development of the twelfth order model of the truss was described in Section 2.4.5 and this model was used in the LQR controller design for RMA actuation. The state vector  $\mathbf{x}$  used in this model was previously defined as

$$\mathbf{x} = \begin{bmatrix} \mathbf{q}_r \\ \mathbf{q}_r \end{bmatrix} = \begin{pmatrix} q_{tip} \\ q_{3/4} \\ q_{mid} \\ q_{1/4} \\ q_{5-1} \\ q_{6-3} \\ q_{tip} \\ q_{3/4} \\ q_{mid} \\ q_{1/4} \\ q_{5-1} \\ q_{6-3} \end{pmatrix} \quad (5.1)$$

The control inputs, for RMA actuation, are:

$$\mathbf{u} = \begin{pmatrix} u_1 \\ u_2 \end{pmatrix} = \begin{pmatrix} f_{5-1(tip)} \\ f_{6-3(mid)} \end{pmatrix} \quad (5.2)$$

The full-state feedback, linear quadratic regulator (LQR) design method assumes that all of the states of the system are available for feedback to the control signal. This assumption is valid for theoretical development and non-linear simulation but is unrealistic for experimental applications. Experimental implementation would require the development of an observer or optimal linear state estimator to estimate the states which cannot be measured directly or the addition of more sensors to the truss. Another assumption of the LQR design is the absence of stochastic processes in the controller design. The sensor noise disturbances in the accelerometers and input disturbances in the reaction mass actuators were neglected in this study. Future designs for an optimal RMA controller will have to include noise.

The truss model for which the optimal LQR controller is to be designed can be expressed as the following state space equation:

$$\begin{aligned} \dot{\mathbf{x}}(t) &= \mathbf{A}\mathbf{x}(t) + \mathbf{B}\mathbf{u}(t) \\ \mathbf{y}(t) &= \mathbf{C}\mathbf{x}(t) \end{aligned} \quad (5.3)$$

where the (A,B) are controllable and the initial condition is given as  $x(t_0) = x_0$  [18]. The design is for full-state feedback and therefore the output vector ( $y(t)$ ) can be defined as the state vector ( $C =$  the identity matrix). The problem is to determine a linear feedback control law for  $u(t)$  which minimizes the performance index or "cost" function [12]:

$$J(x_0, u, t_f) = \frac{1}{2}x^T(t_f)S_f x(t_f) + \frac{1}{2} \int_{t_0}^{t_f} [x^T(t)Qx(t) + u^T(t)Ru(t)]dt \quad (5.4)$$

The performance index (J) consists of a quadratic form of the terminal state  $x(t_f)$  plus an integral of a quadratic form of the state  $x(t)$  and control  $u(t)$  where  $S_f$  and  $Q$  are positive semi-definite matrices and  $R$  is a positive definite matrix [12].  $Q$  is the weighting or penalty matrix on the linear combination of the state variables and  $R$  is the weighting matrix on the control inputs. The selection of these weighting matrices will completely determine the control law of the system [12].

The control law,  $u(t)$ , which minimizes the performance index in Equation 5.4 is determined through calculus of variation using the maximum principle and assuming that the state vector satisfies the differential equations in Equation 5.3. The derivation for the solution of the control law,  $u(t)$ , is explicitly detailed by Sage [18]. The optimal control signal for the regulator problem is defined as

$$u(t) = Kx(t). \quad (5.5)$$

The optimal full-state feedback gain matrix ( $K$ ) is given by [13]:

$$K = -R^{-1}B^T P \quad (5.6)$$

where  $P$  is a symmetric positive definite solution of the steady-state algebraic Riccati equation (ARE) [13, 18] which has the following matrix equation form:

$$A^T P + PA - PBR^{-1}B^T P + Q = 0 \quad (5.7)$$

The optimal control signal for the regulator program, expressed in Equation 5.5, can therefore be rewritten as:

$$u(t) = -R^{-1}B^T P x(t). \quad (5.8)$$

The performance index ( $J_{min}$ ) which corresponds to the optimal linear feedback control law in Equation 5.8 is given by

$$J_{min} = \frac{1}{2} \int_{t_0}^{t_f} [x^T(t)Qx(t) + u^T(t)Ru(t)]dt \quad (5.9)$$

since  $x(t_f) \rightarrow 0$  as  $t_f \rightarrow \infty$ .

The optimal full-state feedback control system possesses the following guaranteed robustness properties in any control loop:

$$\begin{aligned} \text{Gain Margins : } & -6dB \geq G.M. < \infty \\ \text{Phase Margins : } & -60^\circ \geq P.M. \leq 60^\circ \end{aligned} \quad (5.10)$$

As previously stated, the selection of the weighting matrices, Q and R, will determine the control law of the system. The challenge of design, therefore, rests with the selection of the values of the Q and R weighting matrices. For simplicity, the weighting matrices are generally chosen to be diagonal, with only one penalty for each state or control input of the system. The cost function for the diagonal weighting matrices Q and R can be written [12]:

$$J = \frac{1}{2} \int_0^\infty [y^T(t)Qy(t) + u^T(t)Ru(t)]dt \quad (5.11)$$

or

$$J = \frac{1}{2} \int_0^\infty \left[ \sum_{i=1}^p Q_{ii}y_i^2(t) + \sum_{i=1}^m R_{ii}u_i^2(t) \right] dt \quad (5.12)$$

where  $y = x$  for full-state feedback. Bryson suggested a guideline for selecting the initial diagonal elements or penalties,  $Q_{ii}(i=1,p)$  and  $R_{ii}(i=1,m)$  of the weighting matrices [12]. Bryson's rules are

$$Q_{ii} = \frac{1}{y_{i\max}^2} \quad (5.13)$$

and

$$R_{ii} = \frac{1}{u_{i\max}^2} \quad (5.14)$$

where  $y_{i \max}$  and  $u_{i \max}$  are the maximum allowable excursions in the output response  $y_i$  and in the control  $u_i$  respectively [12]. These values are a good starting point for the design procedure which requires some trial-and-error to achieve the desired design objectives and performance specifications. The resulting weighting matrices (Q and R) on the states and control inputs for this design are:

Q =

$$\begin{bmatrix}
 10000 & 0 & 0 & 0 & 0 & 0 & 0 & 0 & 0 & 0 & 0 & 0 \\
 0 & 1000 & 0 & 0 & 0 & 0 & 0 & 0 & 0 & 0 & 0 & 0 \\
 0 & 0 & 1000 & 0 & 0 & 0 & 0 & 0 & 0 & 0 & 0 & 0 \\
 0 & 0 & 0 & 1000 & 0 & 0 & 0 & 0 & 0 & 0 & 0 & 0 \\
 0 & 0 & 0 & 0 & 100 & 0 & 0 & 0 & 0 & 0 & 0 & 0 \\
 0 & 0 & 0 & 0 & 0 & 100 & 0 & 0 & 0 & 0 & 0 & 0 \\
 0 & 0 & 0 & 0 & 0 & 0 & 100 & 0 & 0 & 0 & 0 & 0 \\
 0 & 0 & 0 & 0 & 0 & 0 & 0 & 10 & 0 & 0 & 0 & 0 \\
 0 & 0 & 0 & 0 & 0 & 0 & 0 & 0 & 100 & 0 & 0 & 0 \\
 0 & 0 & 0 & 0 & 0 & 0 & 0 & 0 & 0 & 1 & 0 & 0 \\
 0 & 0 & 0 & 0 & 0 & 0 & 0 & 0 & 0 & 0 & 1 & 0 \\
 0 & 0 & 0 & 0 & 0 & 0 & 0 & 0 & 0 & 0 & 0 & 1
 \end{bmatrix}$$

R =

$$\begin{bmatrix}
 1 & 0 \\
 0 & 1
 \end{bmatrix}$$

Numerically solving the algebraic Riccati equation given in Equation 5.7 results in the full-state feedback gain matrix (K):

$$K^T =$$

$$\begin{bmatrix} -39.284 & -1.091 \\ 37.904 & 1.287 \\ 3.984 & -6.109 \\ 3.905 & 3.734 \\ 10.816 & 0.170 \\ 0.305 & 10.119 \\ -3758.4 & -470.56 \\ 4993.7 & 3580.1 \\ -590.69 & -7057.8 \\ -1806.9 & 2706.8 \\ 0.030 & -0.090 \\ 0.098 & 0.028 \end{bmatrix}$$

Some of the gains in the full-state feedback gain matrix are large and could cause problems during experimental implementation of the controller although the magnitude of the gains is not a concern during simulation. It should be noted that the high gains in the full-state feedback gain matrix are on the states describing the displacement of the truss at the tip, 3/4, mid, and 1/4 locations. By examining the controllability matrix of the system, it is seen that the system is weakly controllable through the truss displacement states which prescribes the use of high feedback gains. The gains on all of the velocity states and the relative displacement states are of magnitudes which are realizable in hardware. It should also be noted that the performance of the full-state controller should be better than the velocity feedback controllers because of the additional sensors at the 3/4 and 1/4 points of the truss as well as the feedback of displacement.

Two simulations of the RMA full-state feedback control laws were accomplished on SIMULINK. The first simulation was the simply the full-state feedback controller to the reaction mass actuators. The second simulation was a hybrid controller which utilized the classical AJT controllers discussed in Chapters 3 and 4 and the full-state feedback control laws to the RMAs. These simulations and their results are presented in the following sections.

### 5.3 Non-Linear Simulation of Full-State Feedback to the RMAs

SIMULINK [14] was used to simulate the truss and the full-state feedback control law for RMA vibration suppression. A block diagram of the SIMULINK closed loop system for the RMA controller is in Appendix E. SIMULINK used the state space equations of the truss and the RMA to evaluate the differential equations of the system and retrieve the twelve states for feedback to the full-state feedback gain matrix ( $K$ ). Just as in all previous simulations, a sinusoidal function, at the resonant natural frequencies of the first four modes of the truss, was the input signal to the tip AJTs to excite the truss model to its bending modes. The excitation signal was processed through a switch which controlled the length of time that the truss was excited before the controllers were activated. The excitation time was adjusted to closely match the magnitude of the acceleration signals of the full-state feedback simulation to the magnitude of the acceleration signals from open loop simulation. Although the tip AJTs were used to excite the truss to its different modes, the RMA control signals were used to dampen the vibrations in this configuration. A saturation block was added to the control inputs loop of each of the RMAs, tip and midpoint, to impose upper and lower bounds on the signals. The saturation blocks were used to limit the control force applied by the simulated RMAs to more closely match the experimental models. Without the saturation blocks, the simulated control forces of the RMAs were capable of controlling the large displacements created by the first mode of the truss. Experimental results of the classically designed, negative relative velocity feedback controllers for the RMAs, discussed in Sections 3.4 and 4.6, demonstrated the inability of the RMAs alone to control the first mode vibrations of the truss. Another method of limiting the control inputs would be to increase the penalties in the control input weighting matrix ( $R$ ).

Figures 5.1 and 5.2 are plots of the tip and midpoint acceleration signals for the first four modes of the truss in a closed loop model implementing the full-state feedback RMA control law. The plot of the first mode displays large acceleration spikes as the truss dampens to equilibrium. The smaller oscillations about these larger spikes are the acceleration forces generated by the RMA control forces attempting to dampen vibrational displacements beyond the capabilities of the control forces of the RMAs. The final large burst of acceleration signals, at approximately 4 seconds on

Table 5.1: Full-State Feedback RMA Controller: Approximate Simulation Settling Times in Seconds

Mode	S. Time (O.L.)	S. Time (Analog)	S. Time (Full-State)
1	40	20	5
2	12	2	0.75
3	3	1.5	0.50
4	2	1	0.30

the plot, may be due to an actuator/instrument instability in the model of the RMAs due to the large feedback gains related to this mode and the saturation limits on the control inputs. It should be recalled that the classically design RMA controllers were unable to control the first mode of the truss with settling times of approximately 20 seconds. The full-state feedback RMA control law simulation dampens the first mode vibrations with a settling time of 5 seconds, even with the unstable acceleration. The second, third, and fourth modes of the truss are within the control force capabilities of the RMAs and the full-state feedback RMA controller simulations demonstrate the expected performance of the controller to dampen these higher frequency modes. Table 5.1 shows approximate simulated settling times (S. Time) of the open loop model, without RMAs, the classical analog RMA controller, and the full-state feedback RMA controller. The settling times of all of the modes are decreased dramatically, demonstrating the expected increase in performance capabilities of the optimal, LQR, full-state feedback controller.

#### 5.4 Non-Linear Simulation of a Hybrid (Classical AJT and Full-State RMA) Controller

SIMULINK [14] was used to simulate the truss, the classical AJT controller, and the full-state feedback control law for hybrid vibration suppression. A block diagram of the SIMULINK closed loop system for the hybrid (classical AJT and full-state RMA) controller is in Appendix E. SIMULINK used the state space equations of the truss, the AJTs, and the RMAs to evaluate the differential equations of the system. It is

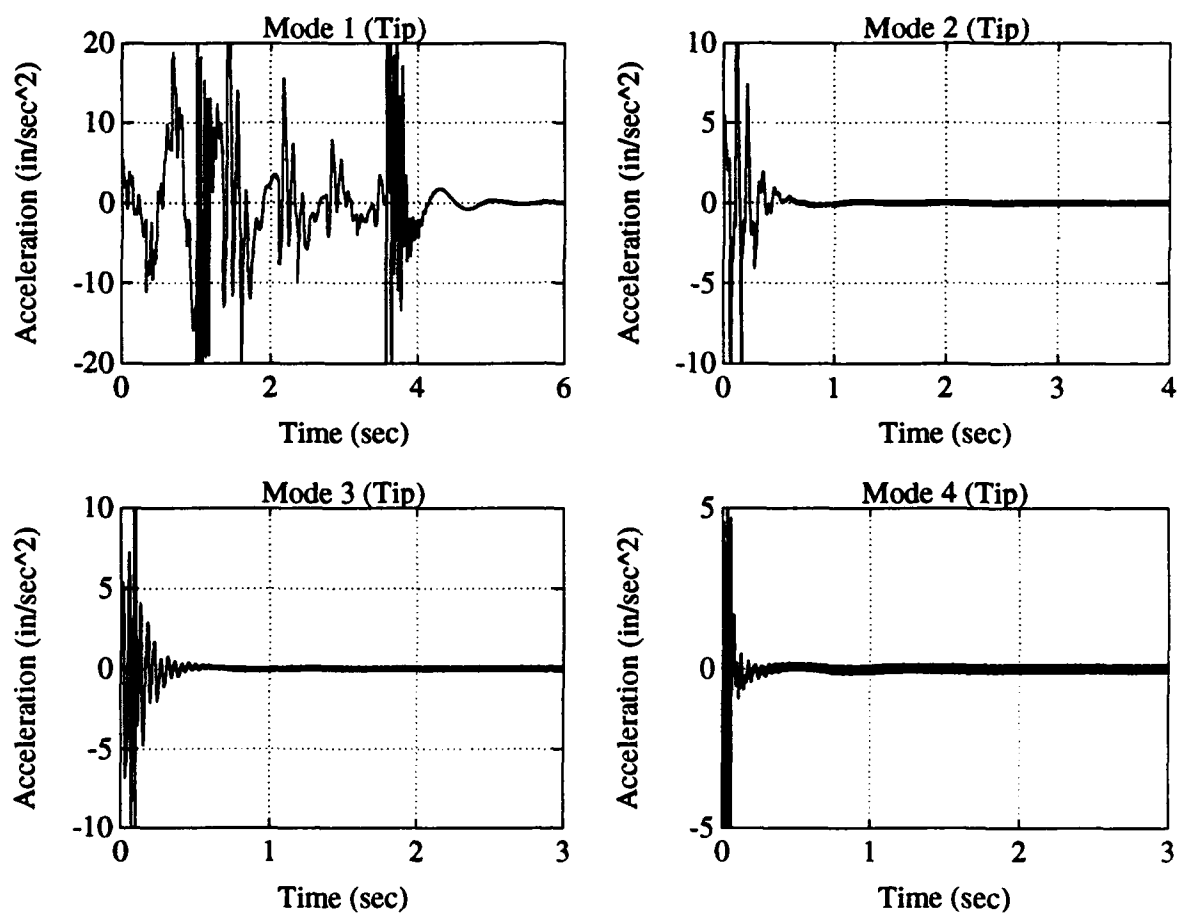


Figure 5.1: Simulation of Full-State Feedback to the RMAs

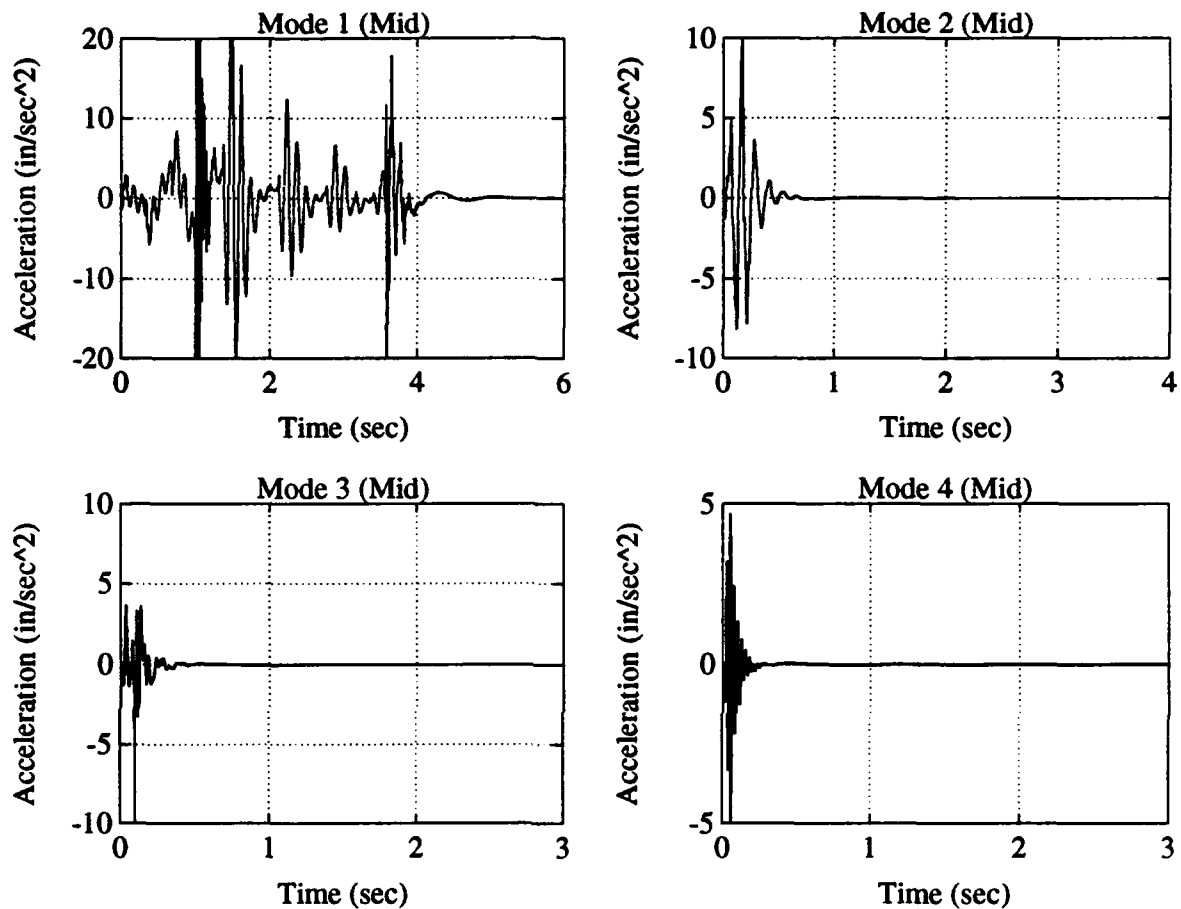


Figure 5.2: Simulation of Full-State Feedback to the RMAs

expected that the hybrid controller will improve the performance of vibration suppression of the truss over the performance simulated for the independent full-state RMA controller.

Again, a sinusoidal function, at the resonant natural frequencies of the first four modes of the truss, was the input signal to the tip AJTs to excite the truss model to its bending modes. The excitation signal was processed through a switch which controlled the length of time that the truss was excited before the controllers were activated. The excitation time was adjusted to closely match the magnitude of the acceleration signals of the full-state feedback simulation to the magnitude of the acceleration signals from open loop simulation. A combination of the classical AJT and

Table 5.2: Hybrid LQR Controller: Approximate Simulation Settling Times in Seconds

Mode	S. Time (O.L.)	S. Time (Analog)	S. Time (Hybrid)
1	40	4	4
2	12	2	0.75
3	3	2	0.5
4	2	1	0.3

full-state RMA control signals were used to dampen the vibrations in this configuration. The AJT controller in simulation is the same as designed for analog control in Section 3.3. The RMA full-state feedback controller is the one previously described in Section 5.4. No design effort was made to couple the two controllers.

Figures 5.3 and 5.4 are plots of the tip and midpoint acceleration signals for the first four modes of the truss in a closed loop model implementing the hybrid control law. The plot of the first mode displays large acceleration spikes as the truss dampens to equilibrium. The smaller oscillations about these larger spikes are the acceleration forces generated by the RMA control forces attempting to dampen vibrational displacements beyond the capabilities of the control forces of the RMAs. The excitations between 4 and 6 seconds in the first mode simulation were caused by the AJT model firing, as was explained in Section 3.3. The hybrid (classical AJT and full-state RMA) control law simulation dampens dampens the vibration of all of the modes of the truss in a very efficient manner and demonstrates the expected performance of the experimental implementation of the controller. Table 5.2 shows approximate simulated settling times (S. Time) of the open loop model, without RMAs, the classical analog hybrid controller, and the hybrid controller. The settling times of all of the modes are decreased, demonstrating the expected increase in performance capabilities of the optimal, LQR, full-state feedback controller.

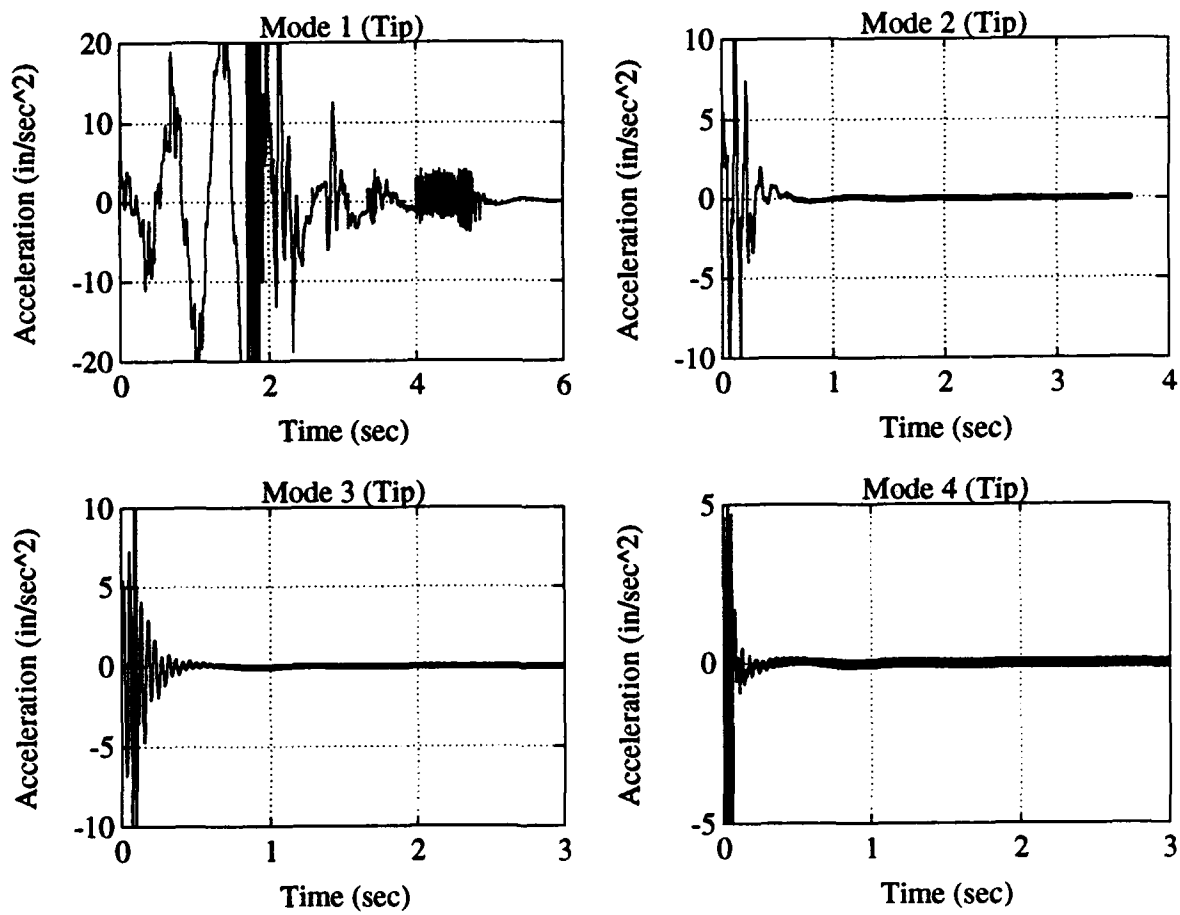


Figure 5.3: Simulation of Hybrid Controller (Classical AJT and Full-State RMA)

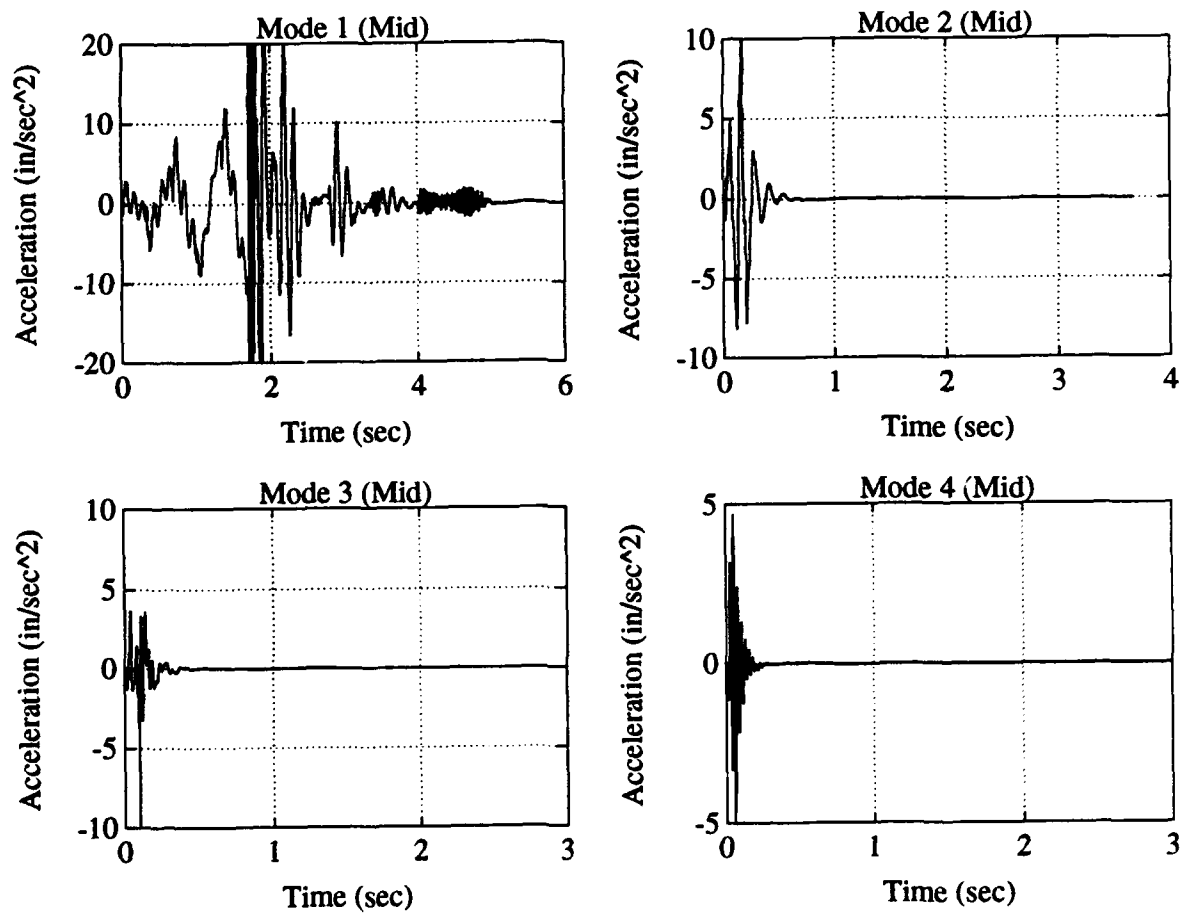


Figure 5.4: Simulation of Hybrid Controller (Classical AJT and Full-State RMA)

## Chapter 6

# CONCLUSION AND RECOMMENDATIONS

### 6.1 Overview

Model characterization and control of the UWCSL truss are reported in this thesis. The results of simulation and experimental implementation of the classical and modern control laws designed to dampen the first four bending modes of the UWCSL truss are summarized in this chapter. Recommendations for future research on the UWCSL truss are also suggested.

### 6.2 Conclusions

Two finite element models of the truss were developed using the MAPMODES [6] finite element code, one with reaction mass actuators and one without reaction mass actuators. The truss models were augmented with models of the air jet thrusters (AJTs) and/or reaction mass actuators (RMAs). Modal truncation was applied to reduce the truss models from 63 degrees of freedom to 4 and 6 degrees of freedom models respectively. Modal damping of the truss was approximated for the first four lateral vibrational modes with experimentally determined viscous damping coefficients for each mode. The two reduced order models, without RMAs and with RMAs, were simulated in open loop configurations using SIMULINK, non-linear simulation software [14]. Experimental procedures were used to validate the simulation models.

Classical control laws were designed for negative velocity feedback to the air jet thrusters and reaction mass actuators, both independently and in a hybrid configuration, to actively dampen the vibrations. Two independent controllers were designed for the different sensor and actuator configurations of the UWCSL truss. One controller was for AJT actuation and the other for RMA actuation with relative negative

velocity feedback. A third controller, the hybrid controller, was created by combining the two independent controllers.

Simulations of the closed loop truss/controller models were used to predict the response of the truss to both continuous-time and discrete-time or digital controllers. The digital control laws were developed by applying Tustin's method of emulation to the continuous controllers, with a 10 millisecond sampling period. The simulated tip acceleration plots for the first four modes of the truss were evaluated for their respective settling times. The settling times of each of the controllers were evaluated to determine the performance of the control law.

The control laws were experimentally implemented through analog and digital computers and the results were used to verify the simulation. Good agreement between the simulation and experimental results was observed. The experimental plots of the tip and midpoint accelerations were evaluated for their settling times and damping ratios. The damping ratios were calculated using the logarithmic decrement method and were used as another tool for evaluating the performance of the controllers. The AJT controllers were effective in controlling the first and second mode disturbances of the UWCSL truss while the RMA controllers were effective in controlling the second and third modes of the truss. As expected, the hybrid controller out performed the individual AJT and RMA controllers and was the most effective method of vibration suppression. The digital controllers' performance was similar to the analog controllers', as was predicted in simulation. The digital AJT and RMA controllers closely matched the analog AJT and RMA controllers in both their settling times and damping ratios.

An initial Linear Quadratic Regulator (LQR) design was formulated to optimize the performance of the RMAs utilizing full-state feedback. The LQ design for the RMAs was simulated both independently and in conjunction with the AJT controller. The performance of the simulated hybrid (LQ RMA and classical AJT) controller was better than the classical controllers.

### 6.3 Recommendations for Future Research

Recommendations for future research based on both the hardware implementation and the computer simulation are suggested in this section. The existing truss, actua-

tors, sensors, and models should serve as a foundation for further research in classical, modern, continuous, and digital control law designs. Further studies into the optimal control problem for the RMAs and for the non-linear AJTs can be accomplished on the truss and its models. Additional work can be done with the initial LQ, full-state feedback, design presented in Chapter 5. Further studies in the simulation and experimental implementation should be done. The LQG, state-estimator design, SANDY, and  $H_2/H_{inf}$  design approaches all need to be explored in both simulation and experimental application. The implementation of a digital computer as the controller in this thesis has increased the facility of implementing these and other control laws on the UWCSL truss. Numerous control laws can be quickly and accurately implemented to dampen the vibrations of the different modes of the truss through the use of LABVIEW [11].

The next step in future research should be the implementation of the digital hybrid controller discussed in this thesis into LABVIEW. This can be accomplished through the use of an input/output (I/O) board with at least four input and four output channels. The experimental results of the digital hybrid controller should match the predicted performance of the simulation accomplished in Chapter 4. Once the digital hybrid controller results are obtained and the simulation validated, the gate to the experimental digital control realm is wide open. Direct digital design of controllers for vibration suppression of the UWCSL truss, classical and modern, can be simulated and implemented to improve the current performance. The study of the effects of different sampling periods on the performance of the digital controllers can be examined along with the consequences of multiple or variable sampling periods.

The truss hardware is configured to allow for the incorporation of active truss members with piezoelectric sensors and actuators. The Boeing Co. has provided the UWCSL with some of these members for further study and research applications. The piezo members are the same length as the diagonal members of the truss and their implementation would require no changes to the current truss configuration, except for the addition of mass and the change in stiffness of the members. The piezoelectric members could also be attached to the hub, or fixed end, of the truss and used to excite vibrations in the structure with minimal changes to the experimental configuration. The piezo members will act as collocated force and vibration sensors and provide more control actuation for the truss.

The addition of sensors and actuators, piezoelectric or other types, forces the question of determining the optimal position for controlling the different modes. A study of optimal sensor and actuator locations on the flexible structure should be accomplished rather than relying on the existing tip and midpoint positions.

Additional sensors and actuators will change the physical configuration of the truss. The models of the truss should be updated to incorporate the changes to the structure. Even without these changes, the truss is an ideal testbed for designing and validating other finite element method codes. Alternative finite element methods (FEM) may better represent the flexible structure or facilitate changes to the model of the structure if the sensor/actuator configuration is changed or the structure itself is altered. The FEMs could also incorporate the effects of the non-linear joints of the truss structure and more accurately incorporate the modeling of the viscous and Coulomb damping terms. Other methods of model reduction can be examined to determine the best low-order model of the truss for control purposes. The FEM code models could be validated using the experimental procedures discussed in Chapter 2 and described in Appendix D.

The availability of structural members incorporating piezoceramic elements allows for the investigation of hybrid actuation wherein the piezos may be used in conjunction with the RMAs or the AJTs. For such hybrid actuation, the question of optimal placement of the sensors and actuators as well as the number and order of the controllers arises. Due to the cost of hardware and the increased complexity associated with such control strategies, the question of the minimum number of actuators and sensors required to obtain performance specifications also surfaces. As evident from discussions on hardware limitations (e.g I/O board channels), the implementation of high order controllers is not a viable option. Thus, the design and validation of reduced order controllers to approximate the performance of high order controllers (e.g. full-state feedback) needs to be investigated. It is readily apparent that a multitude of theoretical and experimental research in structures and controls can be accomplished using the UWCSL truss.

## BIBLIOGRAPHY

- [1] Adams, R.J. Controller Design for a Laser Steering Mirror on a Flexible Structure. M.S.A.A. thesis, University of Washington, 1990.
- [2] Barker, K.J. Toward the Robust Control of High Bandwidth High Precision Flexible Optical Systems. Ph D thesis, University of Washington, 1991.
- [3] Brogan, William L. *Modern Control Theory*. Prentice-Hall, Inc., Englewood Cliffs, NJ. 1991.
- [4] Franklin, G.F., Powell, J.D., and Workman, M.L. *Digital Control of Dynamic Systems*. Addison-Wesley Publishing Co., Menlow Park, CA. 1990.
- [5] Fuller, D.C., Shepherd, M.J. and Zeigler, M.L. Parametric Study of Passively Damped Diagonals in a Large Space Structure, Flight Dynamics Laboratory, Wright Research and Development Center, WPAFB, OH, WRDC-TM-89-192-FIBG, September 1989.
- [6] Hallauer, W.L. Jr. *MAPMODES User's Guide*. Private Publication, 2 February 1989.
- [7] Hallauer, W.L. Jr. and Lamberson, S.E. Experimental Active Vibration Damping of a Plane Truss Using Hybrid Actuation. AIAA Paper 89-1169, *30th Structures, Structural Dynamics and Materials Conference, Mobile, AL*, April 3-5, 1989.
- [8] Hallauer, W.L. Jr. and Lamberson, S.E. A Laboratory Planar Truss for Structural Dynamics Testing. Unpublished Paper, 1989.
- [9] Hughes. R.O. Conceptual Design of Pointing Control Systems for Space Station Gimballed Payloads. AIAA Paper 86-1986, August, 1986.

- [10] Inman, D. J. Control/Structure Interaction: Effects of Actuator Dynamics. *Mechanics and Control of Large Flexible Structures*. ed Junkins, J.L., AIAA Inc, vol 129, 1990.
- [11] LABVIEW 2. National Instruments Corporation. Austin, Texas. October 1990.
- [12] Ly, U.L. Lecture Notes AA 518. Spring 1992. University of Washington, Seattle.
- [13] Maciejowski, J.M. *Multivariable Feedback Design*. Addison-Wesley Publishing Co., Wokingham, England. 1989.
- [14] MATLAB/SIMULINK version 3.5f. MathWorks, Inc. Natick, Massachusetts. 9 June 92.
- [15] Meirovitch, L. *Analytical Methods in Vibrations*. Macmillan Publishing Co., Inc. New York. 1967.
- [16] Miller, D.W. and Crawley, E.F. Theoretical and Experimental Investigation of Space-Realizable Inertial Actuation for Passive and Active Structural Control. *Journal of Guidance, Control, and Dynamics*. Vol.33, No.5, Sept.-Oct.1988, pp 449-457.
- [17] Ogata, K. *System Dynamics*. Prentice-Hall, Inc., Englewood Cliffs, N.J. 1978.
- [18] Sage, Andrew P. and White, Chelsea C. *Optimum Systems Control*. Prentice-Hall, Inc., Englewood Cliffs, N.J. 1977.
- [19] Schulthess, M.R. Studies in Dynamic Characterization and Control of a Flexible Structure and Optical Beampath. M.S.A.A. thesis, University of Washington. 1991.
- [20] Shepherd, M.J. Studies in Control for Vibration Suppression of the UWAA 20-Bay Planar Truss M.S.A.A. thesis, University of Washington, 1991.
- [21] Thompson, W.T. *Theory of Vibration with Applications*. Prentice-Hall, Inc., Englewood Cliffs, N.J. 1988.

- [22] Unix Matlab/Simulink Work Files. University of Washington Computer Account, controls@aa.washington.edu. 1992.
- [23] Zimmerman, D.C., Horner, G.C., and Inman, D.J. Microprocessor Controlled Force Actuator, *Journal of Guidance, Control, and Dynamics* Vol.11, No 3, May-June 1988, pp. 230-236.

## Appendix A

### AJT CONTROL CIRCUITRY

This appendix is an excerpt from Lt. Marcus Schulthess' M.S.A.A. thesis [19]. It describes the electronic circuits which run and control the air jets thrusters. The circuitry was built on a circuit board using capacitors, resistors, operational amplifiers (OP-AMPS) and other integrated circuit elements. Figures A.2 and A.3 show the circuit diagram from the servo accelerometer to the analog input and from the computer output all the way to the solenoid. The rationale for the use of these circuits is discussed in this appendix.

The sensitivity and range of the servo accelerometer output is determined by selecting the proper resistor to place between the signal pin and ground. The value of the resistor was determined from the following equation

$$\frac{\left[ \frac{V_E - V_I}{g_{max}} \right]}{C.S.F.} = \Omega_r \quad (A.1)$$

where  $V_E$  is the excitation voltage, nominally at  $\pm 15$  volts,  $V_I$  is the internal voltage, approximately 2.5 volts, and  $C.S.F.$  is the current scale factor of the accelerometer, 1.3 milliamps per  $g$ . The choice of required resistor  $\Omega_r$  is based upon the maximum number of  $g$ 's expected and output sensitivity desired of the accelerometer. Since the accelerometer maximum output is  $\pm 15$  volts and the analog computer is linear only from zero to  $\pm 10$  volts, the resistor chosen must slightly overestimate the maximum number of  $g$ 's expected. After trying various resistors and examining accelerometer output for each modal frequency at the tip and midpoint truss stations, a  $30k\Omega$  resistor was chosen. This corresponds to a maximum of 0.35 $g$  and a sensitivity of 38.8 volts per  $g$ .

Figure A.3 shows the electronic circuitry after the analog implemented controller. A three way switch is included in the circuit to give an operator functional control of the AJTs. When the switch is in the *Source* position, a signal generator is connected to the input of the tip AJT controller circuit, allowing the tip mounted AJT to excite

the truss structure. The midpoint AJT is grounded. When the switch is in the *Off* position both AJT pairs are disabled allowing the truss structure to vibrate freely without any excitation or active control. When the switch is in the *control* position both AJTs are connected with their respective control circuits and are enabled as active dampers.

The velocity feedback controller was designed using an approximate integrator to insure that when the control loop is closed, a DC signal would not ruin the feedback properties of the controller. However, when the switch is in either the *Source* or *Off* position the analog computer circuit is disabled and stray DC voltages will cause problems for the air jet thrusters because the high gain 741N OP-AMPS will amplify the signal and cause one air jet thruster to switch on inadvertently. To eliminate this problem a lead network or differentiating circuit is implemented immediately following the switch.

A transfer function for the lead filter is easily obtained by solving the circuit diagram shown in Figure A.1.

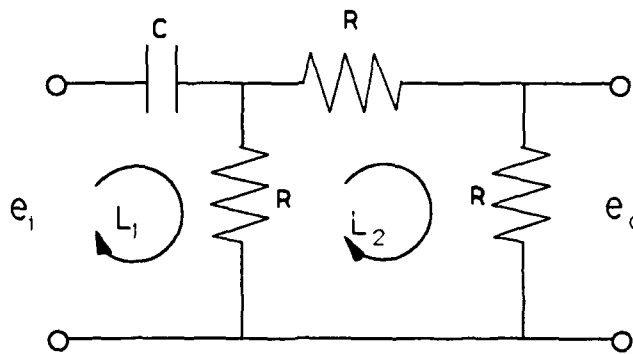


Figure A.1: Lead Network Circuit Diagram

Using Kirchoff's voltage law around loops  $L_1$  and  $L_2$  we obtain equations for the input and output potential voltages

$$e_i = \frac{1}{C} \int i_1 dt + R(i_1 - i_2) \quad (\text{A.2})$$

$$-e_o = R(i_2 - i_1) + Ri_2 = -Ri_2 \quad (\text{A.3})$$

where  $i_1$  and  $i_2$  are the currents flowing around loops  $L_1$  and  $L_2$  respectively. Taking the Laplace transforms of Equations A.2 and A.3 we obtain

$$\begin{aligned} E_i(s) &= \frac{1}{Cs}I_1(s) + R(I_1(s) - I_2(s)) \\ E_o(s) &= R(I_2(s) - I_1(s)) + RI_2(s) = -I_2(s) \end{aligned} \quad (\text{A.4})$$

Solving for the currents  $I_1(s)$  and  $I_2(s)$  in terms of the other variable we have

$$I_1(s) = \frac{E_o(s)}{R} \quad I_2(s) = \frac{3e_o(s)}{R} \quad (\text{A.5})$$

By substituting Equation A.5 back into Equation A.4 while examining the transfer function of output voltage to input voltage ( $\frac{E_o(s)}{E_i(s)}$ ) the simplified transfer function is

$$\frac{E_o(s)}{E_i(s)} = \frac{RCs}{3 + 2RCs} \quad (\text{A.6})$$

The values of the resistance and capacitance were chosen so that the lead filter would have little effect on the frequencies at or above the first lateral vibrational mode of the truss. The first lateral mode of the truss is at 1.48 Hz corresponding to 9.3 radians per second. Based on these criteria the values of  $R$  and  $C$  were chosen to be  $1 \text{ M}\Omega$  and  $1 \mu\text{f}$  respectively. Substituting in these values reduces the transfer function to

$$\frac{E_o(s)}{E_i(s)} = \frac{0.5s}{s + 1.5} \quad (\text{A.7})$$

The control signal is reduced by half as the magnitude reaches its steady state value at 1 Hz. This gain reduction would be unacceptable for most linear controllers. The non-linear behavior of the AJT makes the output force independent of control signal magnitude as long as a dead zone is overcome. The dead zone is implemented keeping in mind the control magnitude reduction effects of the lead filter. An added benefit of the filter is a small phase lead at the first modal frequency which can improve control characteristics by reducing the lag time of the AJT in developing full force output.

Two 741N OP-AMPS were used in the AJT circuit. The AJTs are wired to provide bi-polar excitation and control of the planar truss. The circuit is set up so that one air-jet fires for a positive control voltage while the other fires for a negative voltage.

A small dead zone is designed into the circuit as a necessary control element. The dead zone is implemented using the 741N OP-AMPS. Each operational amplifier is offset with a positive or negative voltage, corresponding to the positive or negative air-jet, that must be overcome by the control signal in order to cause the transistor to fire, thus opening the solenoid valve and turning on the force. A  $10\text{ M}\Omega$  and  $3\text{ k}\Omega$  resistor are used along with a  $\pm 15$  volt input to produce a  $\pm 9\text{ mV}$  dead zone when combined with the control magnitude reduction effect of the lead filter.

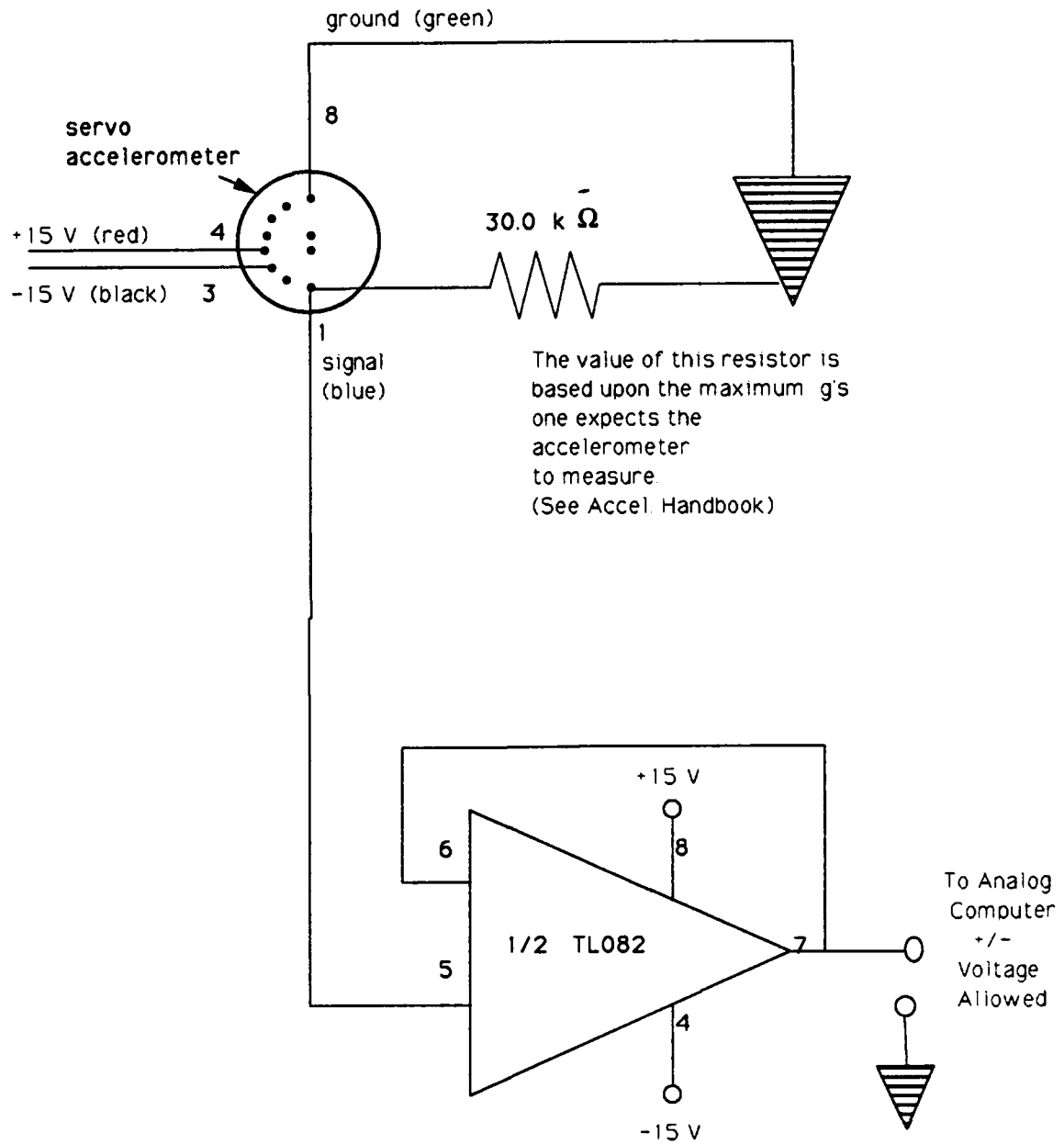


Figure A.2: Accelerometer Circuit



## Appendix B

### STATE SPACE MATRICES

The A and B state space matrices for the 8th order UWCSL truss model, without RMAs, from MAPMODES:

$A_8 =$

Columns 1-4

$$\begin{bmatrix} -1.8466 & 3.5562 & -2.3076 & 0.60449 \\ 1.2936 & -3.4306 & 2.5867 & -0.68079 \\ -0.54866 & 2.3138 & 3.7569 & 2.2882 \\ 0.019085 & -0.59067 & 2.3303 & -4.0724 \\ 1 & 0 & 0 & 0 \\ 0 & 1 & 0 & 0 \\ 0 & 0 & 1 & 0 \\ 0 & 0 & 0 & 1 \end{bmatrix}$$

Columns 5-8

$$\begin{bmatrix} -11,358 & 27,361 & -22,563 & 9,095.9 \\ 9,551.3 & -25,162 & 22,364 & -9,693.1 \\ -5,689.0 & 20,316 & -28,721 & 20,166 \\ 1,408.8 & -8,189.2 & 20,306 & -27,067 \\ 0 & 0 & 0 & 0 \\ 0 & 0 & 0 & 0 \\ 0 & 0 & 0 & 0 \\ 0 & 0 & 0 & 0 \end{bmatrix}$$

$B_8 =$ 

$$\begin{bmatrix} 15.207 & 0.75580 \\ -2.0949 & -0.18716 \\ 0.75580 & 6.3577 \\ -0.29383 & 0.048950 \\ 0 & 0 \\ 0 & 0 \\ 0 & 0 \\ 0 & 0 \end{bmatrix}$$

The A and B state space matrices for the 12th order UWCSL truss model, with RMAs, from MAPMODES:

 $A_{12} =$ 

Columns 1-6

$$\begin{bmatrix} -1.8466 & 3.5562 & -2.3076 & 0.60449 & 0.91244 & 0.049127 \\ 1.2936 & -3.4306 & 2.5867 & -0.68079 & -0.12569 & -0.012165 \\ -0.54866 & 2.3138 & 3.7569 & 2.2882 & 0.045348 & 0.41325 \\ 0.019085 & -0.59067 & 2.3303 & -4.0724 & -0.017630 & 0.0031818 \\ 1.8466 & -3.5562 & 2.3076 & -0.60449 & -7.0818 & -0.049127 \\ 0.54866 & -2.3138 & 3.7569 & -2.2882 & -0.045348 & -7.0832 \\ 1 & 0 & 0 & 0 & 0 & 0 \\ 0 & 1 & 0 & 0 & 0 & 0 \\ 0 & 0 & 1 & 0 & 0 & 0 \\ 0 & 0 & 0 & 1 & 0 & 0 \\ 0 & 0 & 0 & 0 & 1 & 0 \\ 0 & 0 & 0 & 0 & 0 & 1 \end{bmatrix}$$



## Appendix C

### EULER-BERNOULLI BEAM THEORY

The finite element model (FEM) of the cantilever (fixed-free) flexible structure is initially validated theoretically by Euler-Bernoulli beam theory. The beam theory provides a method for determining the upper bounds on the natural frequencies of the truss and an estimate of the first four bending mode shapes [19]. The purpose of this Appendix is to develop the lateral vibrational natural frequencies and mode shapes using the beam theory. A more detailed derivation of the Euler-Bernoulli beam theory can be found in most advanced structural vibration texts [15].

A simple cantilever Euler-Bernoulli beam is shown in Figure C.1. The partial

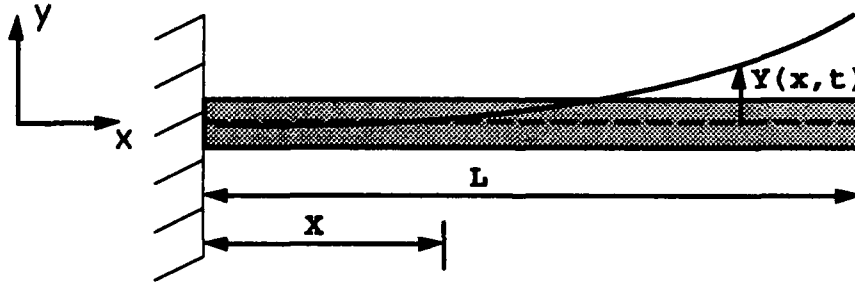


Figure C.1: Cantilever Beam Schematic

differential equation of motion which describes the cantilever beam in free vibration is

$$\frac{\partial^2}{\partial x^2} [EI \frac{\partial^2 y(x, t)}{\partial x^2}] = -m(x) \frac{\partial^2 y(x, t)}{\partial t^2} \quad (C.1)$$

where  $E$  is the Young's modulus,  $I$  the area moment of inertia,  $EI$  the bending stiffness,  $m$  the mass per unit length, and  $y(x, t)$  the transverse displacement of the beam. Young's modulus, the area moment of inertia, and mass per unit length are constant for a uniform beam. The equation is based on the assumptions that the beam is

homogeneous, undergoes small deflections, has a uniform cross-section which is small when compared to its length (slender), and both shear deformation and rotary inertia effects are neglected [15]. The solution of Equation C.1 requires the knowledge of the boundary conditions and the initial conditions which are zero displacement, zero slope, zero moment, and zero shear force. The conditions are listed below, where the fixed end is at  $x = 0$  and the free end is at  $x = L$ .

$$\begin{cases} Y(0, t) = 0 \\ Y'(0, t) = 0 \\ Y(L, t) = 0 \\ Y'(L, t) = 0 \end{cases} \quad (\text{C.2})$$

Assume that the solution of Equation C.1 is separable in time and space and of the form

$$y(x, t) = Y(x)q(t). \quad (\text{C.3})$$

Substituting Equation C.3 in Equation C.1 and dividing through by  $mY(x)q(t)$  results in the following equation:

$$\frac{1}{mY(x)} \frac{\partial^2}{\partial x^2} \left[ EI \frac{\partial^2 Y(x)}{\partial x^2} \right] = -\frac{1}{q(t)} \frac{\partial^2 q(t)}{\partial t^2} \quad (\text{C.4})$$

The left-hand side of Equation C.4 depends only on  $x$  while the right-hand side is purely a function of  $t$ . Because both  $x$  and  $t$  are independent variables, Equation C.4 has a solution only if both sides are constant. Setting each side of Equation C.4 equal to  $\omega^2$ , a constant value, and rearranging the terms leads to two ordinary differential equations (ODEs) [15]:

$$\frac{\partial^2}{\partial x^2} \left[ EI \frac{\partial^2 Y(x)}{\partial x^2} \right] - \omega^2 mY(x) = 0 \quad (\text{C.5})$$

$$\frac{\partial^2 q(t)}{\partial t^2} + \omega^2 q(t) = 0 \quad (\text{C.6})$$

The equation can be symbolically simplified introducing a new variable:

$$\beta^4 = \frac{\omega^2 m}{EI}. \quad (\text{C.7})$$

Equation C.5 describes the mode shapes of the cantilever beam and can be rewritten as

$$\frac{\partial^4 Y(x)}{\partial x^4} - \beta^4 Y(x) = 0 \quad (\text{C.8})$$

Equation C.6 defines the natural frequency of the beam. Equation C.8 is a fourth order homogeneous ODE which must be supplemented by the four boundary conditions. The problem of determining the values of  $\omega^2$  for which an equation, of the type in Equation C.8, has a nontrivial solution which satisfies the boundary conditions, is called an eigenvalue problem [15].  $\omega^2$  is the eigenvalue of the nontrivial solution,  $Y(x)$ , is the eigenvector. The four boundary conditions determine the shape of the solution but leave the amplitude arbitrary. The solution of Equation C.8 is of the form:

$$Y(x) = C_1 \cos(\beta x) + C_2 \sin(\beta x) + C_3 \cosh(\beta x) + C_4 \sinh(\beta x) \quad (\text{C.9})$$

This solution must satisfy the boundary conditions stated in Equation C.2. Replacing  $Y(x, t)$  and its derivatives in the boundary condition equations, Equation C.2, leads to the following matrix equation:

$$\begin{bmatrix} 1 & 0 & 1 & 0 \\ 0 & \beta & 0 & \beta \\ -\beta^2 \cos(\beta L) & -\beta^2 \sin(\beta L) & \beta^2 \cosh(\beta L) & -\beta^2 \sinh(\beta L) \\ \beta^3 \sin(\beta L) & -\beta^3 \cos(\beta L) & \beta^3 \sinh(\beta L) & \beta^3 \cosh(\beta L) \end{bmatrix} \begin{bmatrix} C_1 \\ C_2 \\ C_3 \\ C_4 \end{bmatrix} = \begin{bmatrix} 0 \\ 0 \\ 0 \\ 0 \end{bmatrix} \quad (\text{C.10})$$

The determinant of Equation C.10 must be zero in order for nontrivial solutions to exist. Setting the determinant of the matrix equal to zero yields:

$$\cos(\beta L) = -\frac{1}{\cosh(\beta L)} \quad (\text{C.11})$$

Plotting the functions on each side of Equation C.11 versus  $\beta L$  results in two infinite curves with an infinite number of intersections, each intersection corresponding to a solution of the equation. Solution of the transcendental equation, Equation C.11, for the first three intersections results in  $\beta L = 1.875, 4.694, 7.855$ . Each solution

of  $\beta_r L$  will result in a shape function  $Y_r(x)$  for the  $r^{th}$  normal bending mode, from Equation C.9:

$$Y_r(x) = A_r [(\sin(\beta_r L) - \sinh(\beta_r L))(\sin(\beta_r x) - \sinh(\beta_r x)) + (\cos(\beta_r L) + \cosh(\beta_r L))(\cos(\beta_r x) - \cosh(\beta_r x))] \quad (C.12)$$

$A_r$  is used to normalize the mode shape at a particular location on the cantilever beam. Superposition is used to determine the transverse displacement  $y(x, t) = Y(x)q(t)$ . Each normal mode function ( $Y_r(x)$ ) multiplied by the time function ( $q_r(t)$ ) is a solution of the cantilever beam equation. The total response ( $y(x, t)$ ) is the sum of all of the normal mode responses. Equation C.12 describes the mode shape function ( $Y_r(x)$ ) for the  $r^{th}$  mode. The time function ( $q_r(t)$ ) corresponding to the  $r^{th}$  mode must satisfy Equation C.6 where the natural frequency ( $\omega_r$ ) is given by

$$\omega_r = \beta_r^2 \sqrt{\frac{EI}{m}} = (\beta_r L)^2 \sqrt{\frac{EI}{mL^4}} \quad (C.13)$$

The solution of ( $q_r(t)$ ) can be solved completely if the initial conditions ( $q_r(0)$  and  $\dot{q}_r(0)$ ) are specified.

The truss is 278 inches long and weighs 239 pounds, which makes  $m(x) = 2.237 \times 10^{-3} \frac{(lb_f - s^2)}{in^2}$ . The problem of predicting the natural frequencies and mode shapes is simply determining the bending stiffness  $EI(x)$  of the structure. The bending stiffness of the truss members was experimentally determined by Hallauer for the Air Force Academy truss to be  $EI(x) = 1 \times 10^8 lb_f - in^2$  [7]. The first four lateral Euler-Bernoulli beam theoretical natural frequencies are shown in Table 2.3 and the normalized mode shapes in Figure 2.11.

## Appendix D

# OPERATING INSTRUCTIONS AND EXPERIMENTS FOR THE UWCSL TRUSS

### *D.1 Operating Instructions*

1. Remove the steel bars holding the truss stationary (one on each side of the truss).
2. Open the compressed air valve near the Lab's door.
- 3 Adjust the regulator until the desired pressure is shown by the needle. (65 Psi unless otherwise specified) NOTE: Set the regulator and don't adjust it throughout the experimentation process.
4. Turn on the 12 Volt and 15 Volt Power Supplies mounted under the truss near the control panel. NOTE: The lights will be illuminated when the power is on.

IF RMA's are to be used:

Turn on the two black amplifiers mounted under the truss. The power is turned on by turning the gain dial to the desired gain setting (see Chapter 3, Table 3.3). An illuminated green light indicates the power is on. The red reset light indicates the need for the reset button to be pressed. NOTE: The reset button must be pressed after the initial power up.

IF Analog Computers are to be used:

Turn on the power switch. The computer's lights will flicker and fans can be heard. Move the black 3-position switch to "RESET" and then back to "OPER."

5. Connect the front panel to the desired controller or signal source and/or truss accelerometer signals. (See specific experiment set-up instructions.)
6. To use signals from the Dynamic Signal Analyzer or other source to excite the truss through the tip AJTs, throw the toggle switch on the control panel to the "SIGNAL" position. To use control signals to either the AJTs or the RMAs (Tip or Mid),

throw the toggle switch on the control panel to the "CONTROL" position. To stop all signals into the truss, toggle the switch to the "OFF" position.

**NOTE:**

- a. After long periods with out use, the steel ball bearings and metal plates, on which they sit, should be wiped clean for better results.
- b. Before initial use, ensure that no air is leaking from any of the tubes or the joints into the AJTs.

## *D.2 Experiments*

### *D.2.1 Open Loop: Swept Sine Resonant Frequency Determination*

Objective: The purpose of this experiment is to obtain the resonant natural frequencies of the open loop UWCSL Truss through the use of the swept sine function of an HP Dynamic Signal Analyzer. The result of this procedure is a Bode Plot of the input signal to the tip acceleration of the truss which can be used to determine the resonant frequencies of the truss as well as its open loop transfer function.

Equipment: UWCSL Truss with Operating Instructions

- 1 HP 35665A Dynamic Signal Analyzer (DSA)
- 1 1 foot (short) BNC (Co-ax) Cable
- 2 3 foot (long) BNC (Co-ax) Cables
- 1 BNC T Connector

**PROCEDURE:**

Hardware Set-up:

1. Follow the UWCSL Truss Operating Instructions. DO NOT turn the truss control panel toggle switch to "Signal" until the HP Dynamic Signal Analyzer (DSA) has been configured. (SEE FIGURE D.1 TO FOLLOW SET-UP STEPS 2-5)
2. Connect the short BNC Cable to the "source" output port of the DSA. Connect the other end of this short BNC Cable to the BNC T Connector.
3. Connect 1 of the long BNC Cables to the other output of the BNC T Connector. Connect the BNC T Connector (not the cable) to the DSA "Channel 1" input port.

4. Connect the loose end of the long BNC Cable to the truss control panel port labeled: "Signal In." (Steps 3 and 4 allow the the source input to be simultaneously fed into the DSA's "Channel 1." and into the truss. The source "Signal In" will excite the 2 tip AJTs of the truss.)
5. Connect the other long BNC Cable to the "Channel 2" input port of the HP DSA. Connect the loose end of this long BNC Cable to the truss control panel port labeled: "TIP ACCEL." (This cable will carry the truss tip acceleration signal from the tip accelerometer to the DSA.)

HP DSA Set-up:

6. Turn on the power switch of the DSA. Wait until calibration is complete. Press the green "PRESET" hardkey. Then press the "Do Preset " softkey.
7. Press the "Inst Mode" hardkey and then the "Swept Sine " softkey.
8. Press the "Meas Data" hardkey and then the "Frequency Response " softkey.
9. Press the "Disp Format" hardkey and then the "Bode Diagram" softkey.
10. Press the "Trace Coord" hardkey. To shift between the two plots, press the "Active Trace" hardkey. (The active plot is the plot with the A: or B: and type in the upper left hand corner highlighted.) Use the softkeys to ensure that the upper plot is a "dB Magnitude" type and the lower plot is an "Unwrapped Phase" type. Also ensure that the "X-axis LIN/LOG" softkey has "LOG" highlighted.
11. Press the "Scale" hardkey. Press the "Y per Div (Decades)" softkey and chose an appropriate Y-axis scale. Enter a numerical value on the keypad (Y per Div =10 dB/div) and press the "Enter" softkey. Press the "Top Reference" softkey to set the top of the Y-axis scale (Top Ref = 40 dB). Do this for both plots using the "Active Trace" hardkey. The scale of the two plots should resemble the following values: Upper plot: Y per Div = 10 dB/div and Top Ref = 40 dB) Lower plot: Y per Div = 50 deg/div and Top Ref = 50 deg).
12. Press the "Freq" hardkey. Press the "Start" softkey and enter the desired start frequency (1 Hz). Press the "Span" softkey and enter the desired frequency span (51 Hz). Press the "Sweep LIN/LOG" softkey and ensure that "LOG" is highlighted. You can adjust the resolution as desired but notice the estimated sweep time in the upper right hand corner of the screen (high resolution will require a longer sweep time).
13. Press the "Source" hardkey. Press the "Level" softkey and select the desired level

(0.05 Vpk). The input signal level must be greater than the AJT's dead-band but not so large as to saturate the control circuits.

#### RUN

14. Turn the truss control panel toggle switch to "Signal."
15. Press the "START" hardkey to begin the swept sine measurement.

#### PLOT RESULTS

16. (This will screen dump the plots displayed on the screen to the laser printer.) Press the "PLOT/PRINT" hardkey. Press the "MORE SETUP" softkey. Press the "Device is Plot/Prnt" softkey and ensure that "PRNT" is highlighted. Press the "Return" softkey.
17. Press the "Start Plot/Prnt" softkey to initiate the printing.

#### *D.2.2 Open Loop: Determination of Damping Coefficients*

Objective: The purpose of this experiment is to obtain the damping coefficients of the open loop UWCSL Truss at its first four modes. The truss is excited at its natural frequencies using the fixed sine function of an HP Dynamic Signal Analyzer. (The frequencies used in this lab should come from the "Swept Sine Resonant Frequency Determination" experiment. The suggested values in the procedures come from experimentation done in AUG 92.) The results of this procedure are plots of decaying acceleration signals at each of the modal frequencies. The plots can be evaluated using different numerical methods to determine the damping coefficient at each of the modes.

Equipment: UWCSL Truss with Operating Instructions

- 1 HP 35665A Dynamic Signal Analyzer (DSA)
- 3 3 foot (long) BNC (Co-ax) Cables

#### PROCEDURE:

##### Hardware Set-up:

1. Follow the UWCSL Truss Operating Instructions. DO NOT turn the truss control

panel toggle switch to "Signal" until the HP Dynamic Signal Analyzer (DSA) has been configured. (SEE FIGURE D.2 TO FOLLOW SET-UP STEPS 2-4)

2. Connect a BNC Cable to the "source" output port of the DSA. Connect the other end of this BNC Cable to the truss control panel port labeled: "Signal In."

3. Connect 1 of the long BNC Cables to the DSA "Channel 1" input port. Connect the loose end to the truss control panel port labeled: "TIP ACCEL." (This cable will carry the truss tip acceleration signal from the tip accelerometer to the DSA.)

4. Connect the third long BNC Cables to the DSA "Channel 2" input port. Connect the loose end to the truss control panel port labeled: "MID ACCEL." (This cable will carry the truss midpoint acceleration signal from the mid accelerometer to the DSA.)

#### HP DSA Set-up:

5. Turn on the power switch of the DSA. Wait until calibration is complete. Press the green "PRESET" hardkey. Then press the "Do Preset " softkey.

6. Press the "Inst Mode" hardkey and then the "FFT Analysis " and the "2 Channel" softkeys.

7. Press the "Disp Format" hardkey and then the "Upper/Lower" softkey. (This will cause 2 plots to be displayed on the screen.) To shift between the two plots, press the "Active Trace" hardkey. (The active plot is the plot with the A: or B: and type in the upper left hand corner highlighted.)

8. Press the "Meas Data" hardkey. Make the upper plot active and press the "Time Channel 1 " softkey. Now make the lower plot active and press the "Time Channel 2" softkey. (The upper plot will display the tip acceleration signals and the lower plot will display the midpoing acceleration signals.)

9. Press the "Trace Coord" hardkey. Press the "More: NYQ REAL IMAG" softkey. Press the "REAL PART " softkey and ensure that both plots are "REAL" type. Press the "RETURN " softkey and ensure that the "X-axis LIN/LOG" softkey has "LIN" highlighted.

10. Press the "Scale" hardkey. Press the "Y per Div (Decades)" softkey and choose an appropriate Y-axis scale. Enter a numerical value on the keypad (Y per Div =1.2 V/div) and press the "Enter" softkey. Press the "Top Reference" softkey to set the top of the Y-axis scale (Top Ref = 6 V). Do this for both plots using the "Active Trace" hardkey. The scale of the two plots should resemble the following values for

the first resonant frequency (adjust these values at other frequencies): Upper plot: Y per Div = 1.2 V/div and Top Ref = 6 V) Lower plot: Y per Div = 500 mV/div and Top Ref = 2.5 V).

11. Press the "Freq" hardkey. Press the "Record Length" softkey. Enter the desired record length with the numeric keypad or with the up and down arrows next to the keypad. (The first resonant frequency should have a record length of 64 sec.)

12. Press the "Source" hardkey. Press the "Fixed Sine" softkey and enter the desired frequency (1.485 Hz). Press the "Level" softkey and select the desired level (0.05 Vpk). Press the "Source ON/OFF" softkey and ensure that "ON" is highlighted. The DSA is now sending the fixed sine signal out of the source port into the truss.

#### RUN

13. Turn the truss control panel toggle switch to "Signal" to initiate the input signal to the truss. Allow the truss to stabilize at the desired vibrating frequency (wait 10-15 seconds) before going on to the next step.

14. Press the "START" hardkey to begin recording the acceleration signals from the truss tip and midpoint. Allow the DSA to calibrate and allow the time response to be recorded for approximately 10 seconds. Throw the truss control panel toggle switch to "Off" making note of the "Time remaining" in the record length. (This stops the signal to the truss and will cause the DSA to display the acceleration signal damping of the truss.)

15. Let the truss dampen out and allow the DSA to measure the results for the entire record length. Once the record length has expired, the plot will be displayed on the screen. Press the "PAUSE/CONT" hardkey to stop the measurements.

16. Press the "MARKER" hardkey. This will now allow you to use the marker softkeys and the marker position dial to determine peak values and other points of interest on the plots. (The marker is effective only for the active plot unless marker coupling is on.)

#### PLOT RESULTS

17. (This will screen dump the plots displayed on the screen to the laser printer.) Press the "PLOT/PRINT" hardkey. Press the "MORE SETUP" softkey. Press the "Device is Plot/Prnt" softkey and ensure that 'PRNT' is highlighted. Press the "Re-

turn" softkey.

18. Press the "Start Plot/Prnt" softkey to initiate the printing.

NOTE: Temperature and other lab conditions will cause the plots to vary. Take all data in the same time period (day, hour, etc.) for consistent results.

\* You can use a number of different methods to determine the damping coefficient of the truss once the plots exist.

### *D.2.3 Open Loop: Determination of Mode Shapes*

Objective: The purpose of this experiment is to obtain the mode shapes of the open loop UWCSL Truss. The truss is excited at its natural frequencies using the fixed sine function of an HP Dynamic Signal Analyzer. The results of this procedure are plots of displacement from the Electro-Mike position sensor. By normalizing the peak values of displacement at each of the nodes of the truss, the mode shape at each frequency can be determined.

Equipment: UWCSL Truss with Operating Instructions

1 HP 35665A Dynamic Signal Analyzer (DSA)

1 10 foot (long) BNC (Co-ax) Cable

1 Electro-Mike Position Sensor, Circuit Box and Cables

#### **PROCEDURE:**

##### Hardware Set-up:

1. Follow the UWCSL Truss Operating Instructions. DO NOT turn the truss control panel toggle switch to "Signal" until the HP Dynamic Signal Analyzer (DSA) has been configured.
2. Connect the BNC Cable to the "source" output port of the DSA. Connect the other end of this BNC Cable to the truss control panel port labeled: "Signal In."
3. Connect the BNC cable out of Electro-Mike circuit box to the DSA "Channel 1" input port.

##### HP DSA Set-up:

4. Turn on the power switch of the DSA. Wait until calibration is complete. Press the green "PRESET" hardkey. Then press the "Do Preset" softkey.

5. Press the "Inst Mode" hardkey and then the "FFT Analysis " and the "1 Channel" softkeys.
6. Press the "Disp Format" hardkey and then the "Single" softkey.
7. Press the "Meas Data" hardkey. Press the "Time Channel 1 " softkey. The plot will display the displacement signals from the Electro-Mike position sensor.
8. Press the "Trace Coord" hardkey. Press the "More: NYQ REAL IMAG" softkey. Press the "REAL PART " softkey and ensure that the plot is "REAL" type. Press the "RETURN " softkey and ensure that the "X-axis LIN/LOG" softkey has "LIN" highlighted.
9. Press the "Scale" hardkey. Press the "Y per Div (Decades)" softkey and choose an appropriate Y-axis scale. Enter a numerical value on the keypad (Y per Div =3 V/div) and press the "Enter" softkey. Press the "Top Reference" softkey to set the top of the Y-axis scale (Top Ref = 15 V). Calibrate the Electro-Mike.
10. Place the position sensor near the 18th node of the truss. (Note the ruler measurements for calibration from 0 to 0.5 in at 0.05 in intervals.) Follow the "Simplified Operating Instructions" on the Electro-mike Circuit box using the DSA to examine the voltage levels.

#### HP DSA Set-up

11. Press the "Freq" hardkey. Press the "Record Length" softkey. Enter the desired record length with the numeric keypad or with the up and down arrows next to the keypad. (8 sec)
12. Press the "Fixed Sine" softkey and enter the desired frequency (1.485 Hz). Press the "Level" softkey and select the desired level (0.05 Vpk). Press the "Source ON/OFF" softkey and ensure that "ON" is highlighted. The DSA is now sending the fixed sine signal out of the source port into the truss.

#### RUN

13. Turn the truss control panel toggle switch to "Signal" to initiate the input signal to the truss. Allow the truss to stabilize at the desired vibrating frequency (wait 10-15 seconds) before going on to the next step.
14. Press the "START" hardkey to begin recording the position signals from the Electro-Mike. Allow the DSA to calibrate and allow the time response to be recorded for approximately 8 seconds.

15. Once the record length has expired, the plot will be displayed on the screen. Press the "PAUSE/CONT" hardkey to stop the measurements.
16. Press the "MARKER" hardkey. This will now allow you to use the marker softkeys and the marker position dial to determine peak values and other points of interest on the plots. (The marker is effective only for the active plot unless marker coupling is on.)

#### PLOT RESULTS

17. (This will screen dump the plots displayed on the screen to the laser printer.) Press the "PLOT/PRINT" hardkey. Press the "MORE SETUP" softkey. Press the "Device is Plot/Prnt" softkey and ensure that 'PRNT' is highlighted. Press the "Return" softkey.
18. Press the "Start Plot/Prnt" softkey to initiate the printing.

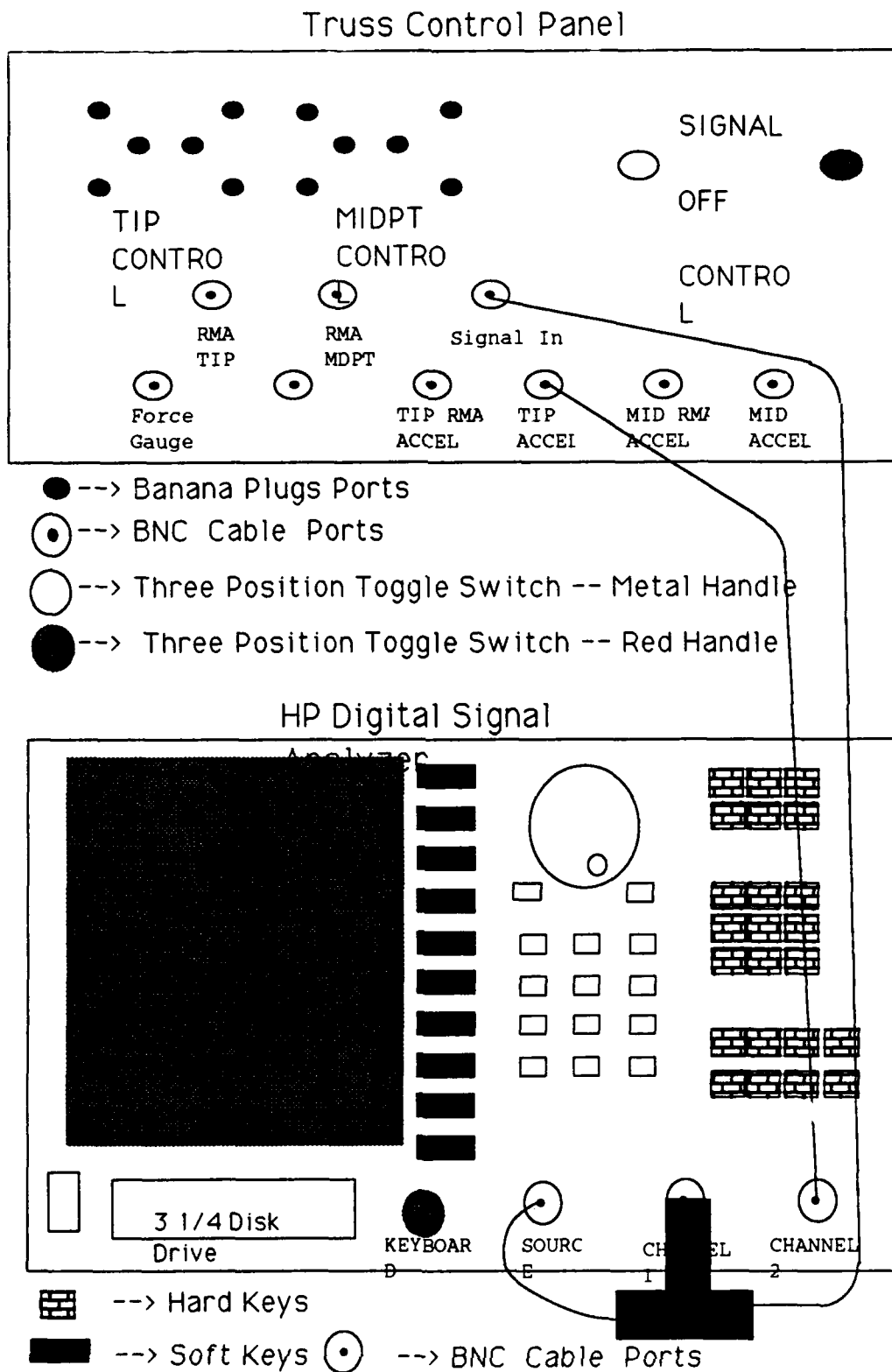


Figure D.1: Experiment 1 Configuration

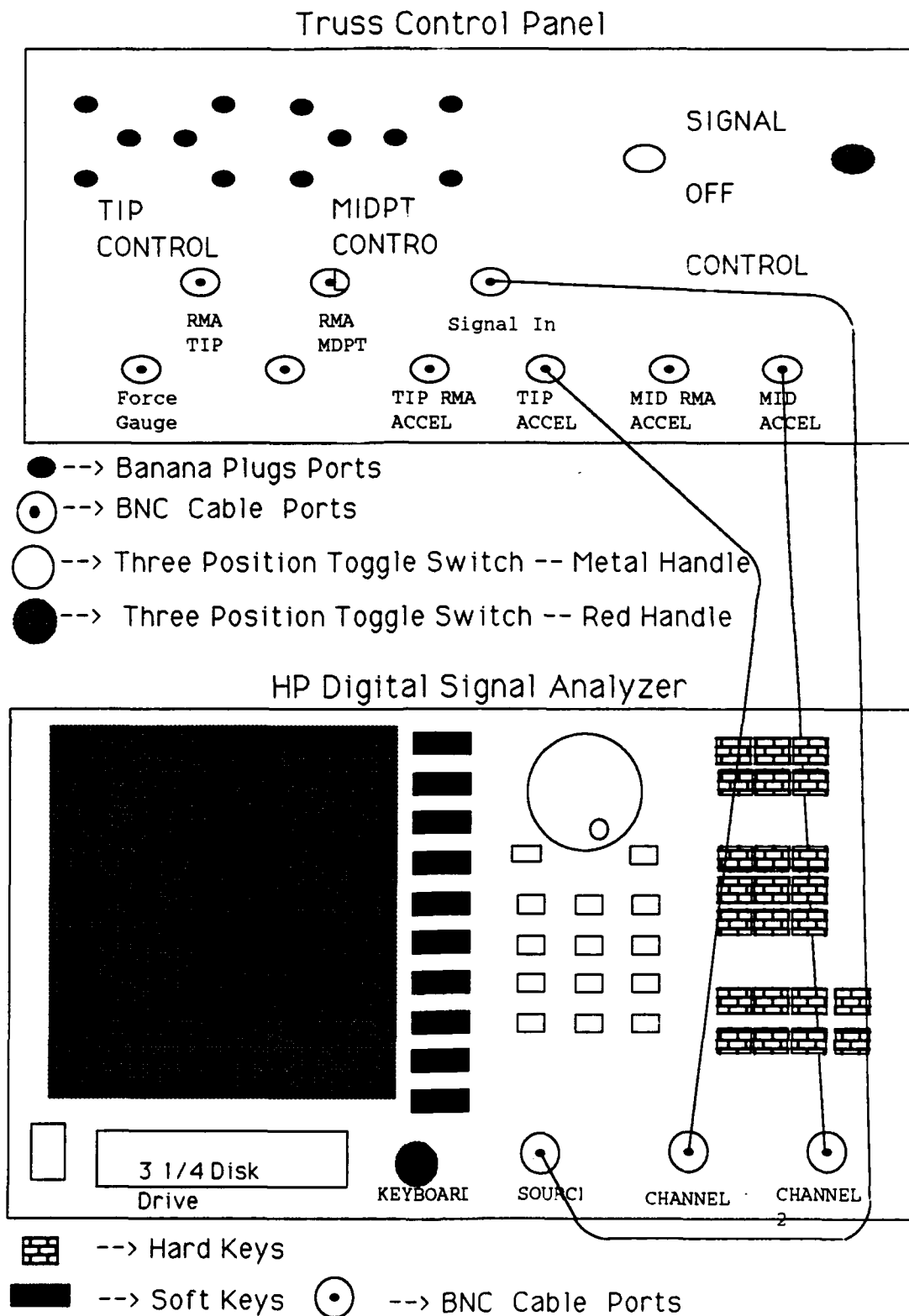
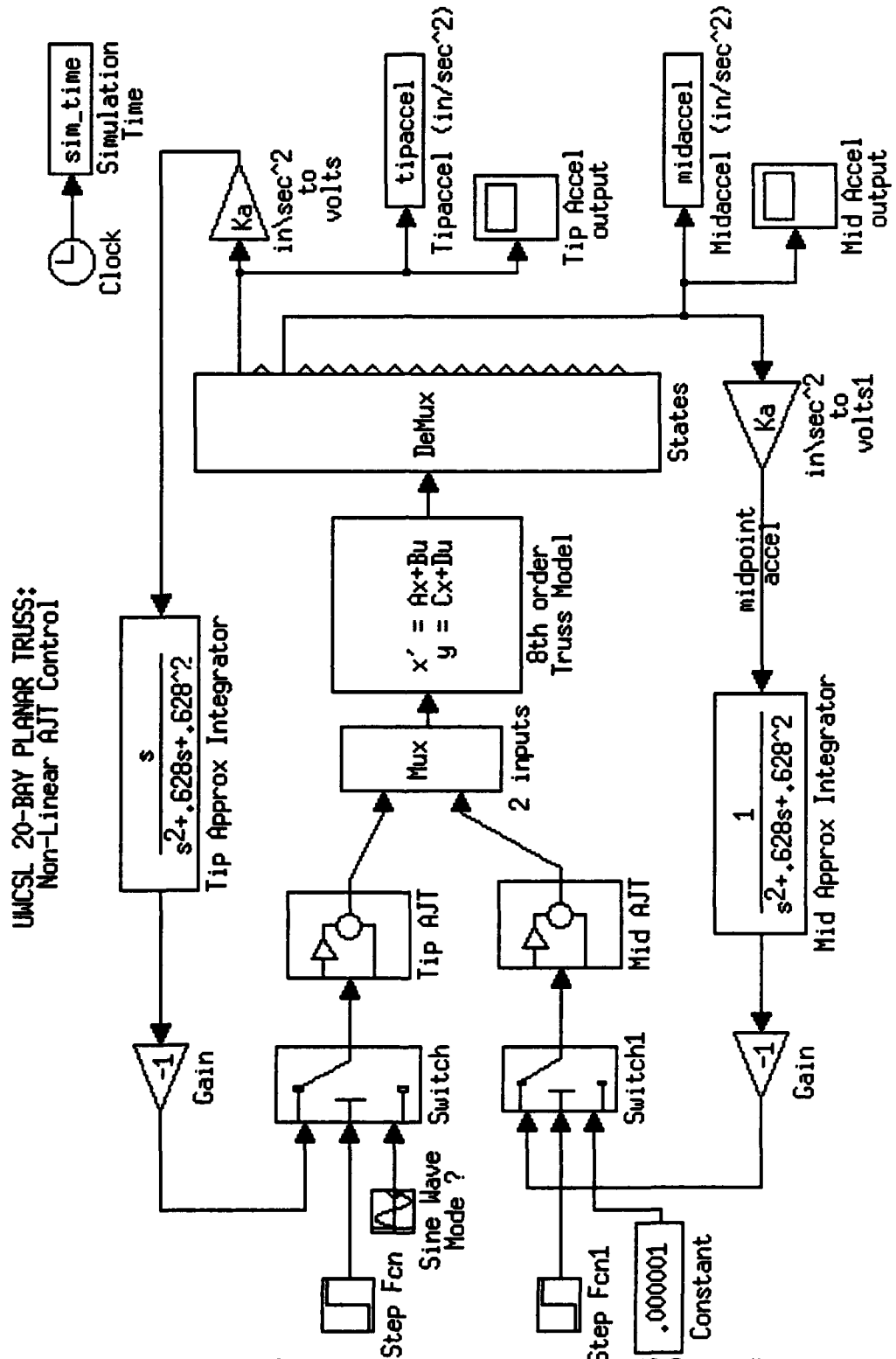


Figure D.2: Experiment 2 Configuration

## Appendix E

### **SIMULINK BLOCK DIAGRAMS FOR SIMULATION**

This appendix contains the SIMULINK block diagrams used for simulation of the truss models and the various controllers in this thesis. The block diagrams presented here are the basic models used to obtain the simulation results. Modifications were made to these models to obtain additional data or to simulate other controller configurations.



UMCSL 20-BAY PLANAR TRUSS:  
Classical Hybrid (AJT and RMA) Control

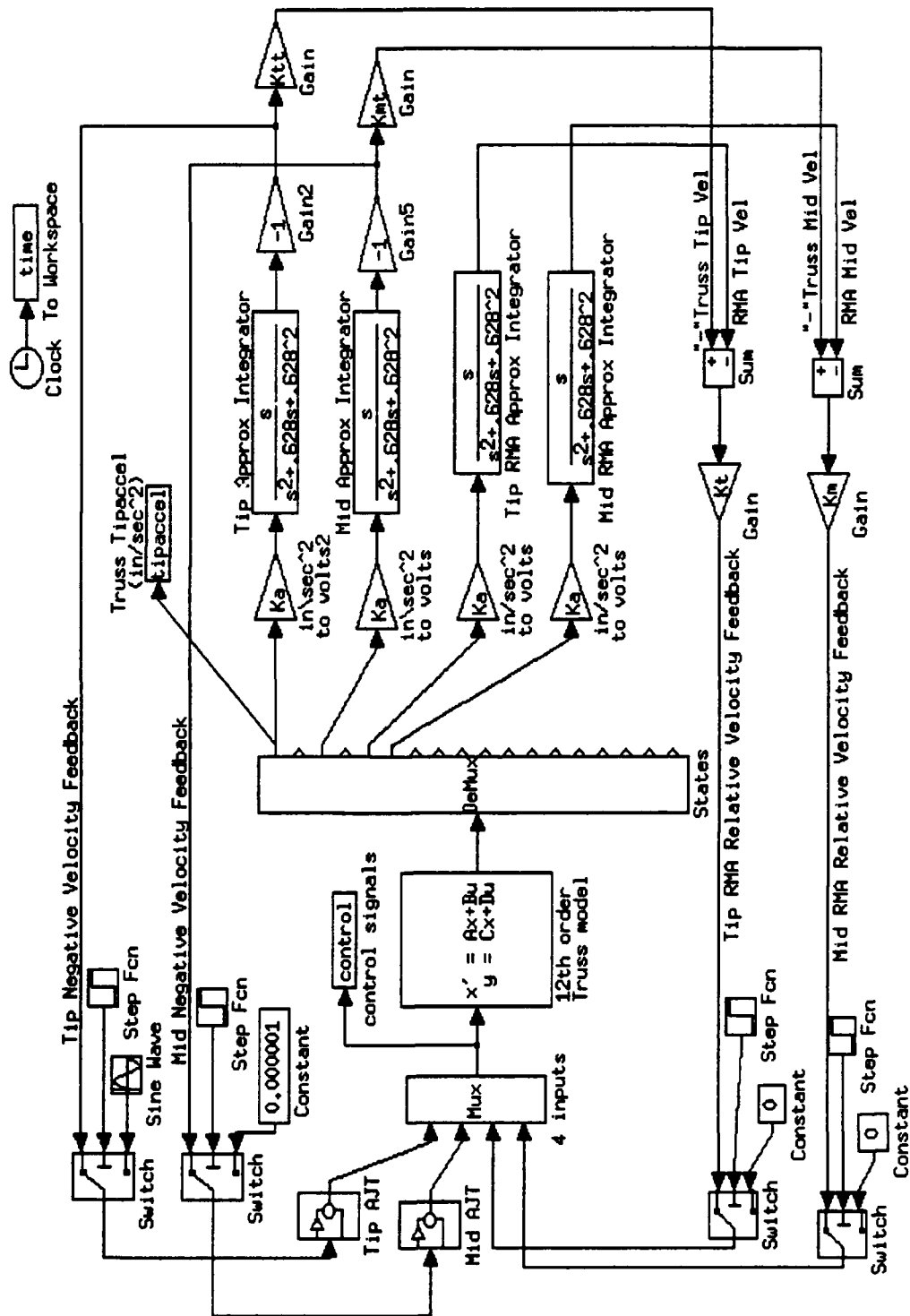


Figure E.2: SIMULINK Block Diagram: Hybrid AJT and RMA Controller

UMCSL 20-BAY PLANAR TRUSS:  
Classical Hybrid (AJT and RMA) Control

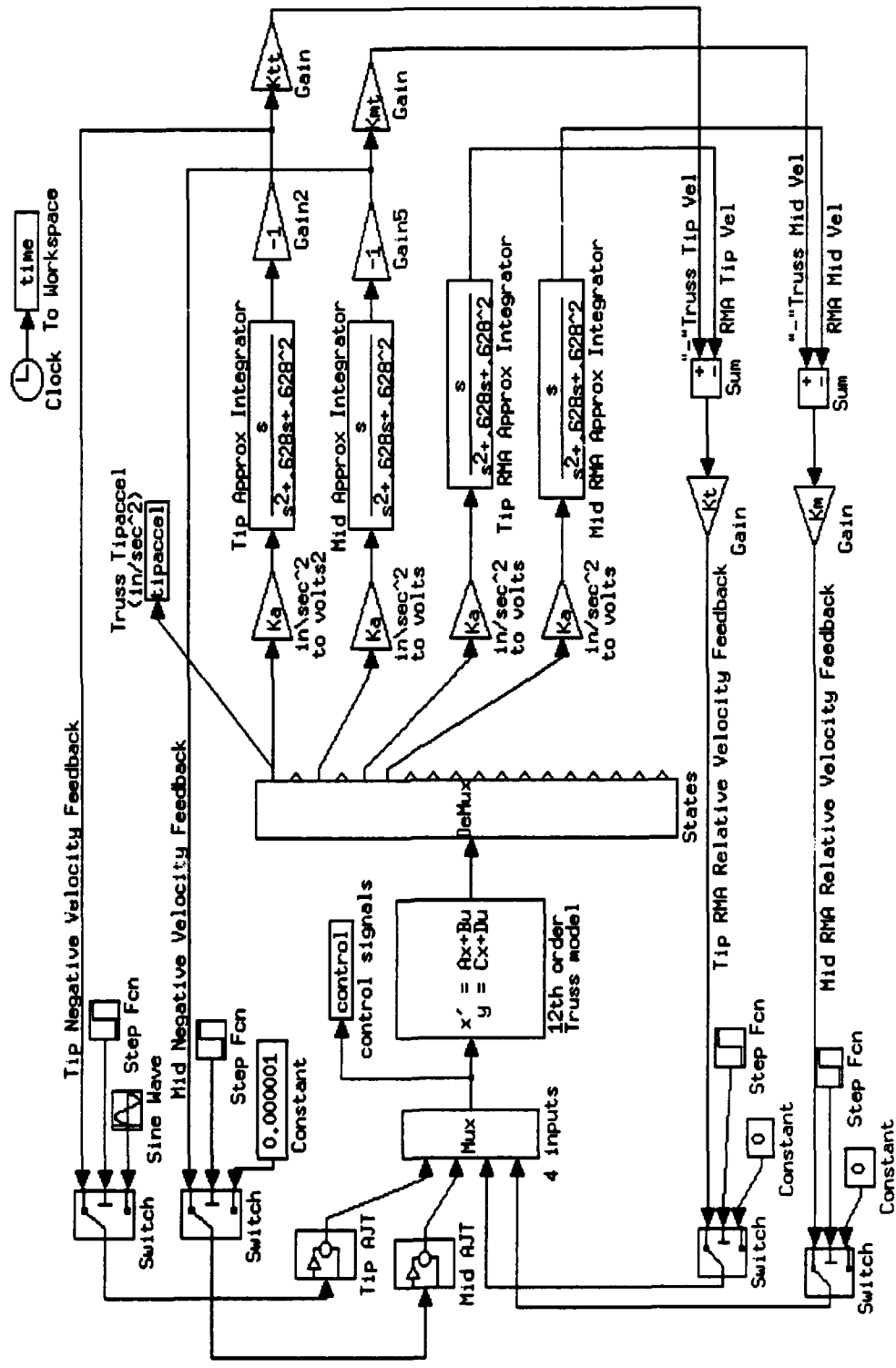


Figure E.3: SIMULINK Block Diagram: Digital AJT Controller

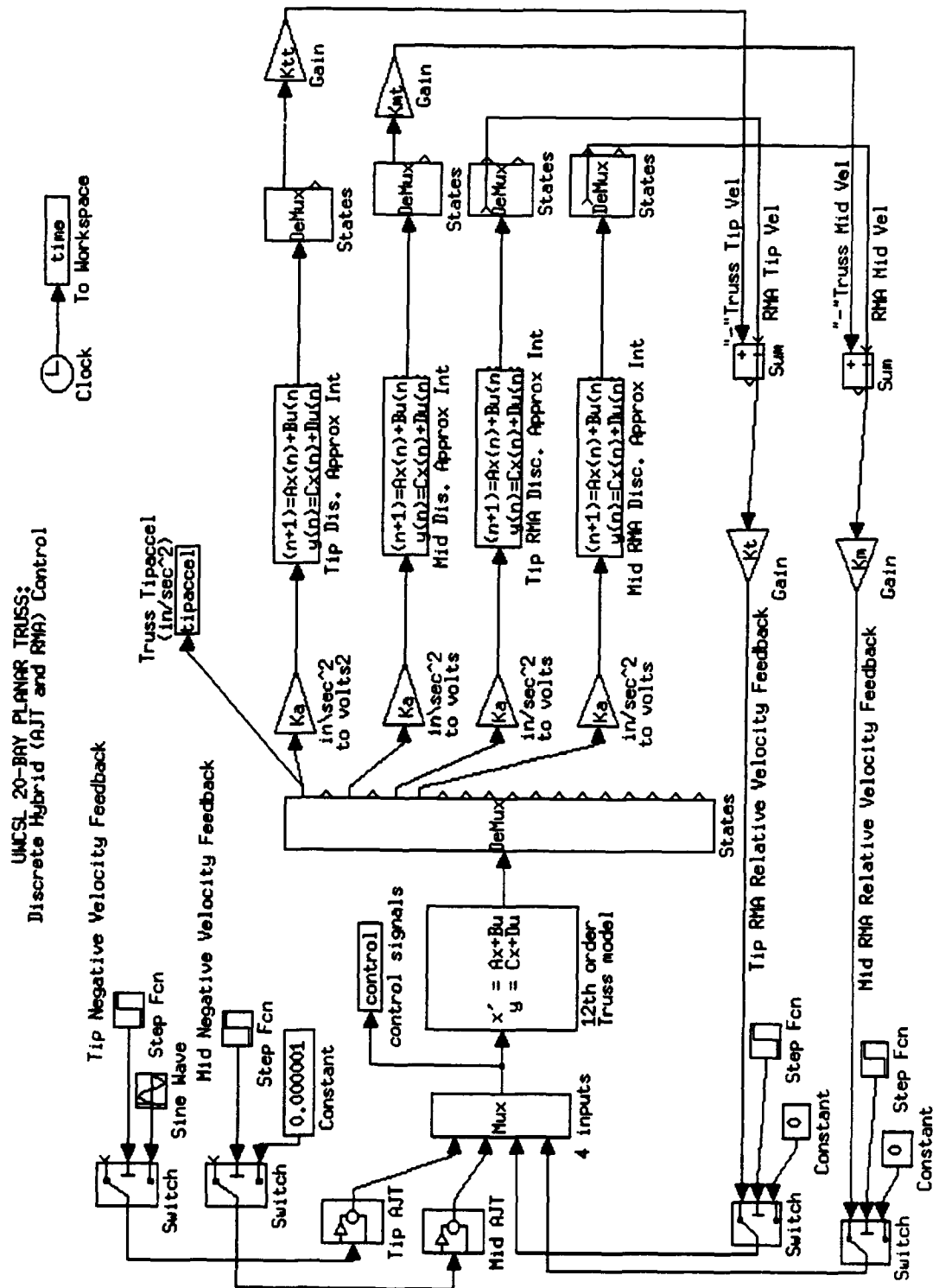


Figure E.4: SIMULINK Block Diagram: Digital Hybrid Controller



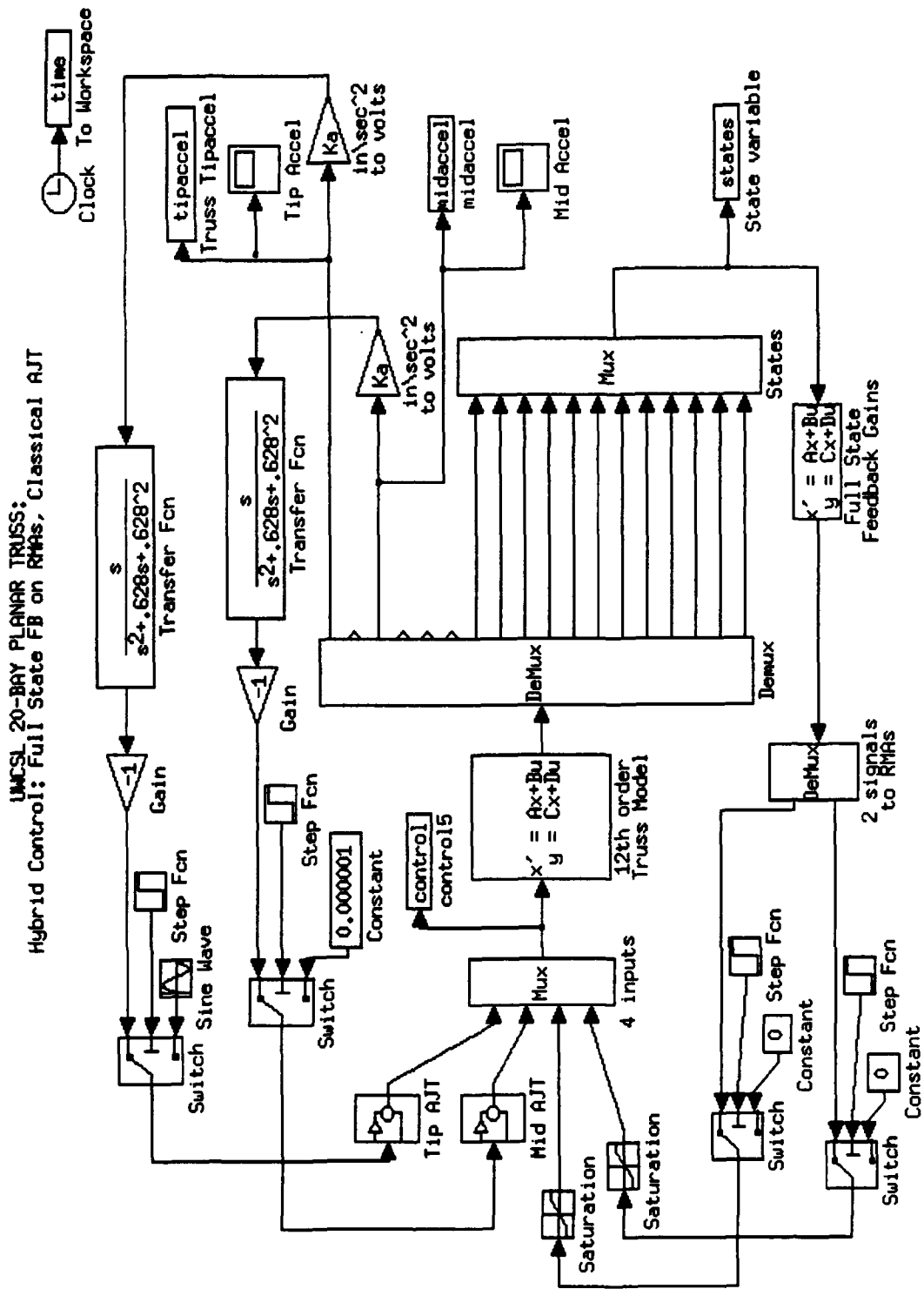


Figure E.6: SIMULINK Block Diagram: Hybrid (Full-State RMA, Classical AJT)

## Appendix F

### DIGITAL CONTROLLER STATE SPACE MATRICES AND LABVIEW DIAGRAMS

Emulation of the approximate integrator with a 5 millisecond sampling period (T) results in the following state space matrices which the discrete approximate integrator.

$A_d(5 \text{ msec}) =$

$$\begin{bmatrix} -0.9969 & 0.0031 \\ -0.0031 & 1.0000 \end{bmatrix}$$

$B_d(5 \text{ msec}) =$

$$\begin{bmatrix} 0.9984 \\ -0.0016 \end{bmatrix}$$

$C_d(5 \text{ msec}) =$

$$\begin{bmatrix} -0.0050 & 0.0000 \\ 0.0000 & -0.0050 \end{bmatrix}$$

$D_d(5 \text{ msec}) =$

$$\begin{bmatrix} -0.0025 \\ 0.0000 \end{bmatrix}$$

Emulation of the approximate integrator with a 10 millisecond sampling period (T) results in the following state space matrices which the discrete approximate integrator.

$A_d(10 \text{ msec}) =$

$$\begin{bmatrix} -0.9937 & 0.0063 \\ -0.0063 & 1.0000 \end{bmatrix}$$

$$B_d(10 \text{ msec}) =$$

$$\begin{bmatrix} 0.9969 \\ -0.0031 \end{bmatrix}$$

$$C_d(10 \text{ msec}) =$$

$$\begin{bmatrix} -0.0010 & 0.0000 \\ 0.0000 & -0.0010 \end{bmatrix}$$

$$D_d(10 \text{ msec}) =$$

$$\begin{bmatrix} -0.0050 \\ 0.0000 \end{bmatrix}$$

Emulation of the approximate integrator with a 20 millisecond sampling period (T) results in the following state space matrices which the discrete approximate integrator.

$$A_d(20 \text{ msec}) =$$

$$\begin{bmatrix} -0.9874 & 0.0125 \\ -0.0125 & 0.9999 \end{bmatrix}$$

$$B_d(20 \text{ msec}) =$$

$$\begin{bmatrix} 0.9937 \\ -0.0062 \end{bmatrix}$$

$$C_d(20 \text{ msec}) =$$

$$\begin{bmatrix} -0.0199 & -0.0001 \\ 0.0001 & -0.0200 \end{bmatrix}$$

$$D_d(20 \text{ msec}) =$$

$$\begin{bmatrix} -0.0099 \\ 0.0001 \end{bmatrix}$$

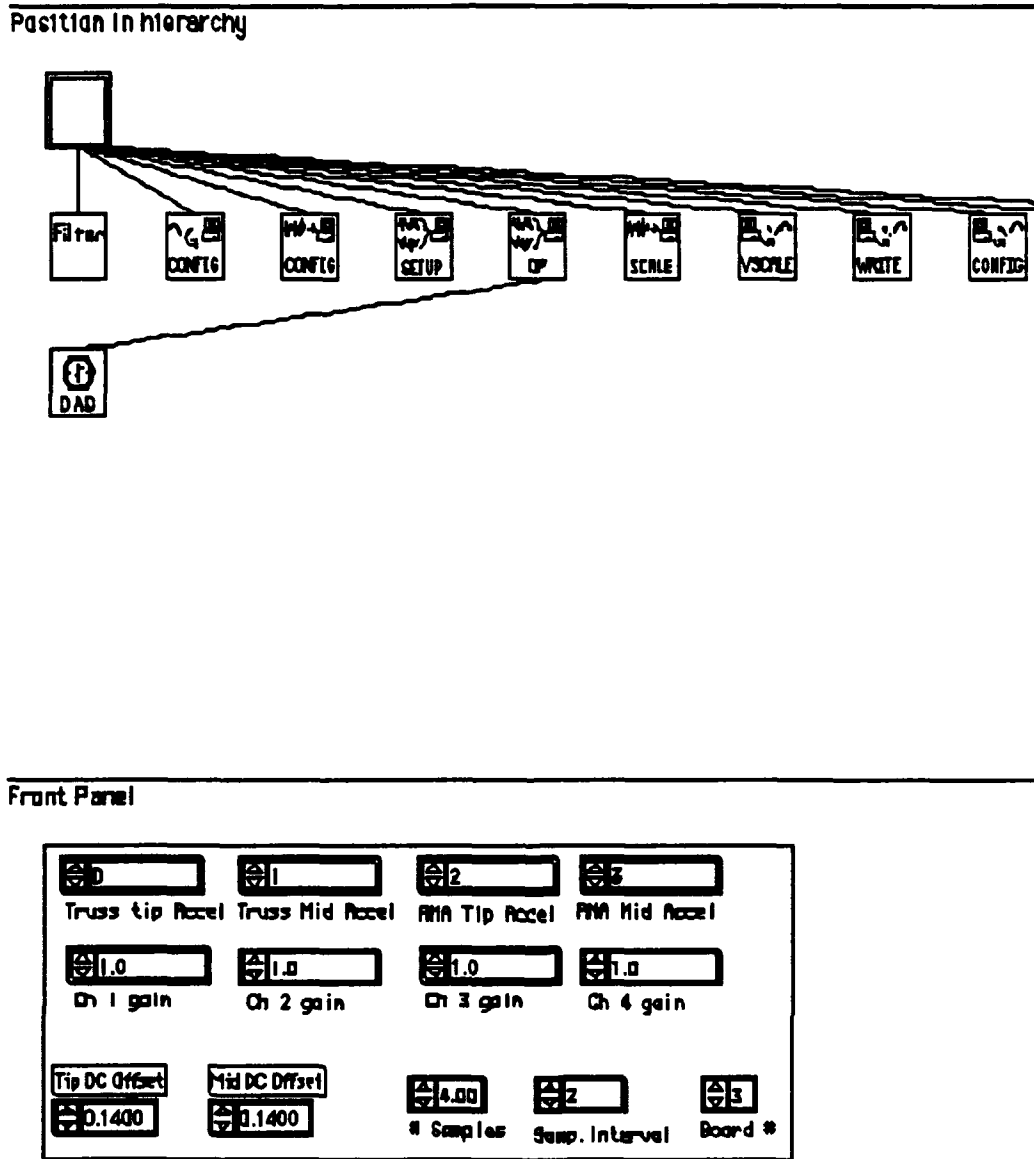


Figure F.1: LABVIEW: Block Diagram Hierarchy and Front Panel

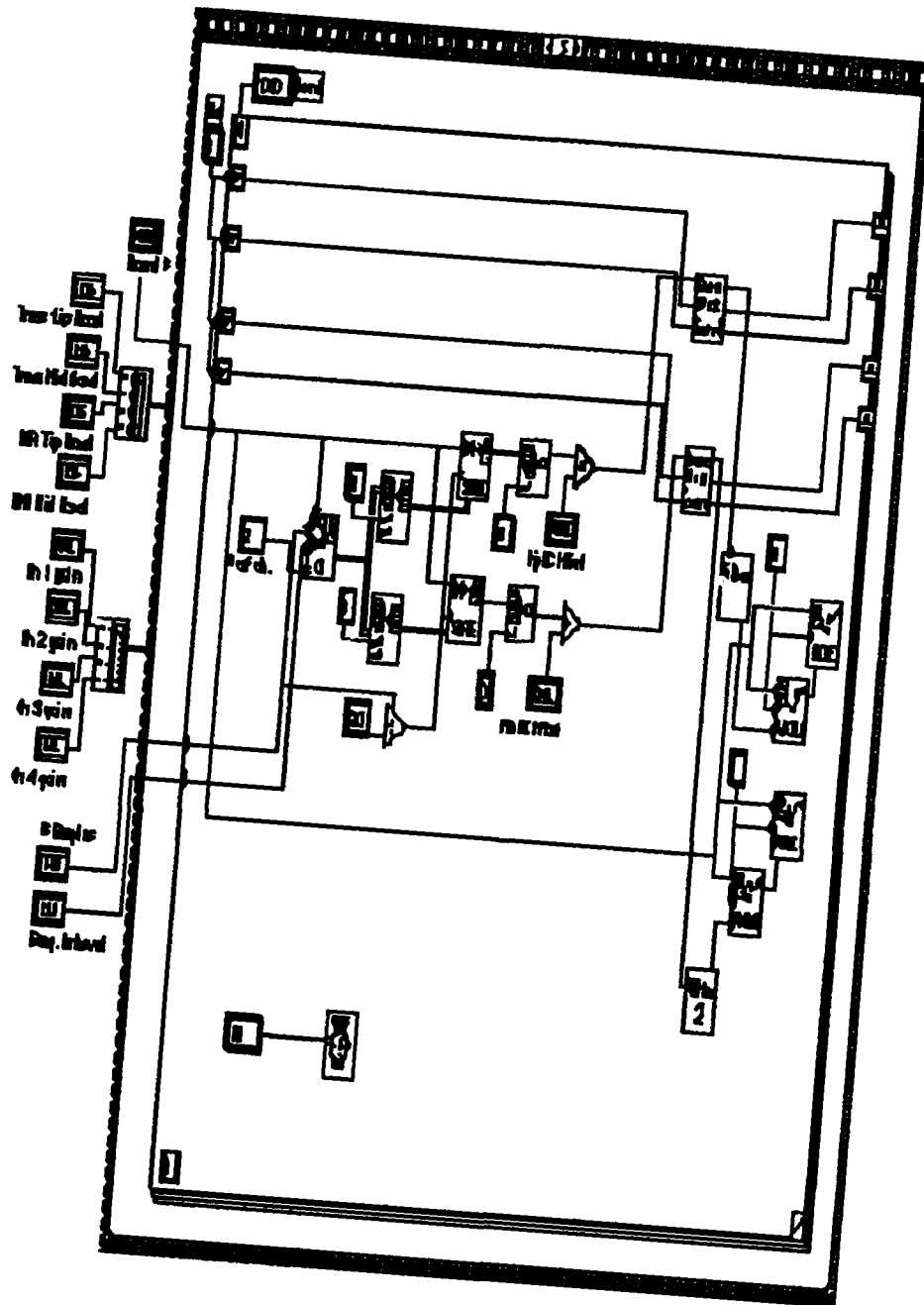


Figure F.2: LABVIEW: Digital AJT Controller Block Diagram

